ZERO SIDE FORCE VOLUTE DEVELOPMENT

Contract No. NAS8-39286
Final Report

Prepared for:

National Aeronautics & Space Administration
George C. Marshall Space Flight Center
Marshall Space Flight Center, AL 35812

P. G. Anderson, R. J. Franz, R. C. Farmer

Y. S. Chen
(Engineering Sciences, Inc.)

SECA, Inc.
3313 Bob Wallace Avenue
Suite 202
Huntsville, AL 35805

N96-16278

Unclas

G3/34   0086515

(NASA-CR-199198) ZERO SIDE FORCE
VOLUTE DEVELOPMENT Final Report
(SECA) 114 p

ACKNOWLEDGMENTS

SUMMARY

Collector scrolls on high performance centrifugal pumps are currently designed with methods which are based on very approximate flowfield models. Such design practices result in some volute configurations causing excessive side loads even at design flowrates. The purpose of this study was to develop and verify computational design tools which may be used to optimize volute configurations with respect to avoiding excessive loads on the bearings.

The new design methodology consisted of a volute grid generation module and a computational fluid dynamics (CFD) module to describe the volute geometry and predict the radial forces for a given flow condition, respectively. Initially, the CFD module was used to predict the impeller and the volute flowfields simultaneously; however, the required computation time was found to be excessive for parametric design studies. A second computational procedure was developed which utilized an analytical impeller flowfield model and an ordinary differential equation to describe the impeller/volute coupling obtained from the literature, Adkins & Brennen (1988). The second procedure resulted in 20 to 30 fold increase in computational speed for an analysis.

The volute design analysis was validated by postulating a volute geometry, constructing a volute to this configuration, and measuring the steady radial forces over a range of flow coefficients. Excellent agreement between model predictions and observed pump operation prove the computational impeller/volute pump model to be a valuable design tool. Further applications are recommended to fully establish the benefits of this new methodology.

TABLE OF CONTENTS

NOMENCLATURE

C_p static pressure coefficient

C_v function of the moments of the cross-sectional area

C_1, C_2, C_3 turbulence modeling constants

C_μ turbulence modeling constant

D_p pressure coefficient at volute inlet

d numerical dissipation terms of the discretized governing equations

F numerical fluxes in the ξ-direction of the discretized governing equations

$F\{t\}$ integration constant in Bernoulli's equation

F_{ox} steady fluid force acting on the impeller in the x-coordinate direction for a minimum force spiral volute

F_{oy} steady fluid force acting on the impeller in the y-coordinate direction for a minimum force spiral volute

F_x steady fluid force acting on the impeller in the x-coordinate direction

F_y steady fluid force acting on the impeller in the y-coordinate direction

G_{ij} diffusion metrics

h total head ($h^* = 2h/\rho\Omega^2 R_2^2$)

J Jacobian of coordinate transformation

k turbulence kinetic energy

P_i pressure in impeller

P_r turbulent kinetic energy production rate

p static pressure

q flow primitive variables

R impeller radius

r radial component of polar coordinate system

S_q source terms of the governing equations

ΔS cross-section area of a control volume perpendicular to the flux vector

s length in tangential direction

t time

U_i volume-weighted contravariant velocities

u_i flow velocity components in cartesian coordinate

V velocity in volute

v relative flow velocity in impeller

x cartesian coordinate in the direction from volute center to volute tongue

y cartesian coordinate in the direction normal to the x-coordinate

z cartesian coordinate

β relaxation parameter of the pressure correction equation
perturbation function for impeller flow (in Appendix A)

ϵ turbulent kinetic energy dissipation rate
distance between impeller and volute centers (in Appendix A)

ϵ^* ϵ/R_2 (in Appendix A)

$\epsilon_1, \epsilon_2, \epsilon_3$ coefficients of the numerical dissipation terms

ϕ flow coefficient

γ angle of flow path through impeller

μ effective viscosity

μ_l fluid viscosity
μ_t eddy viscosity
Ω radian frequency of the impeller (shaft) rotation
ω radian frequency of the circular whirl orbit
ψ total head rise coefficient
ρ fluid density
σ_q turbulence modeling constant
θ angular component of polar coordinate system
ξ, η, ς coordinates of computational domain

Subscripts
c   component of $\cos(\omega t)$
exp   experimental result
i   location of a grid point
o   centered impeller value (nondimensionalized)
s   component of $\sin(\omega t)$
x,y,z partial derivative components in the cartesian coordinate
1   impeller inlet
2   impeller discharge

Superscripts
n   variables at previous time step
n+1   variables at current time step
'   correction value
"   measurement made from frame fixed to rotating impeller
*   nondimensionalized quantity

1.0 INTRODUCTION

1.1 Overview

Collector scrolls on high performance centrifugal pumps are currently designed with methods which are based on very approximate flowfield models. Such design practices result in some volute configurations causing excessive side loads even at design flowrates. The purpose of this study was to develop and verify computational design tools which may be used to optimize volute configurations with respect to avoiding excessive loads on the bearings.

The Space Shuttle Main Engine's (SSME) High Pressure Fuel Turbopump (HPFTP) experiences such large side loads, that even after a short running time, the useful life of the rotor bearings is consumed and the bearings require replacement. While impeller/volute interactions produce side loads, current opinion is that the excessive side loads that require frequent bearing replacement is the result of other influences. The High Pressure Oxidizer Turbopump also experienced high side loads, which was a factor in the Alternate Turbopump Development (ATD). The ATD indeed produced very low side loads, but it was found that purposely increasingly these side loads improved the operation of the pump. Fluid film bearings are currently being strongly considered for turbopump application. The use of fluid bearings increases concern over rotordynamic effects. All of these concerns are benefited by an increased understanding of impeller/volute coupling effects caused by geometry and flowfield interactions. Thus, the ability to computationally simulate turbopumps more accurately would advance pump technology required for launch vehicle design.

The computational impeller/volute pump model was developed by creating three modules:

1. A grid generation code was written to expedite the accurate specification of the volute geometry with a small number of adjustable parameters.

2. A state-of-the-art computational fluid dynamics (CFD) code, FDNS, was used to simulate a fully coupled impeller/volute interaction and to determine side forces caused by the

pump operation.

3.   An existing analytical model developed by Adkins and Brennen (1988) was used to represent the impeller flow and the interaction between the impeller and the volute flowfields. This module was developed to affect an improvement in computational efficiency over the fully coupled impeller/volute CFD model.

These three modules constitute an accurate and practical code to design volute configurations. Existing test data and experimental tests conducted at Caltech as part of this study were used to provide verification for the computational impeller/volute pump model.

This report describes the development of these modules and their verification. The format of the presentation shall be: a brief summary of impeller/volute behavior, a description of volute grid generation, results of CFD simulations of impeller/volute flows, the design of a test volute, and the experimental verification of the performance of the test volute.

1.2 The Nature of the Problem

To eliminate the side forces on the pump bearings, the imbalance of radial forces created by the non-axisymmetric discharge conditions of the impeller flow into the volute must be eliminated. Currently, high performance centrifugal pump design is not performed by using CFD methodology. The analytical methodology which is utilized is typified by the analysis of Adkins and Brennen (1988), in which the interactions that occur between a centrifugal pump impeller and a volute are described with approximate analytical models. Treatments of the inability of blades to perfectly turn the flow through the impeller and of quasi-one dimensional flow through the volute are the major elements of this analysis. Since this study involves design concepts, the understanding of pump operation derived from previous experimental studies will be reviewed to establish the basis for future model development.

The design of the SSME turbopumps follows the trend toward higher speed and higher power density turbomachinery which creates a greater sensitivity to operational problems. This

2

study focused on the steady, radial forces acting on the impeller and its bearings due to the flow through the pump diffuser and volute. Even though the SSME HPFTP has three stages, attention was directed to a single stage pump so that a meaningful point of departure for CFD design tool development can be established. Using present design methods, radial side loads can be minimized for design flow rates for a single stage pump by properly matching an impeller and volute, as illustrated in Fig. 1 taken from Chamieh (1983). For the configuration shown, the design condition occurs when the flow coefficient has a value of 0.092. A recent account of fluid induced impeller forces is presented by Brennen (1994). However, such forces are not zero if design flowrates are not realized and if inlet flows are not ideal, as would be the case if the inlet flow were from a previous stage.

The steady impeller fluid force components, F_{ox} and F_{oy}, shown in Fig. 1 are defined in terms of a coordinate system in which x is the coordinate defined by the impeller centerline and the volute cutwater (tongue); y is normal to x in the direction of the impeller rotation. F_{ox} is nearly optimum since it is very small over a wide range of flowrates about the design point. The behavior of F_{oy} is much more difficult to optimize since it varies from large positive values to large negative values as the flow coefficient varies through the design flow condition. This point is emphasized by plotting the magnitude of the impeller force, F_o, as shown in Fig. 2, Chamieh (1983). F_o is not zero, but it is a minimum for the spiral volute (volute A) when F_{oy} passes through zero, i.e. the design point. To eliminate the side forces, F_{ox} and F_{oy} must simultaneously be zero. The best one could hope for is to design the volute/diffuser such that the "sweet-point" in the curve shown in Fig. 2 is close to zero for a wide range of flowrates about the design point. Hence, the design goal for selecting volute/diffuser configurations is to make the behavior of F_{oy} approach that of F_{ox} in a plot such as that shown in Fig. 1. The CFD model volute flow developed in this study was used to investigate conditions under which such desired behavior can be obtained.

The influence of volute shape is also shown in Fig. 2 by a comparison of a spiral volute to a circular volute (volute B), presented by Chamieh (1983). Volute B becomes the optimum shape as the flow coefficient approaches zero, as evidenced by this figure. This qualitative effect is typical of the predictive behavior which any CFD model must exhibit to be useful as
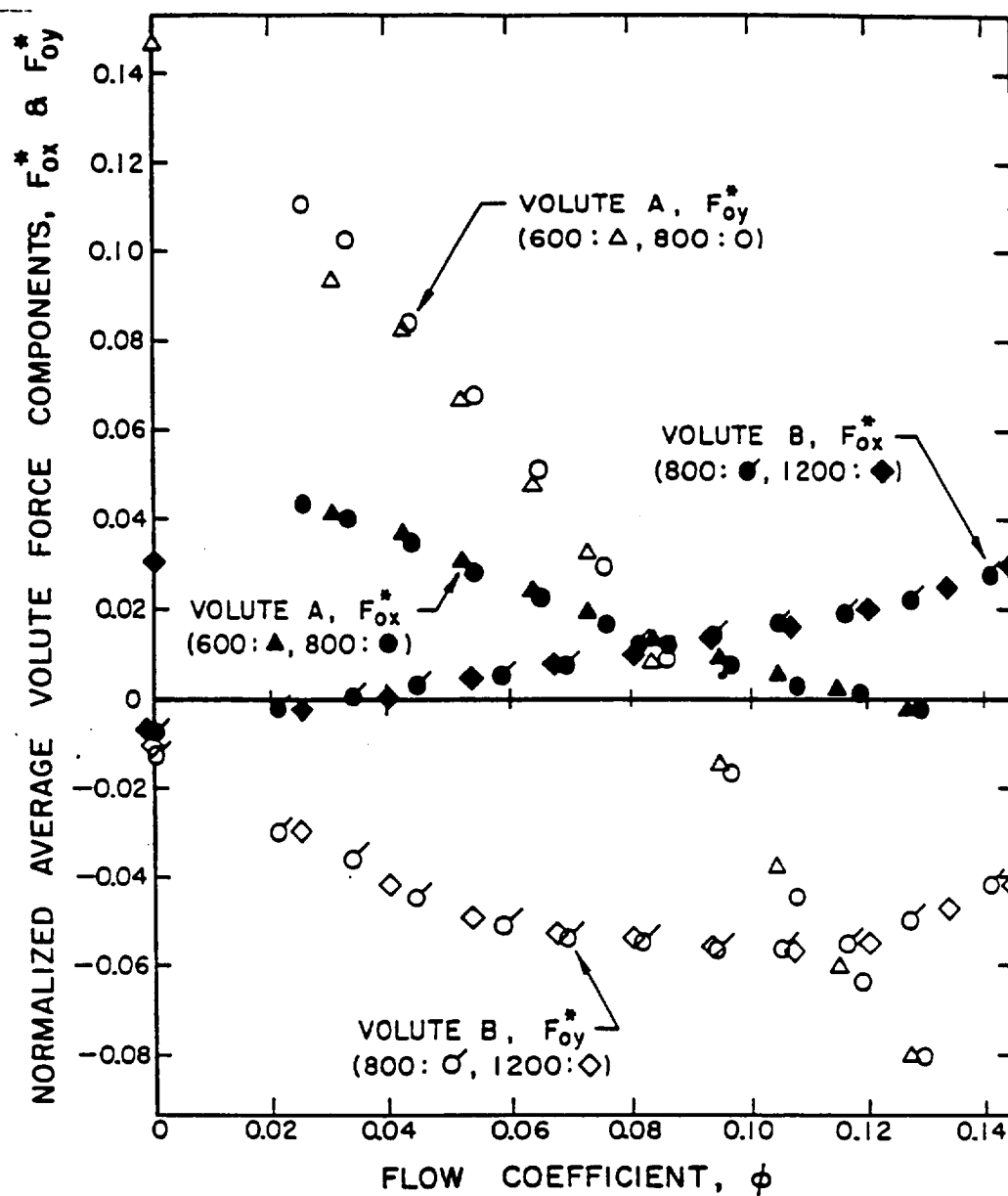
3

Fig. 1 Normalized average volute force components are shown for Impeller X, Volutes A and B and for face seal clearances of 0.79 mm. Rotor speeds in rpm and their corresponding symbols are shown in brackets, from Chamieh (1983)
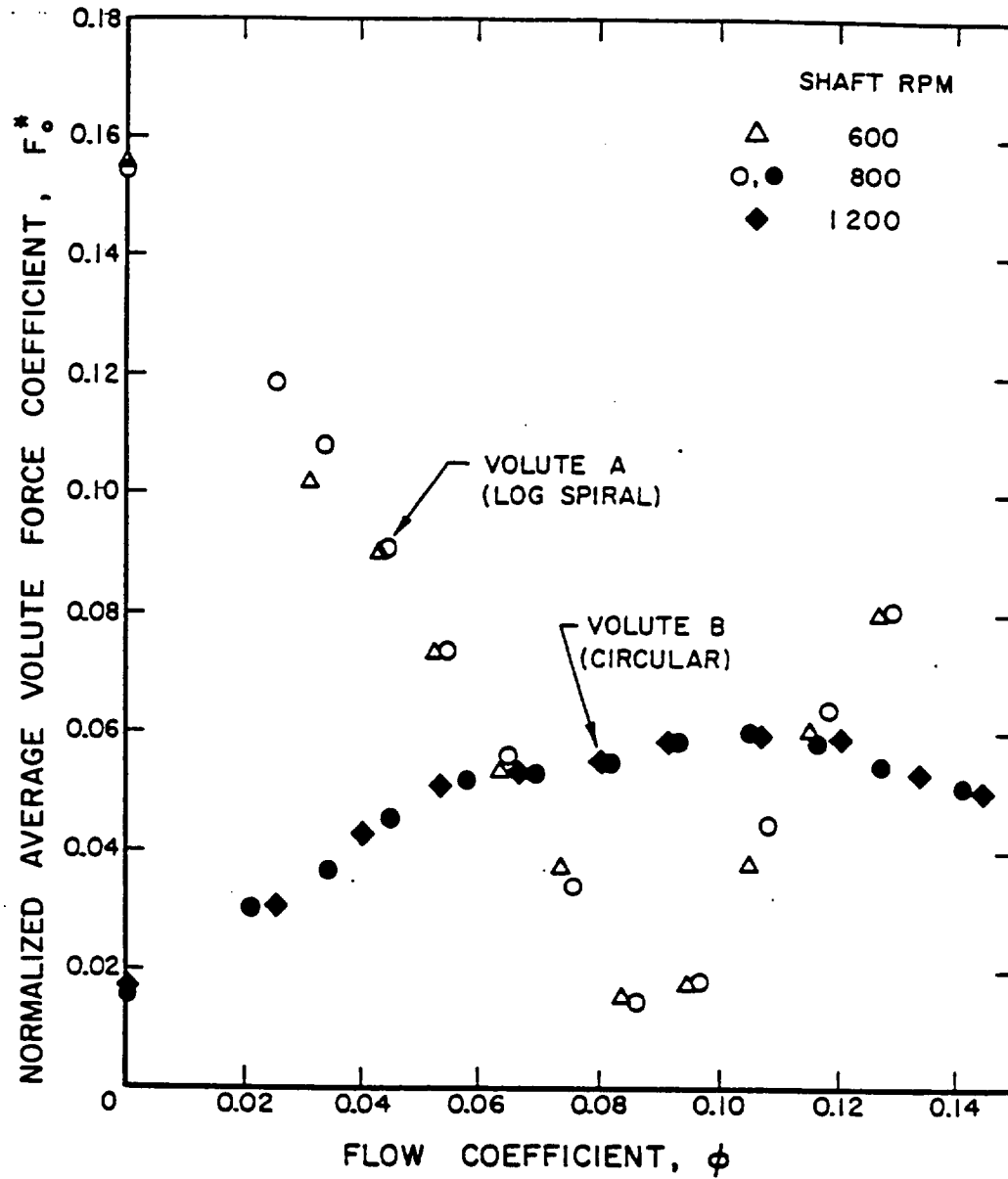
Fig. 2 Normalized average volute force for Impeller X and face seal clearances of 0.79 mm. Open and closed symbols represent data for Volutes A and B respectively, from Chamieh (1983).

a design tool for centrifugal pumps.

Experimental studies have also been conducted to optimize volute configurations. Figure 3 from Agostinelli, et al (1960) shows the effect on the radial forces of using a volute which is initially circular and then becomes spiral, as the flow progresses from the cutwater to the discharge. This figure also shows the effect of using a double volute, which is nearly ideal for reducing radial forces at all flow rates. However, other design penalties, such as additional weight and structural complexity in geometrically small pumps, preclude the usefulness of this configuration. A vaned diffuser between the impeller and the volute may also be used to reduce radial forces, but, again, at the expense of introducing other complications. This study addressed only the improvement of volute shape for controlling side loads.

Several other very important factors also contribute to radial forces: (1) those due to whirl caused by the impeller being displaced from the "design" center of the volute (because of shaft wear, bearing wear, tolerances, etc.), (2) those due to cavitation which are strongly dependent on the thermodynamic properties of the pumped fluid and pump design, and (3) those due to leakage through the impeller seals. These factors have been critically important in establishing the current design of the HPFTP and the HPOTP for the SSME, although they are not considered in this investigation.

However, studies of such effects have resulted in the establishment of an extremely fine laboratory, the Rotor Force Test Facility (RFTF), for studying centrifugal pump operations at Caltech under NASA/MSFC sponsorship. The outstanding feature of the RFTF is the unique system which has been developed to measure forces on impeller shafts. This facility was used to conduct verification tests to support the development of the CFD impeller/volute model developed in this study.
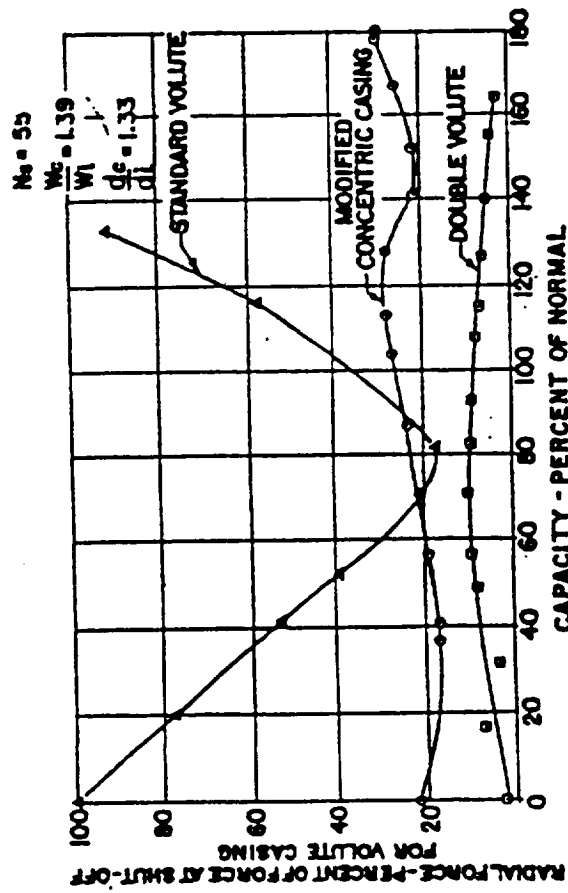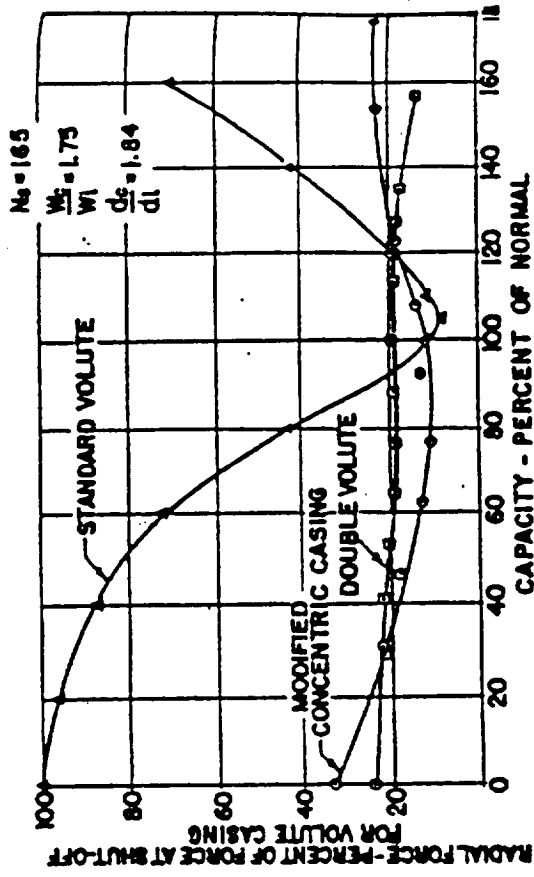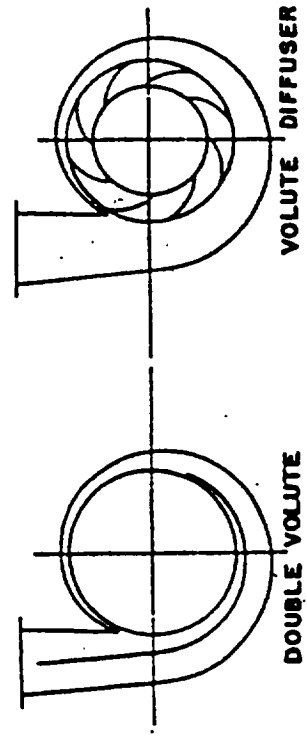
Fig. 3 Volute Designs for Minimizing Radially Unballanced Forces

2.0 VOLUTE GRID GENERATION

To expedite the optimization of volute geometry, an algebraic grid generator code was written which contains a small number of adjustable parameters, but which creates a wide spectrum of volute shapes. As a point of departure and to illustrate the general features of impellers and volutes, Volute A and Impeller X, which were experimentally tested by Adkins and Brennen (1988), were chosen for further study. Volute A and Impeller X are shown in Figs. 4 and 5, respectively.

Two mappings are employed to create the volute grid. The first describes the volute surface and the second generates the grid. In order to describe the surface of the volute using a natural physical-to-surface coordinate mapping, the volute is divided into three regions. The regions are the spiral, discharge and tongue regions. A fourth region, designated the blank region, adjacent to the tongue and discharge regions can be created in case the second mapping puts grid lines through the tongue into the wall. These four regions constitute the first volute mapping. The grid used in flow computation is obtained using a second mapping between the surface-to-computational coordinates. The user can create an alternate grid topology by creating a different second mapping. The Grid Code is described in Appendix C.

The volute surface is developed from cross-sections and from contour edges between them. In the cross-section planes all the regions have H-grids. In the midplane of the contours the regions are also H, except for the tongue region which is C.

The spiral region can be created using two different methods. The first interpolates between cross-sections defined at angles along the spiral contour using cubic splines with knots at the endpoints of the curve segments that make up the cross-section. The first and last angles encompass 360°. The second method describes the cross-sections in terms of the variables shown in Fig. 6. These variables are specified by functions of θ such as: Archimedian spirals ($r = a\theta$), log spirals ($\ln r = a\theta$), circular arcs, cubic splines, line segments, and special functions for $r_F\{\theta\}$.
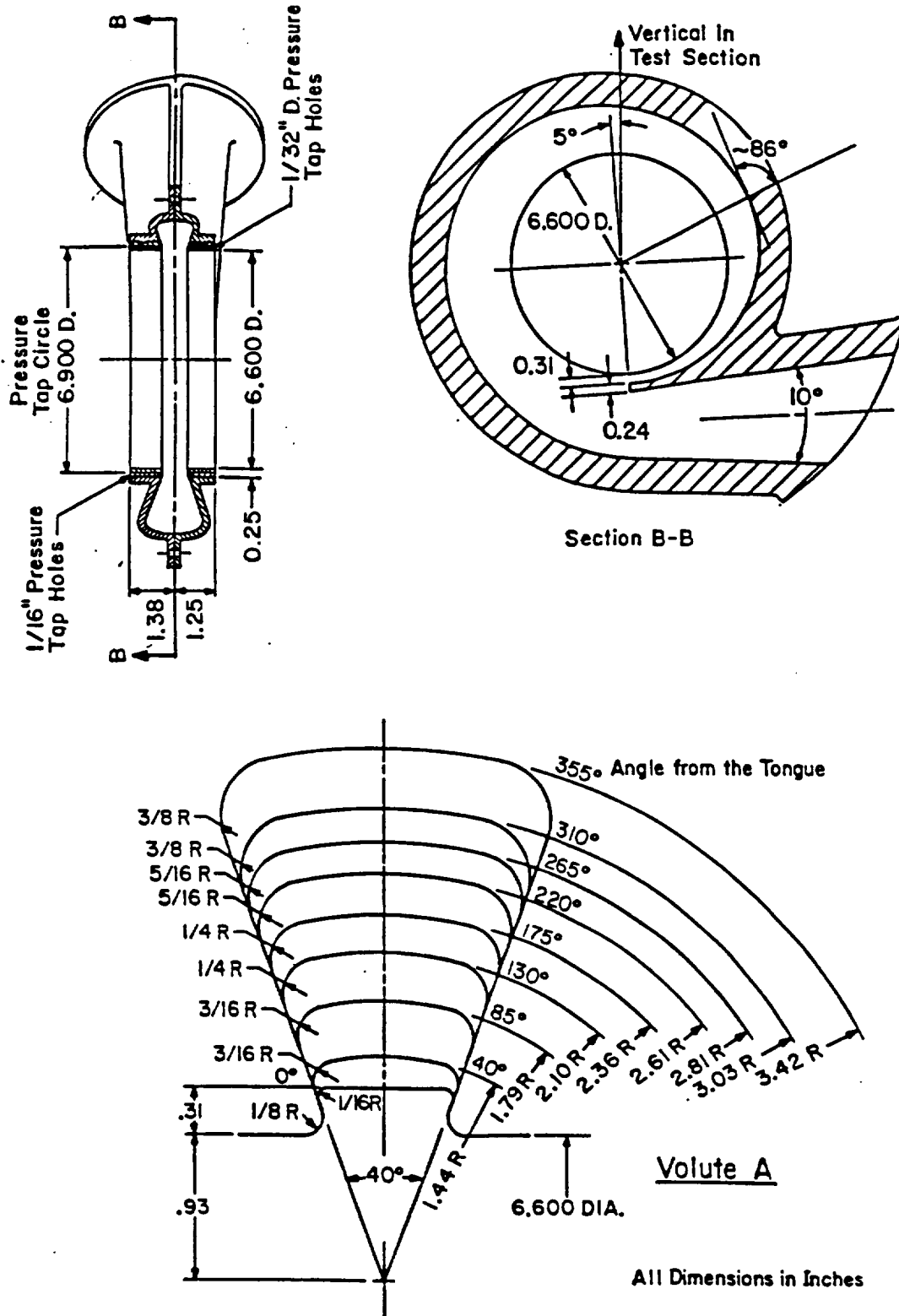
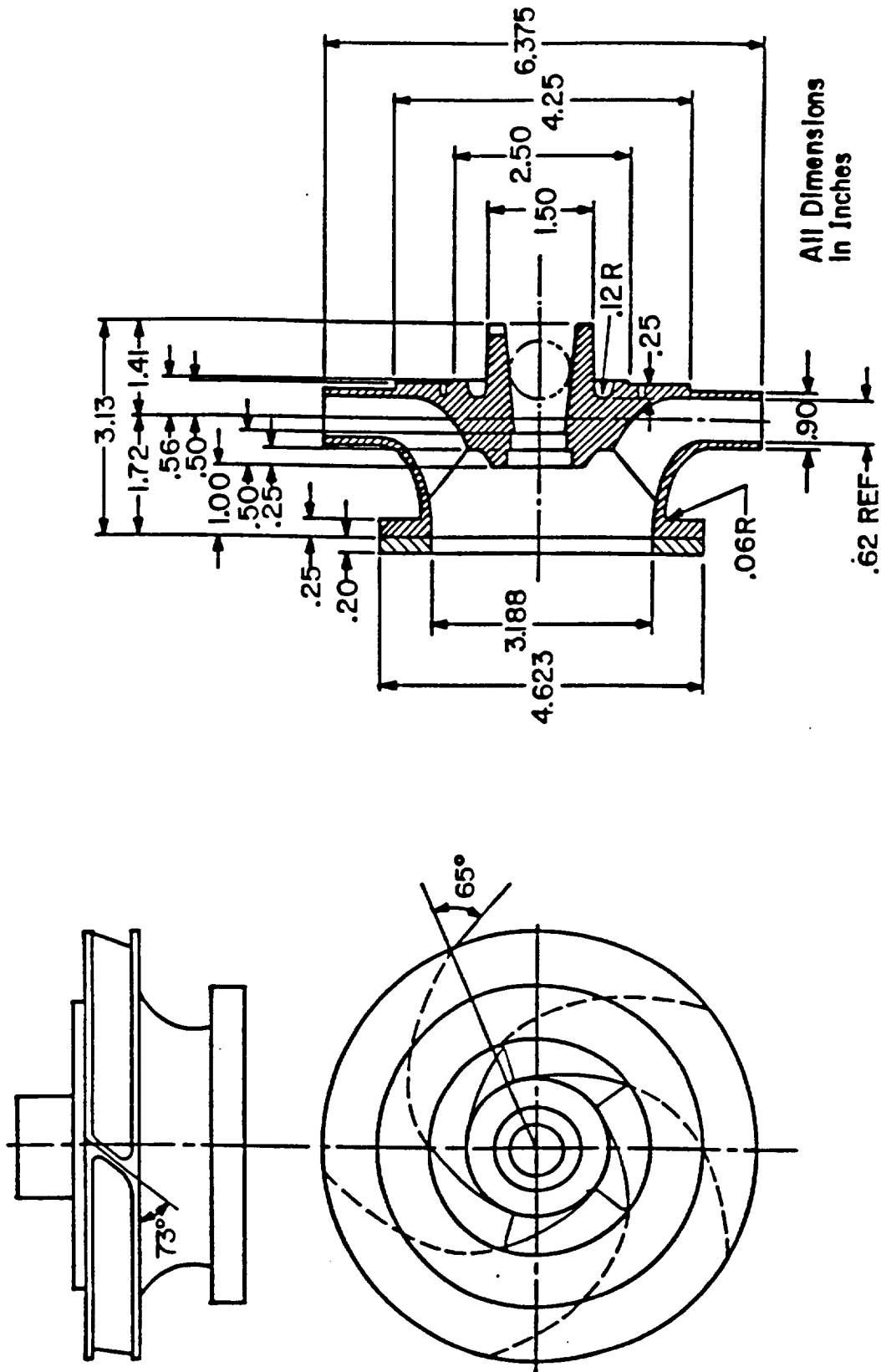Fig. 4 Drawing of Volute A from Adkins (1986)

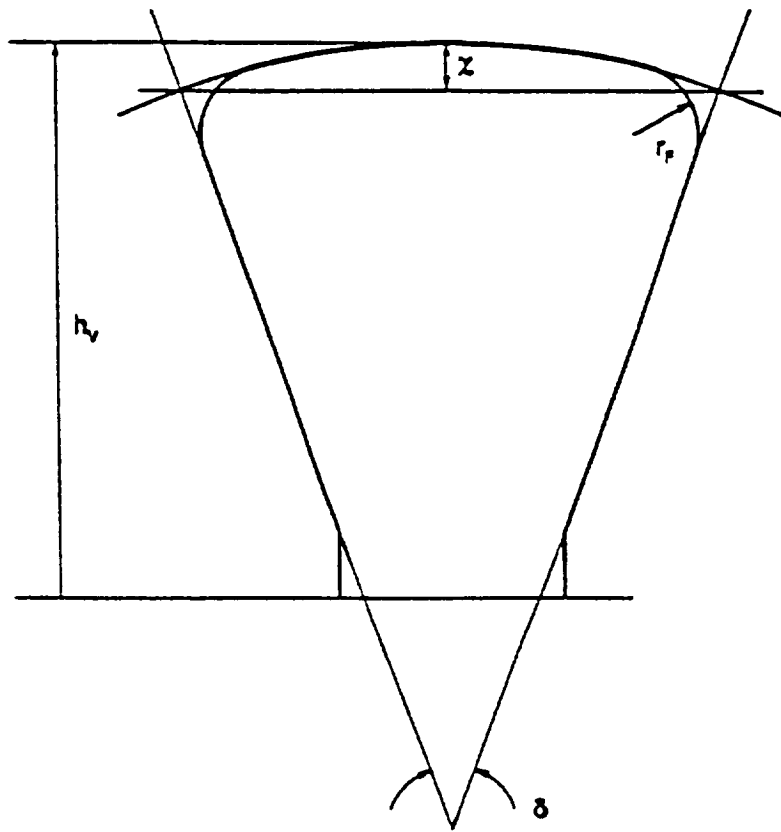Fig. 5 Drawing of Impeller X from Adkins (1986).

All Dimensions
In Inches

10

Fig. 6 Definition of Variables for F(Θ) Cross-Section

The discharge region is defined from a series of cross-sections starting at the last spiral cross-section and extending through a sequence of one or more circular cross-sections. Two sets of contour edges, one starting from the last spiral contour and the other from the tongue control the interpolation of the surface grid. For the initial section, the last spiral cross-section is cut by the tongue region contour and the corners rounded. A circular cross-section is defined at the end of the discharge contours.

The tongue region is contained within the spiral region, bounded by the last two defined spiral cross-sections. Beginning from the top of the first spiral cross-section, the tongue contour arcs around to meet the discharge contour. Options are provided to calculate the actual tongue/discharge contour intersection point. The contour edges are projected in the ±axial direction onto the exterior surface of the spiral region to create edges that "square off" the tongue region. The corners are rounded between the top of the first spiral cross-section and the bottom of the initial discharge cross-section using a rolling ball algorithm.

Figures 7-10 show details of the volute geometry generated with the first mapping of the grid code. Figure 7 shows the spiral and discharge regions with the tongue left out. Figure 8 shows the tongue section. Figures 9-10 show the grid with the tongue region included. Figure 10 shows details of the blending of the tongue with the other part of the grid. Figures 11-14 show various surface to computational coordinate mappings for creating interior grid points. Figure 15 shows a mapping of the geometric grid into the computational domain.

Volute A was chosen as a baseline test case for performing a 3-D CFD simulation. It was expected that the volute geometry would have a large effect on the computed flowfield. If such is indeed the case, special consideration should be given to volute A since it has already been constructed. The data available from the volute drawings needed to generate a grid are: the dimensions of the volute cross-sections at various angles, typically every 45°. A partial description of the fabrication process follows. A sheet of aluminum was cut into the nine specified cross-section shapes. The nine aluminum sections were positioned at the appropriate locations on a flat board. Wood forms were cut and glued between the aluminum sections. The craftsman sanded the wood forms to provide a smooth transition between the specified cross-
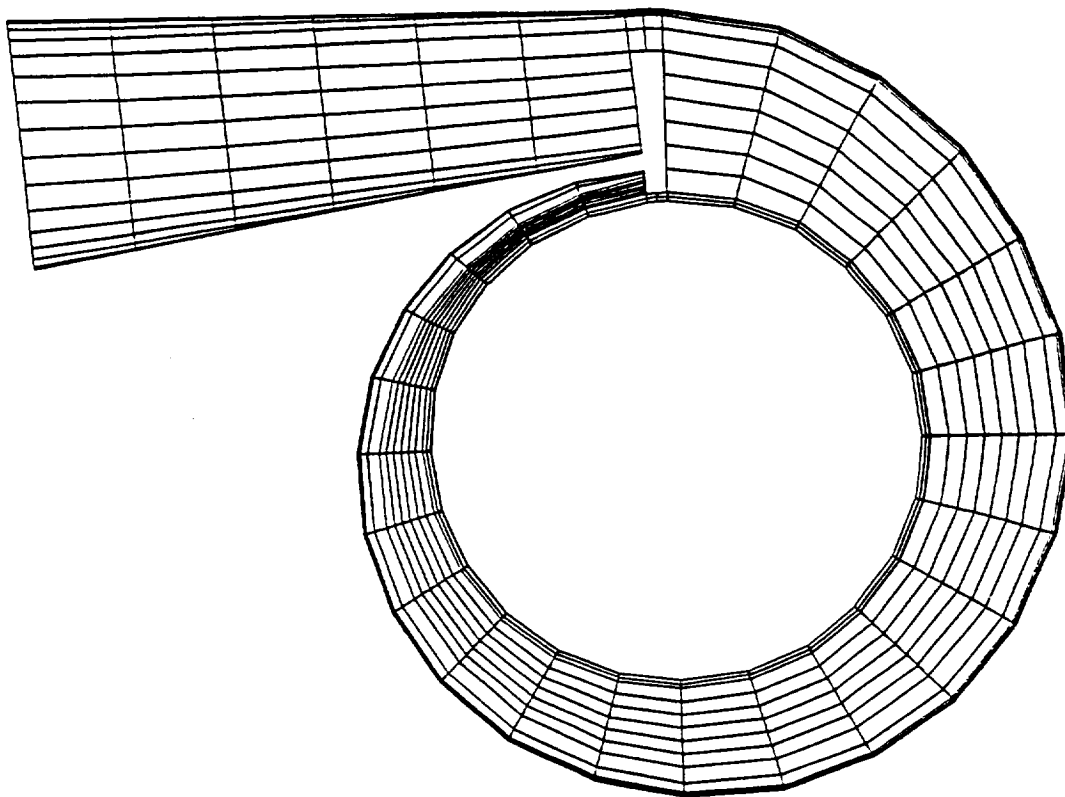
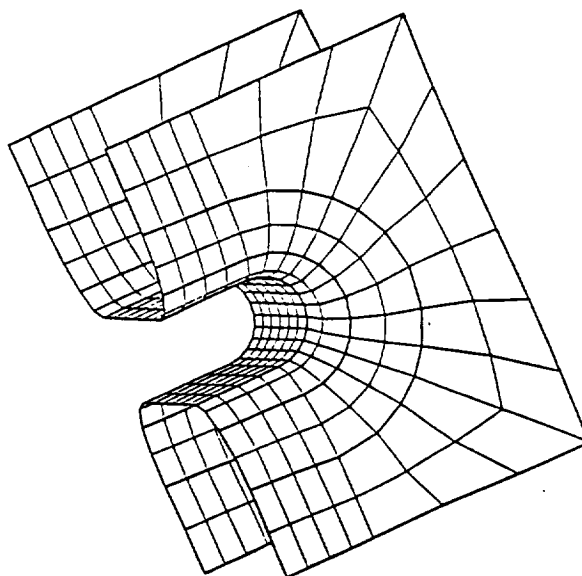Fig. 7 Volute Surface, Excluding the Tongue Region

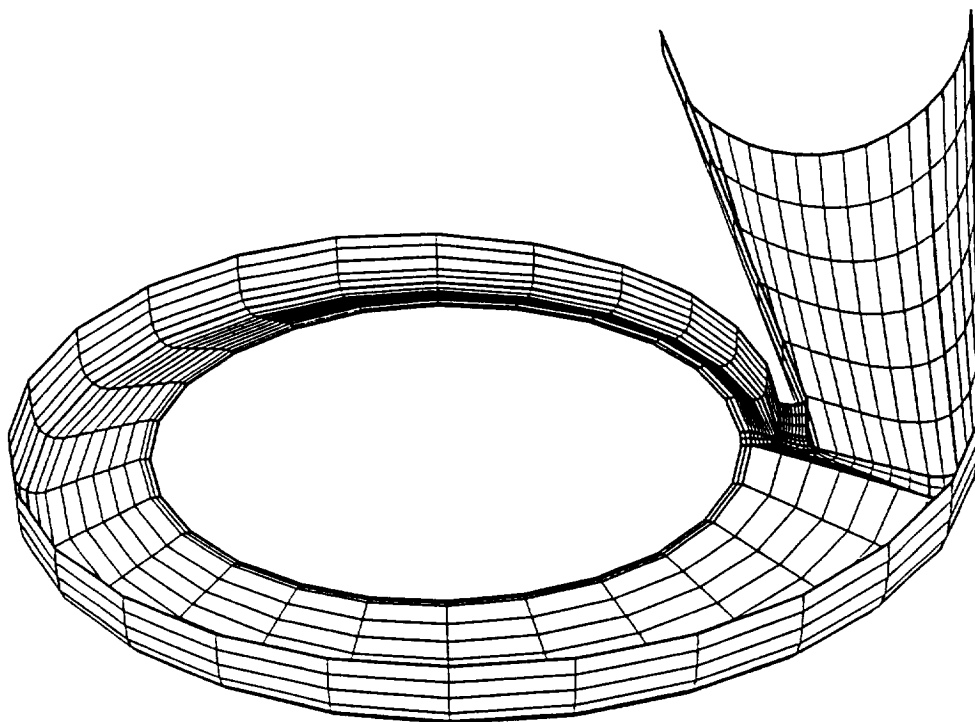Fig. 8 An Illustration of Generating the Tongue Surface

13

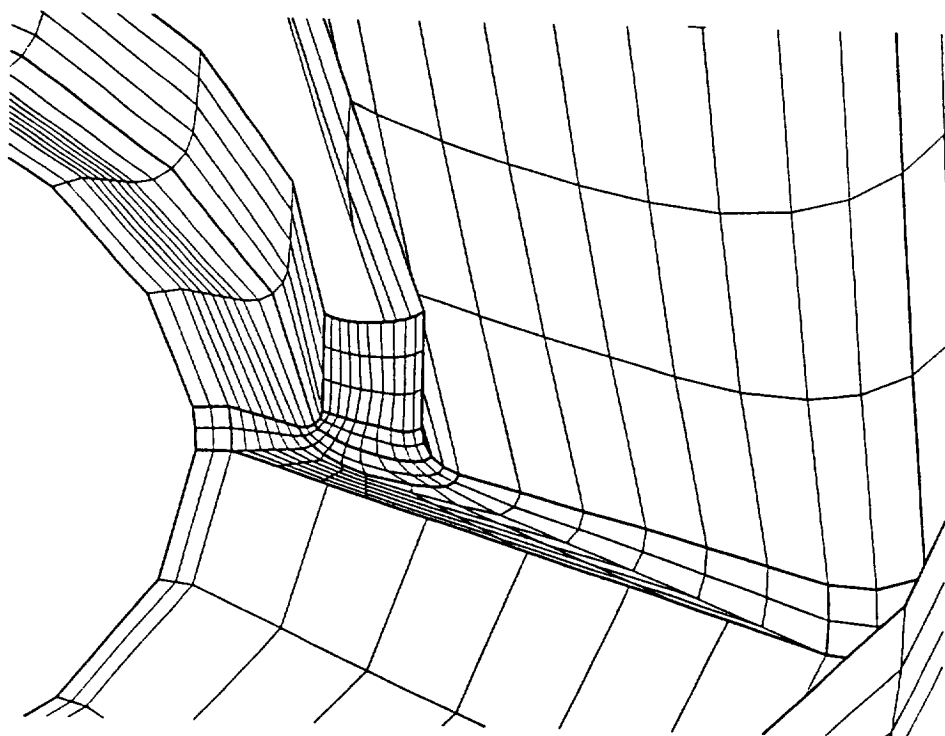Fig. 9 Volute Surface on One Side of the Midplane

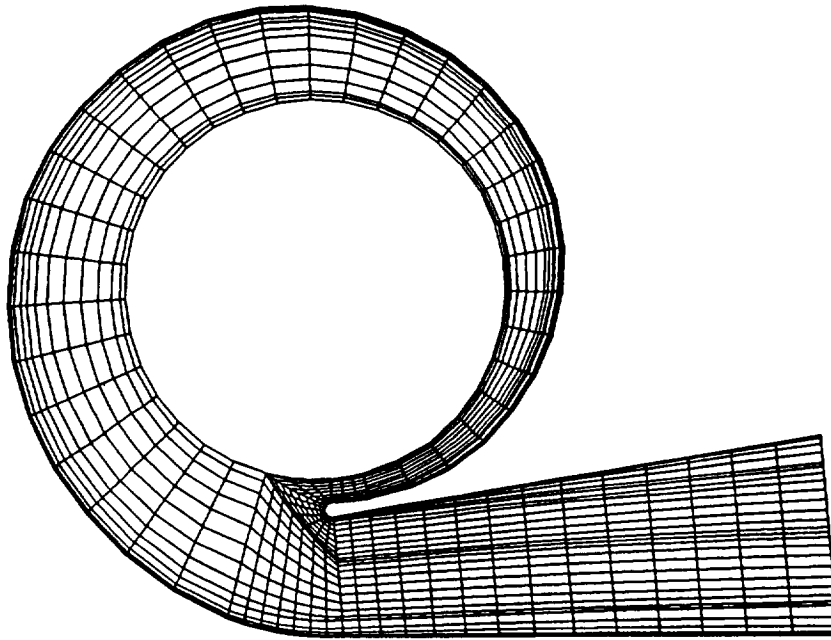Fig. 10 Volute Surface, Focusing on the Tongue

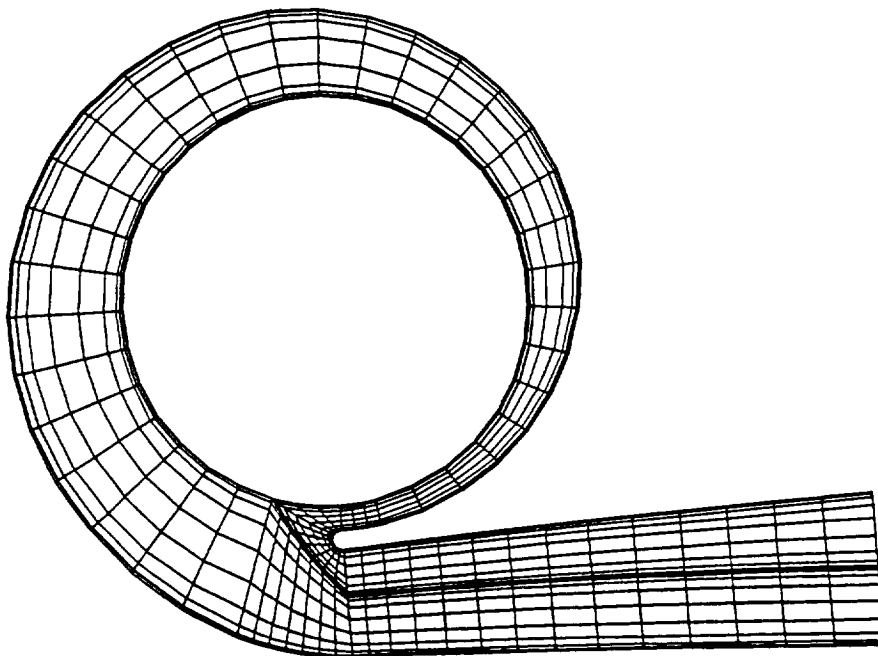Fig. 11 Exterior Surface of 3-D Grid, used in Impeller/Volute Coupled CFD Solution

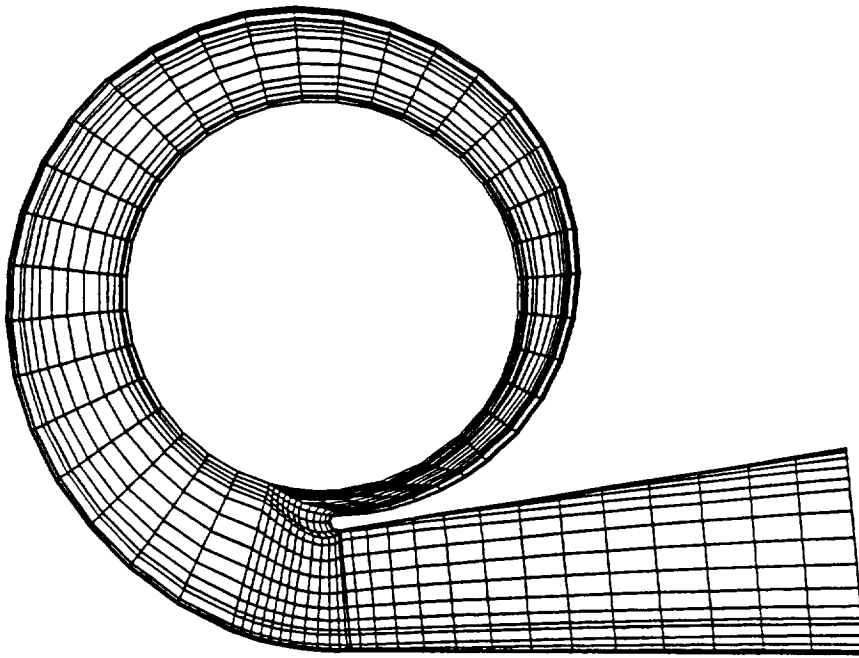Fig. 12 Exterior Surface of 3-D Grid, Used in Computation with Adkins-Brennen Model

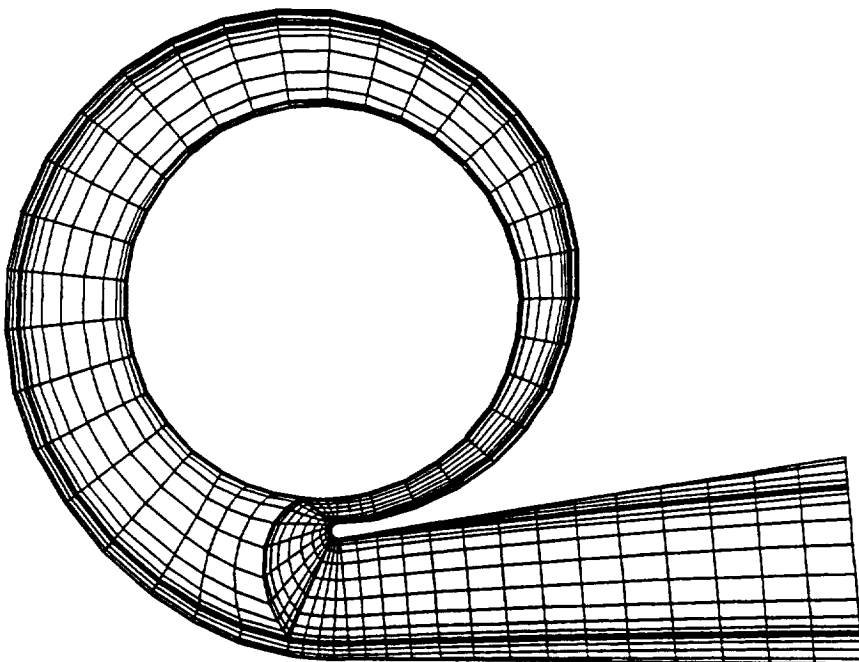Fig. 13 Exterior Surface of 3-D Grid, First Alternate Mapping

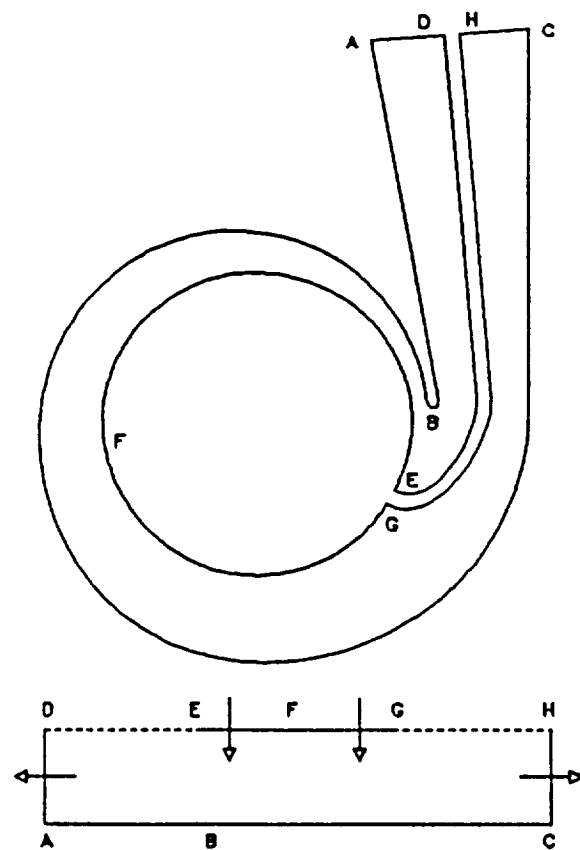Fig. 14 Exterior Surface of 3-D Grid, Second Alternate Mapping

16

Fig. 15 Physical to Computation Coordinate Mapping in 2-D Plane

sections. Then fiberglass was laid over the forms. With regard to constructing a grid of the volute, the criterion the craftsman had used to determine the shape of the wood forms and their actual surface profile is unknown. This lack of knowledge required that assumptions be made in the interpolation process for the Volute A surface.

Grids used for other volute geometries will be discussed subsequently.

3.0 CFD RESULTS

Most of the limiting assumptions made in analytical impeller/volute pump models can be relaxed by using current CFD technology. However, analyzing 3-dimensional flowfields, especially when zonal slip conditions at the impeller/volute interface must be accounted for, was recognized from the onset as being a very computationally intensive process. Therefore, 2-dimensional impeller/volute flows were analyzed initially to study the computational coupling at the moving interface. Upon successfully accomplishing such analyses, the full 3-dimensional simulation of the coupled impeller/volute flowfield was then computed. As expected, the simulation could be accomplished, but the expense of a single simulation prompted the development of a more practical solution method. The splitting of the analysis into a separate description of the impeller flow and of the volute flow appeared to be an excellent procedure for applying the CFD codes. Practically, one could use the impeller model and interface coupling parameter developed by Adkins and Brennen (1988) as inlet boundary conditions for the flow to the volute and construct the 3-dimensional CFD volute model. The Adkins and Brennen impeller/ volute model is summarized in Appendix A. This procedure was implemented, a substantial savings in computation time for a single simulation was realized, and parametric design studies for optimized volute configurations were accomplished. These CFD models were developed and results of the analyses made with the models are presented in the remainder of this section.

3.1 The FDNS CFD Impeller/Volute Pump Model

The FDNS CFD code, Chen (1989), simulates 3-dimensional, turbulent flows with the

18

accuracy required to predict the losses due to the unsteadiness of the volute flow which is due to vortex shedding from impeller vanes and diffuser blades and the recirculation in the pump. FDNS treats the full range of flow speeds from incompressible to hypersonic; hence, the description of either water or dense hydrogen gas required no new development. The simultaneous treatment of impeller and volute flow requires interpolation across a zonal boundary; a feature of the FDNS code available when this study started, Chen (1988). In short, the FDNS flow solver is mature and required no further development for application to impeller/volute interaction analysis.

Once it can be demonstrated that the steady radial forces can be accurately predicted for a given configuration, the question can be addressed: How can the volute/diffuser geometry be modified to reduce these forces? The design tool reported herein provides the methodology for varying the configuration to minimize or control the side forces. Since such a design tool did not previously exist, the predictive capability was developed, and the entire procedure demonstrated by actually designing a test volute, constructing the configuration, and measuring its performance to verify the design tool.

The conservation equations solved to simulate the impeller/volute interaction are given below in curvilinear coordinates. (Note the nomenclature used in these equations is completely independent of that used to describe the Adkins/Brennen model described in Appendix A.)

$$J^{-1}(\partial \rho q/\partial t) = \partial[-\rho U_i q + \mu G_{ij}(\partial q/\partial \xi_j)]/\partial \xi_i + S_q \qquad (1)$$

Where $q = 1$, u, v, w, k, and ϵ represent, respectively, mass, momentum, turbulent kinetic energy, and turbulent kinetic energy dissipation. J, U_i, and G_{ij} are given by

$$J = \partial(\xi,\eta,\zeta)/\partial(x,y,z)$$

$$U_i = (u_j/J)(\partial \xi_i/\partial x_j)$$

$$G_{ij} = (\partial \xi_i/\partial x_k)(\partial \xi_j/\partial x_k)/J$$

Also, $\mu = (\mu_l + \mu_t)/\sigma_q$ is the effective viscosity when the turbulent eddy viscosity is used to model turbulent flows. The turbulent eddy viscosity is $\mu_t = \rho C_\mu k^2/\epsilon$; C_μ and σ_q are turbulent modeling constants. Wall functions are used to reduce the number of grid points which are required very near the wall. Near wall turbulence models are impractical and unnecessary for the computations needed to simulate volute/impeller flow in pumps. Appropriate fluid properties for water, LOX, or dense gaseous hydrogen are used directly, either in tabular form or as suitable equations of state. The source terms are given by:

$$S_q = \frac{1}{J} \begin{bmatrix} 0 \\ -P_x + \nabla[\mu(u_j)_x] \\ -P_y + \nabla[\mu(u_j)_y] \\ -P_z + \nabla[\mu(u_j)_z] \\ \rho(P_r - \epsilon) \\ (\rho\epsilon/k)(C_1 P_r - C_2 \epsilon + C_3 P_r^2/\epsilon) \end{bmatrix}$$

An upwind scheme is used to approximate the convective terms of the momentum, energy, and continuity equations; the scheme is based on second and fourth order central differencing with artificial dissipation. First order upwinding is used for the turbulence equations. Different eigenvalues are used for weighing the dissipation terms depending on the conserved quantity being evaluated, in order to give correct diffusion fluxes near wall boundaries. For simplicity, consider fluxes in the ξ-direction only. That is:

$$\partial F/\partial \xi \approx 0.5(F_{i+1} - F_{i-1}) - (d_{i+0.5} - d_{i-0.5}) \tag{2}$$

A general form of the dissipation term is given as follows.

$$d_{i+0.5} = 0.5[\epsilon_1 |\rho U|]_{i+0.5}(q_{i+1} - q_i) + [\epsilon_2(1-\epsilon_1)MAX\{0.5\Delta S\rho(|u|,|v|),$$
$$2|\rho U|\} + \epsilon_3 \Delta S]_{i+0.5}(q_{i-1} - 3q_i + 3q_{i+1} - q_{i+2}) \tag{3}$$

Different values for ϵ_1, ϵ_2, and ϵ_3 are used for the continuity, energy and momentum equations, as shown in Table 1.

Table 1. Dissipation Parameters		
	Momentum & Energy	Continuity
ϵ_1 ϵ_2 ϵ_3	d_1 0.015 0	0 0 d_3
where: d_1 = REC and d_3 = 0.005		

To maintain time accuracy, a time-centered, time-marching scheme with a multiple pressure corrector algorithm is employed. In general, a noniterative time-marching scheme was used for time dependent flow computations; however, subiterations can be used if necessary. The pressure corrector scheme is described as follows. A simplified momentum equation was combined with the continuity equation to form a pressure correction equation. This equation is:

$$\partial \rho u_i / \partial t \simeq - \nabla p'$$

or in discrete form:

$$u_i' \simeq - \beta (\Delta t / \rho) \nabla p' \tag{4}$$

where β represents a pressure relaxation parameter ($\beta = 10$ is typical). The velocity field in the continuity equation is then perturbed to form a correction equation. That is:

$$\nabla (\rho u_i)^{n+1} = \nabla [\rho^n (u_i^n + u_i')] = 0$$

or,

$$\nabla (\rho u_i') = - \nabla (\rho u_i)^n \tag{5}$$

Substituting equation (4) into (5), the following pressure correction equation is obtained.

$$- \nabla(\beta \Delta t \, \nabla p') = - \nabla(\rho u_j)^n \tag{6}$$

Once the solution of equation (6) is obtained, the velocity field and the pressure field are updated through equation (4) and the following relation.

$$p^{n+1} = p^n + p'$$

To ensure that the updated velocity and pressure fields satisfy the continuity equation, the pressure correction procedure is repeated several times (usually 4 times is sufficient) before marching to the next time step. This constitutes a multi-corrector solution procedure.

The velocity through the impeller is calculated relative to the impeller, transformed to a fixed coordinate system at the impeller exit, and passed to the volute as a boundary condition along a zonal boundary. Since the grid points across the zonal boundary do not have a one-to-one correspondence, a linear interpolation is used for the overlaid grid points. The interpolation scheme along the zonal interface is applied implicitly inside the matrix solver to obtain better convergence.

3.2 2-D Volute Simulation

A general unsteady impeller/diffuser interface boundary condition treatment was developed and tested. The current model can be employed for steady-state or transient computations; however, the transient simulation would be very computationally intensive. A 2-D impeller/diffuser test case of Caltech, see Appendix A, was used to develop the computational model. The Caltech impeller geometry includes a logarithmic spiral blade shape and several diffuser vane profiles. For this study, a general cyclic boundary condition treatment was also implemented, based on multi-zone zonal interface solution procedures. This allows the use of patched cyclic boundaries without overlaid grids.

To establish a feasible procedure for optimizing the volute pressure distribution based on CFD analysis, a generic 2-D volute test case was generated. A 2-zone volute model was

formulated with the outer wall contour adjustable through a shape function. The objective of this calculation was to find a volute outer wall shape that will minimize the net force on the impeller.

For the 2-D volute test case, the side force optimization algorithm was tested. The objective function to be minimized is the force on the impeller and the independent variable is the volute spiral angle. A relaxed version of Newton's iteration method and a method using parabolic interpolation were tested. The impeller was replaced by a boundary condition of constant total pressure upstream of the diffuser. Figures 16-17 show the pressure contours and velocity vectors for the initial volute geometry. After every geometry perturbation, some number of iterations are required for a converged solution. For this test, the slope of the force versus spiral angle was evaluated every 200 time steps, and the geometry updated. Figures 18-19 show the pressure contours and velocity vectors after 8000 time steps using Newton's method. The iteration history of the force is given in Fig. 20. Due to the non-linear nature of the system, Newton's method produces severe over-shoots and under-shoots which leads to slow convergence towards a minimum side force geometry. The second method using parabolic interpolation was more robust. Figure 21 compares the iteration history for both methods. The feasibility of the impeller/diffuser flowfield coupling simulation was established, but it was not practical to continue the calculation to optimize the spiral angle by CFD simulations alone.

The unsteady impeller/diffuser vane interaction simulation was investigated for this same 2-D configuration. A relatively small time step size was used for time accuracy. 5260 time steps were integrated for one impeller blade passage. The extended two-equation turbulence model was employed for the turbulent flow computation. Pressure contours of the flowfield solution after four blade passages are shown in Fig. 22. The pressure time history on three vane surfaces near the leading edge are plotted in Fig. 23, for the last blade passage cycle. It is known that for this 5:9 blade ratio, the true periodicity is one complete impeller revolution.

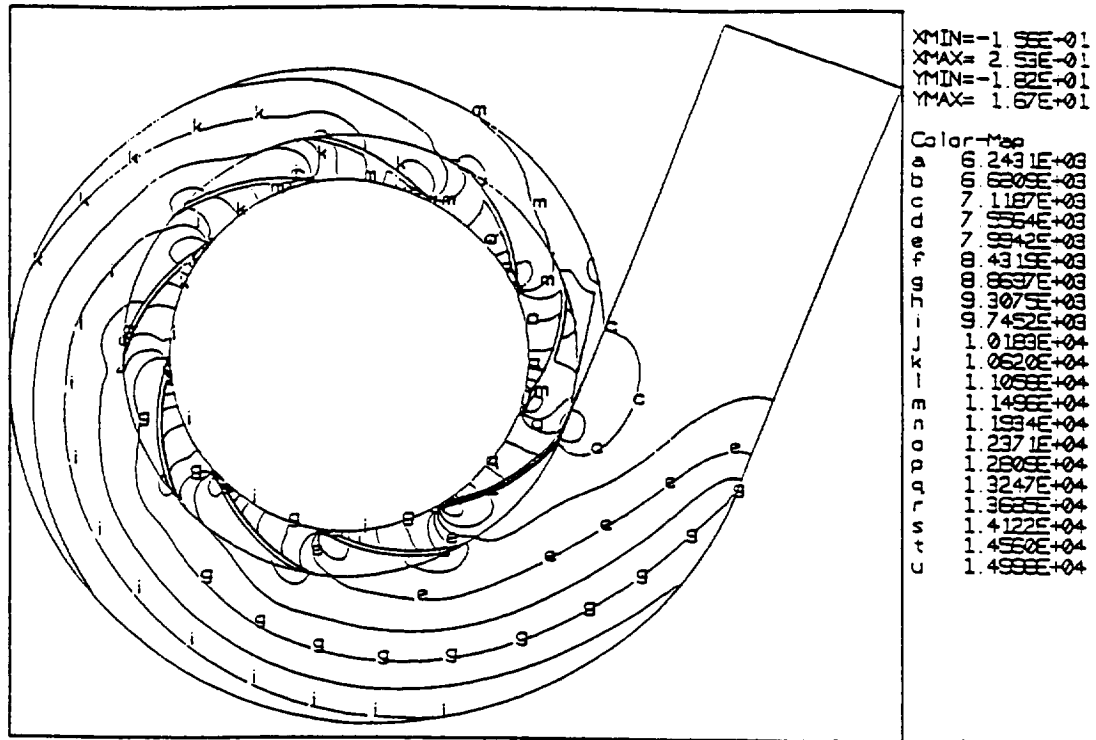The computation was extended to eight blade passage cycles. Pressure contours of the

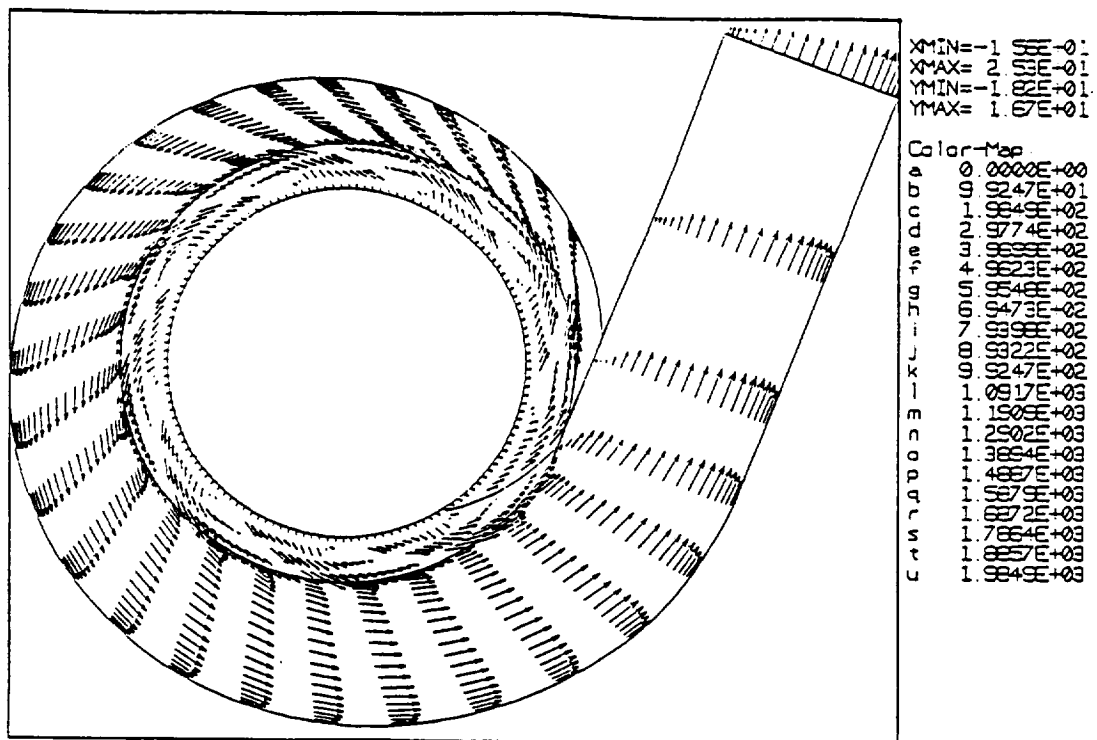Fig. 16 Pressure Contours of the Initial Volute Geometry

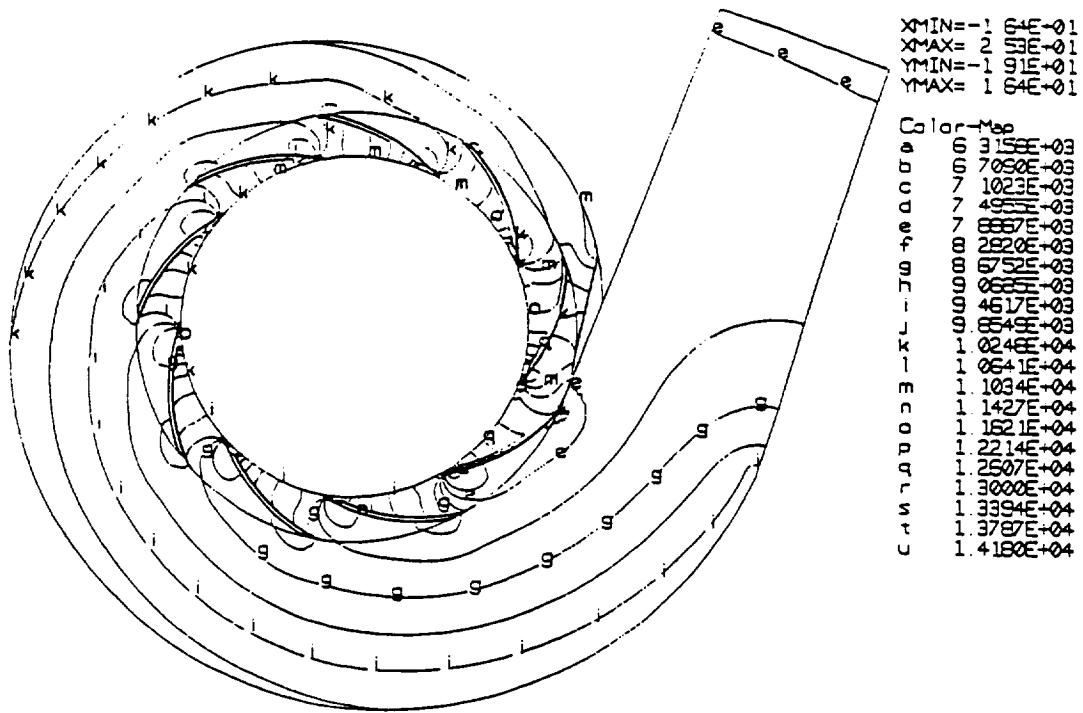Fig. 17 Velocity Vectors of the Initial Volute Geometry

XMIN=-1 64E-01
XMAX= 2 53E-01
YMIN=-1 91E+01
YMAX= 1 64E+01

Color-Map
a   6 315E+03
b   6 709E+03
c   7 102E+03
d   7 495E+03
e   7 888E+03
f   8 282E+03
g   8 675E+03
h   9 068E+03
i   9 461E+03
j   9 854E+03
k   1 024E+04
l   1 064E+04
m   1 103E+04
n   1 142E+04
o   1 182E+04
p   1 221E+04
q   1 260E+04
r   1 300E+04
s   1 339E+04
t   1 378E+04
u   1 418E+04

Fig. 18 Pressure Contours of the Optimized Volute After 8000 Time Steps

XMIN=-1 64E-01
XMAX= 2 53E-01
YMIN=-1 91E+01
YMAX= 1 64E+01

Color-Map
a   0 0000E+00
b   8 7243E+01
c   1 744E+02
d   2 617E+02
e   3 497E+02
f   4 362E+02
g   5 234E+02
h   6 107E+02
i   6 979E+02
j   7 851E+02
k   8 7243E+02
l   9 596E+02
m   1 046E+03
n   1 134E+03
o   1 221E+03
p   1 308E+03
q   1 395E+03
r   1 483E+03
s   1 570E+03
t   1 657E+03
u   1 744E+03
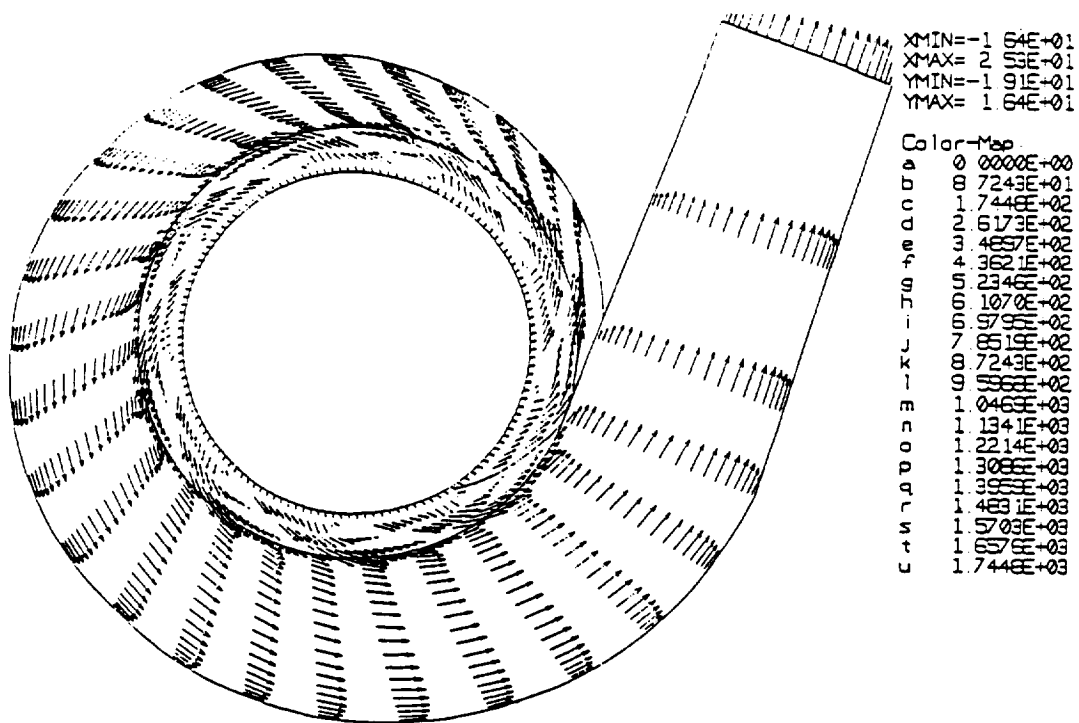
Fig. 19 Velocity Vectors of the Optimized Volute After 8000 Time Steps

25
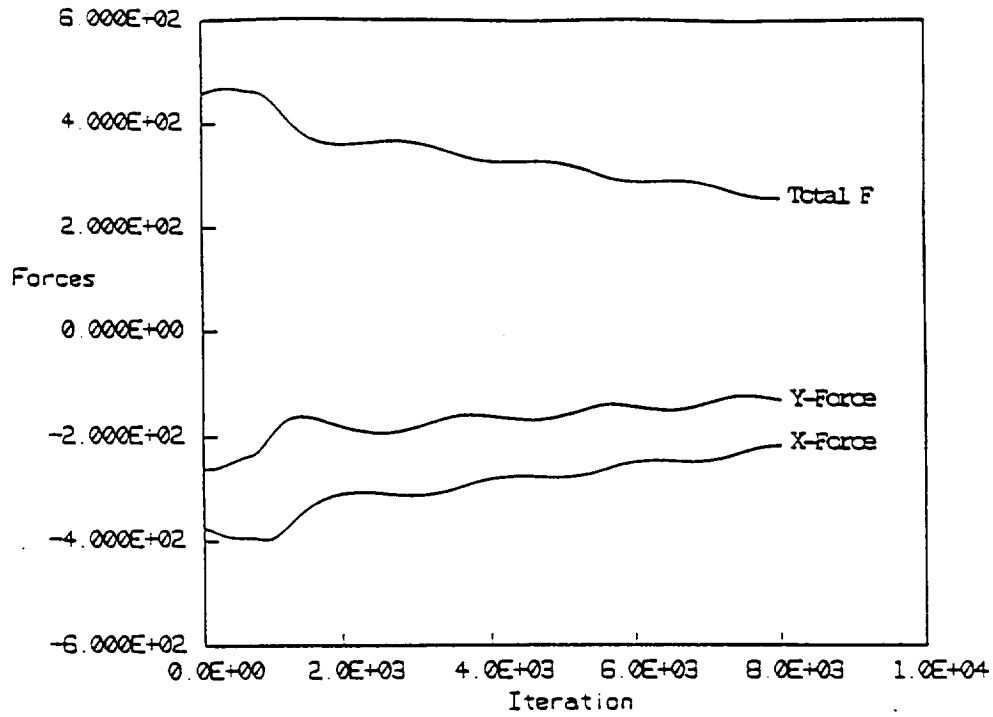
Fig. 20 Time Step History of the Force Using Newton's Method, Relaxed
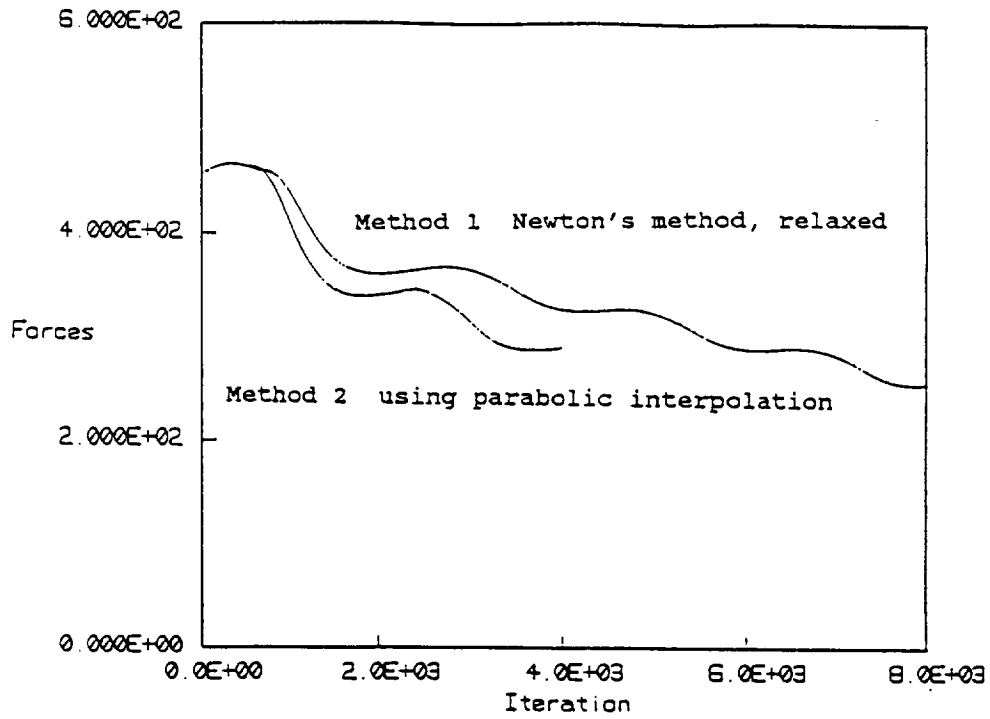
Fig. 21   Comparison of the Time Step History of the Force for the Optimization Algorithms Tested
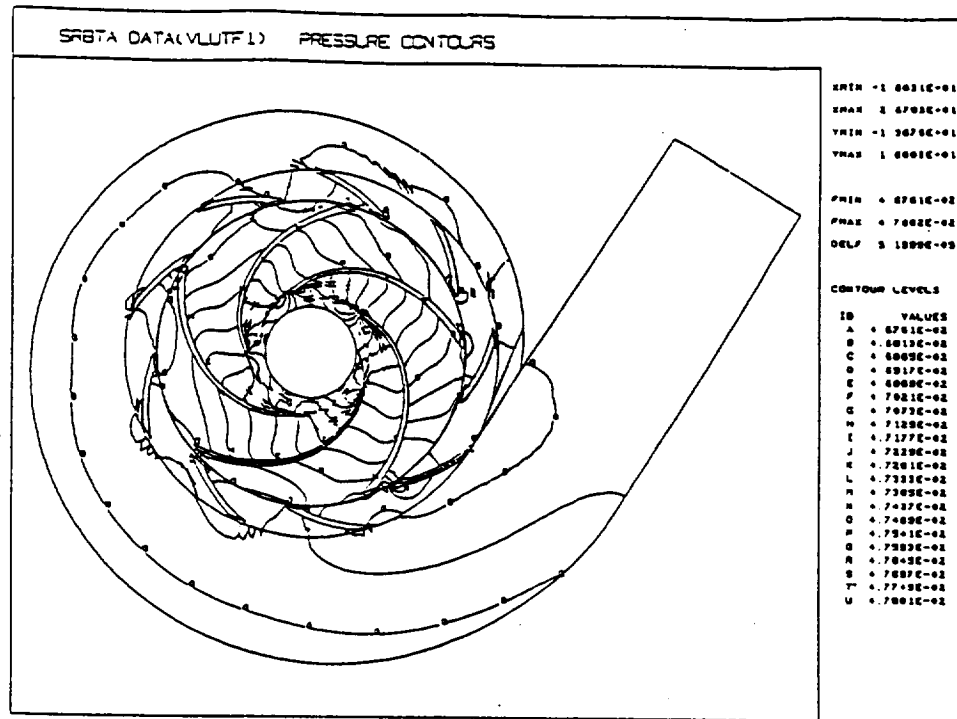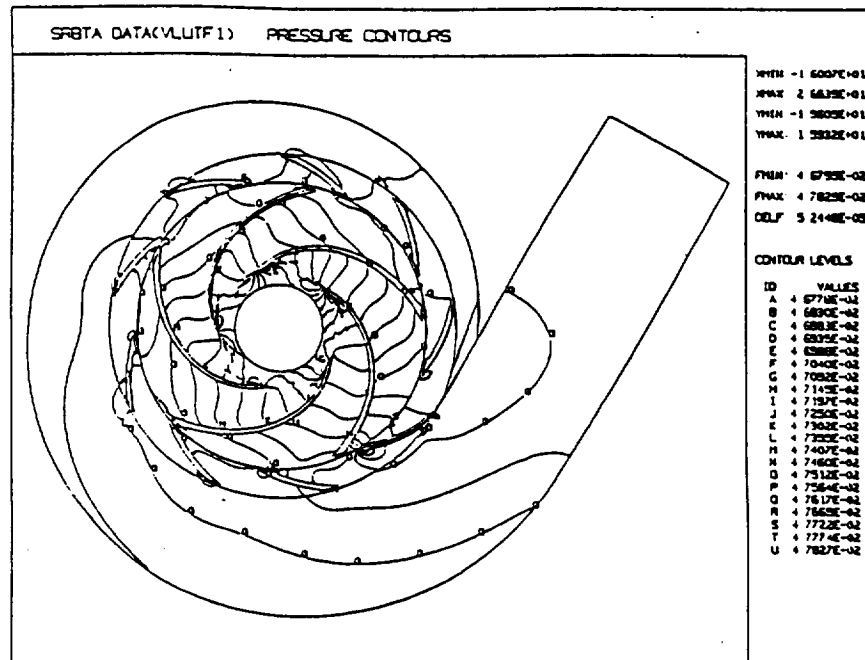
Fig. 22 Pressure Contours of the Impeller/Volute Test Case
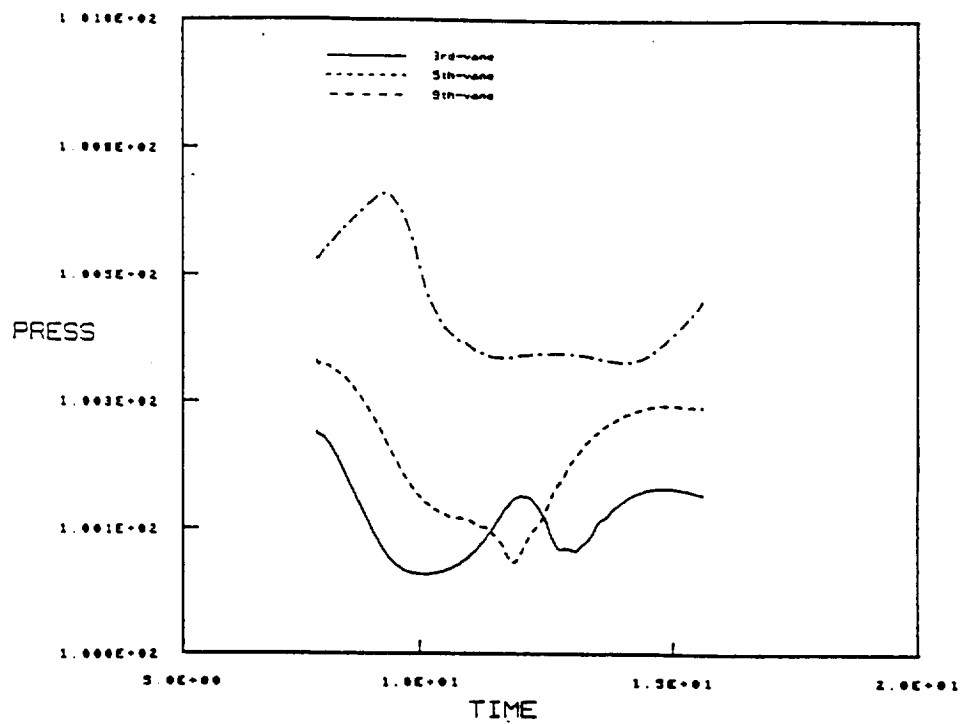
Fig. 23   Pressure Time History Near the Leading Edge of Selected Volute Vanes Over
One Blade Passage Cycle of the Impeller/Volute Test Case

27

flowfield solution are shown in Fig. 24. Figure 25 shows the time history of the pressure on the leading edges of three diffuser vanes over the last six blade passage cycles. The effect of the initial guess is still evident in the pressure history. More computation cycles are required to wash-out the low frequency disturbances. The unsteady simulation is feasible, but the number of impeller cycles required to obtain a quasi-steady flow is excessive.

3.3 3-D CFD Simulation of Volute A

The flowfield for Volute A, shown in Fig. 4, was simulated for two representations of the flow from Impeller X, shown in Fig. 5. The first simulation was for boundary conditions upstream of the impeller and yielded a fully coupled CFD impeller flowfield prediction. The coupling consisted of interpolating the impeller exit conditions to serve as the volute inlet conditions across the zonal interface as described in section 3.1. The second simulation consisted of using the Adkins/Brennen impeller model and interface matching parameter, β, to approximate the impeller/volute coupling. The results of these predictions are given in the following two subsections.

3.3.1 CFD Simulation of Both Volute A and Impeller X

To utilize an inlet boundary upstream of the impeller, grids for the impeller and the volute were generated, and the coupled impeller/volute flow was calculated. The impeller grid and the volute grid are shown in Figs. 26 and 27, respectively.

The flowfield computation was simulated for the design flow coefficient of $\varphi = .092$. Figures 28 and 29 show the pressure contours and velocity vectors after 6 impeller revolutions. The solution is not yet periodic, indicated by the impeller force iteration history shown in Fig. 30 for the last 3 impeller revolutions (3000 iterations).

The volute discharge exit was extended further downstream to enclose the recirculation region that had been observed in the design flow coefficient, $\varphi = .092$, computation, and the computation continued. Figures 31 and 32 show the pressure contours and velocity vectors.

Fig. 24   Pressure Contours of the Impeller/Volute Test Case After Eight Blade Passage Cycles
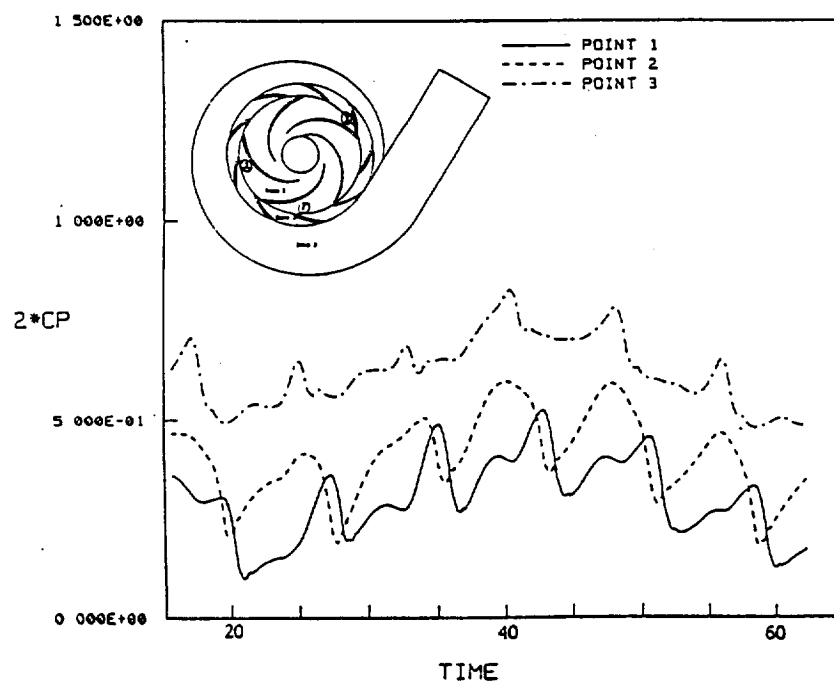

Fig. 25   Pressure Time History Near the Leading Edge of Selected Volute Vanes Over Six Blade Passage Cycles of the Impeller/Volute Test Case
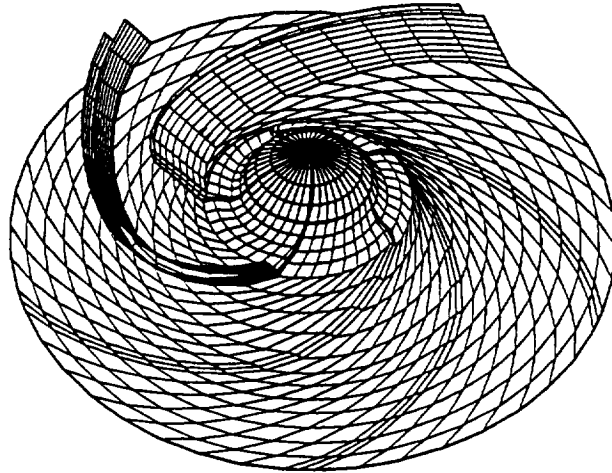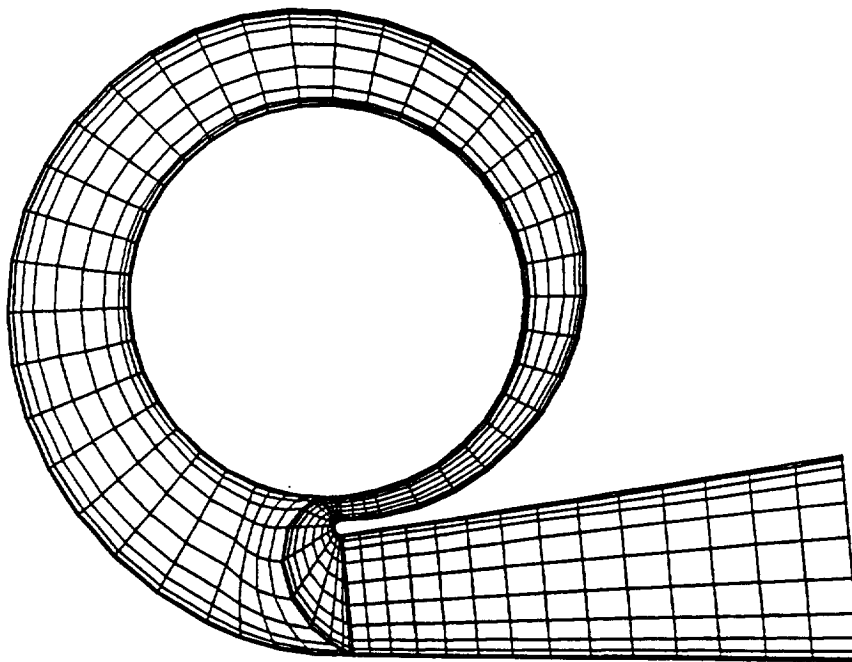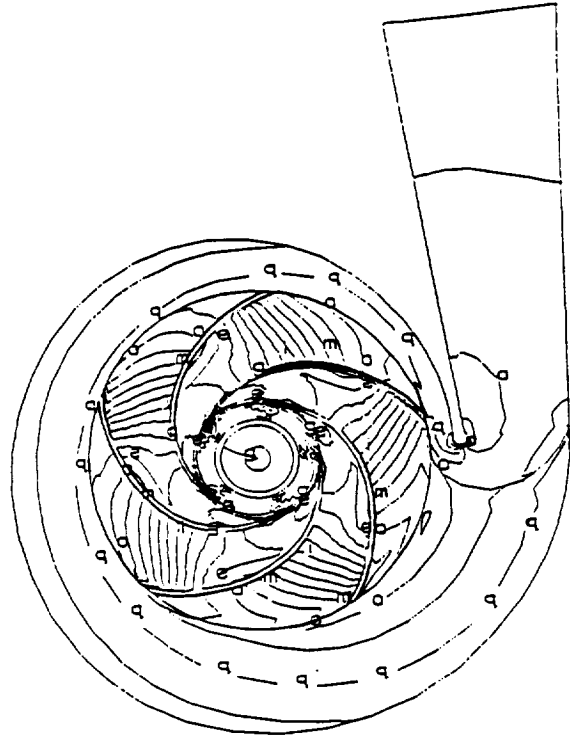
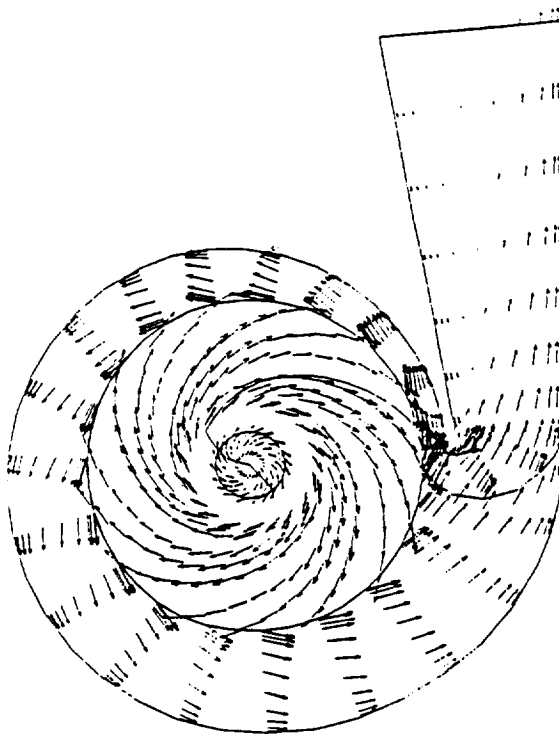Fig. 26 Impeller, Without Shroud, Showing Two Blades

Fig. 27 Volute Grid

XMIN=-7 525+00
XMAX= 8 555+00
YMIN=-5 185+00
YMAX= 8 565+00

Color-Map
a   9 2742E+01
b   9 4013E+01
c   9 5284E+01
d   9 6555E+01
e   9 7826E+01
f   9 9097E+01
g   1.0036E+02
h   1.0163E+02
i   1.0291E+02
j   1.0418E+02
k   1.0545E+02
l   1.0672E+02
m   1.0799E+02
n   1.0926E+02
o   1.1053E+02
p   1.1180E+02
q   1.1307E+02
r   1.1435E+02
s   1.1562E+02
t   1.1689E+02
u   1.1816E+02

Fig. 28 Pressure Contours

XMIN=-7 95E+00
XMAX= 9 01E+00
YMIN=-5 54E+00
YMAX= 8 92E+00

Color-Map
a   0.0000E+00
b   2.7945E-01
c   5.5891E-01
d   8.3836E-01
e   1.1178E+00
f   1.3972E+00
g   1.6767E+00
h   1.9561E+00
i   2.2356E+00
j   2.5151E+00
k   2.7945E+00
l   3.0740E+00
m   3.3534E+00
n   3.6329E+00
o   3.9123E+00
p   4.1918E+00
q   4.4713E+00
r   4.7507E+00
s   5.0302E+00
t   5.3096E+00
u   5.5891E+00

Fig. 29 Velocity Vectors
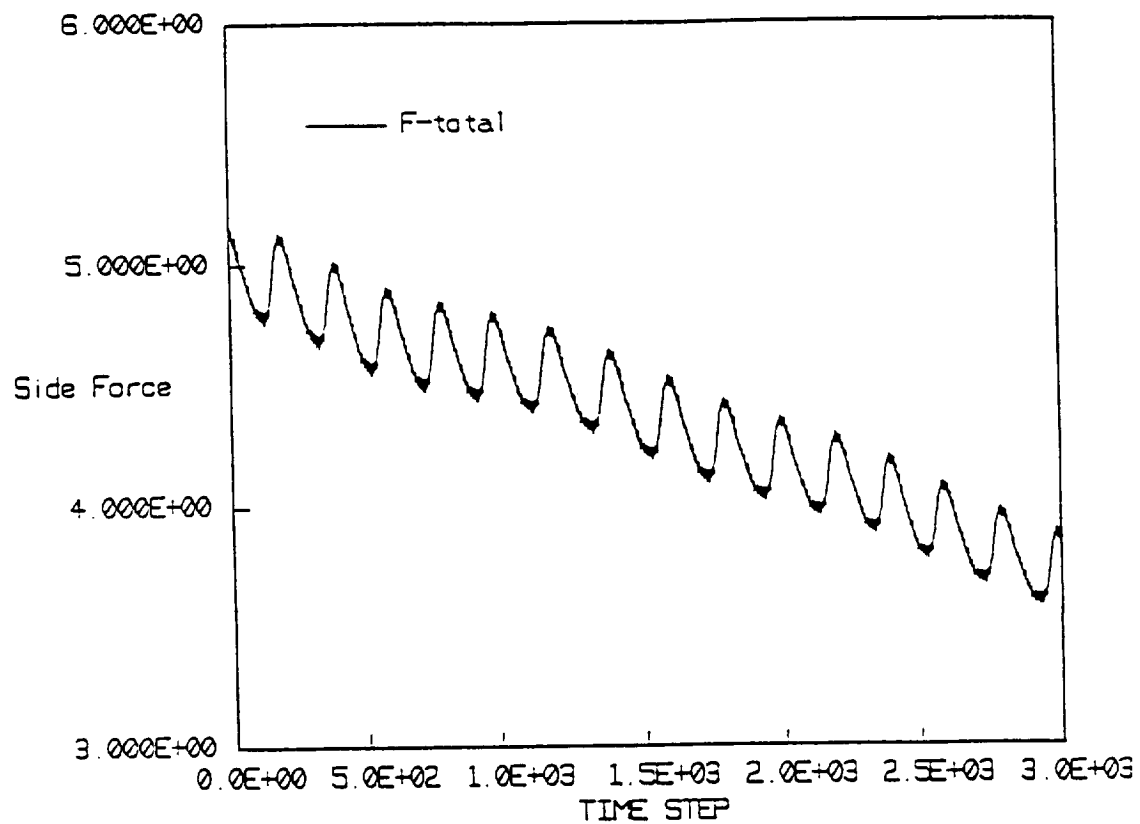
Fig. 30   Impeller Force Iteration History Over the Last 3 Impeller Revolutions, Using a
Non-Standard Non-Dimensionalization

```
XMIN=-1.57E+01
XMAX= 1.67E+01
YMIN=-5.18E+00
YMAX= 2.25E+01

Color-Map:
a    9.7348E+01
b    9.8595E+01
c    9.9843E+01
d    1.0109E+02
e    1.0233E+02
f    1.0358E+02
g    1.0483E+02
h    1.0607E+02
i    1.0732E+02
j    1.0857E+02
k    1.0982E+02
l    1.1106E+02
m    1.1231E+02
n    1.1356E+02
o    1.1481E+02
p    1.1605E+02
q    1.1730E+02
r    1.1855E+02
s    1.1979E+02
t    1.2104E+02
u    1.2229E+02
```

Fig. 31 Pressure Contours ϕ = .092


```
XMIN=-5.96E+00
XMAX= 7.02E+00
YMIN=-5.18E+00
YMAX= 5.89E+00

Color-Map
a    0.0000E+00
b    2.9183E-01
c    5.8367E-01
d    8.7551E-01
e    1.1673E+00
f    1.4591E+00
g    1.7510E+00
h    2.0428E+00
i    2.3347E+00
j    2.6265E+00
k    2.9183E+00
l    3.2102E+00
m    3.5020E+00
n    3.7938E+00
o    4.0857E+00
p    4.3775E+00
q    4.6694E+00
r    4.9612E+00
s    5.2530E+00
t    5.5449E+00
u    5.8367E+00
```

Fig. 32 Velocity Vectors ϕ = .092

The impeller force is calculated by integrating the pressure at the impeller exit. The force iteration history is shown in Figs. 33 and 34 for the last impeller revolution. Figure 33 shows the force magnitude and its components, F_x and F_y. The origin is at the volute center with the x-axis tangent to the tongue. Figure 34 is a plot of the magnitude of the force on an expanded scale, showing the fluctuation from the impeller blades passing the volute tongue. Figures 33 and 34 also indicate that a fully-coupled 3-D impeller/volute flowfield solution was obtained.

The calculations were repeated for a range of flow coefficients. The time averaged circumferential pressure profile, $c_p(\theta) = \dfrac{p(\theta) - p_{inlet,s}}{.5 \; \rho u_2^2}$, on the shroud and hub sides (front and back,

respectively) of the volute at a radius ratio of $r/r_{impeller\;exit} = 1.08$ is shown in Fig. 35 for $\phi = .092$. The kink in p(θ) near $\theta = 15°$ was believed to be grid dependent. The transition between the fine grid near the tongue and the coarser grid around the spiral starting at $\theta = 15°$ was later modified. The calculated force components are shown in Fig. 36 with experimental values from Adkins and Brennen (1988). The experimental values were obtained by averaging the force measured by a rotating balance with the impeller placed at four positions 90° apart along a circular whirl orbit. The calculated F_x does not resemble the experimental values. If the kink in p(θ) is flattened, the calculated force was expected to be closer to the measured force.

Since the kink in the pressure profile mentioned was near $\theta = 15°$, where the transition between the fine grid near the tongue and the coarser grid around the spiral occurs, the transition was improved. The volute drawing was reviewed and some changes made to the grid. However, obtaining fully coupled solutions requires large amounts of computation time, therefore an alternate computation scheme was used to continue the investigation.
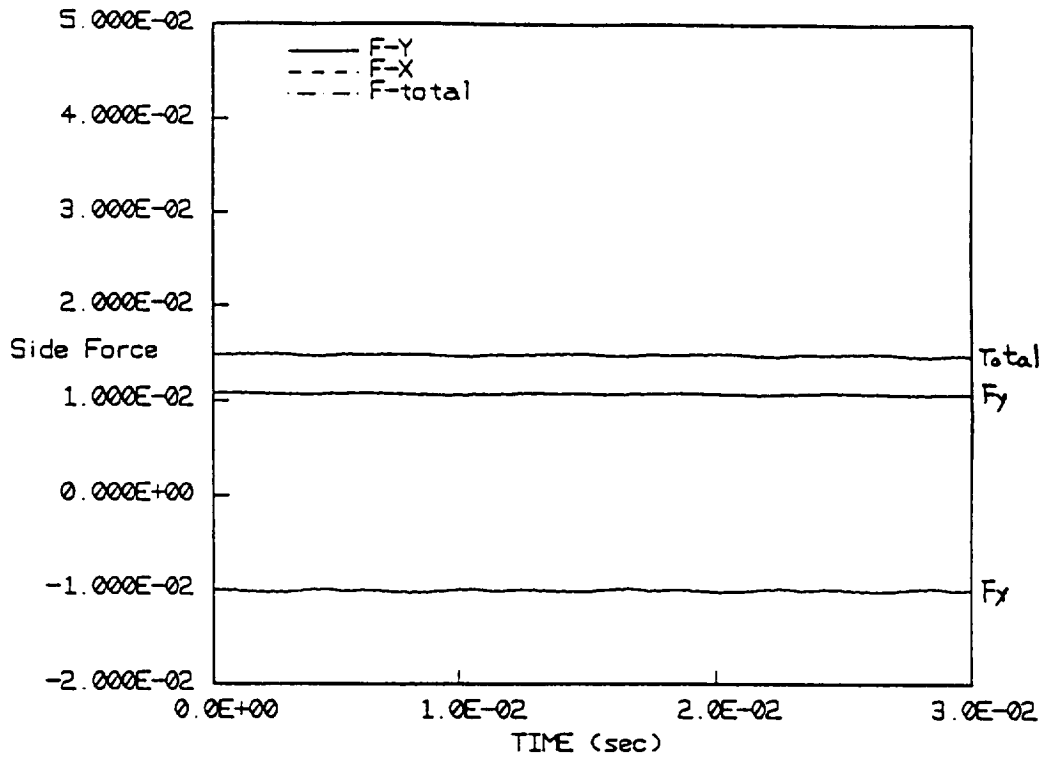
Fig. 33 Force, Magnitude and Components, Iteration History
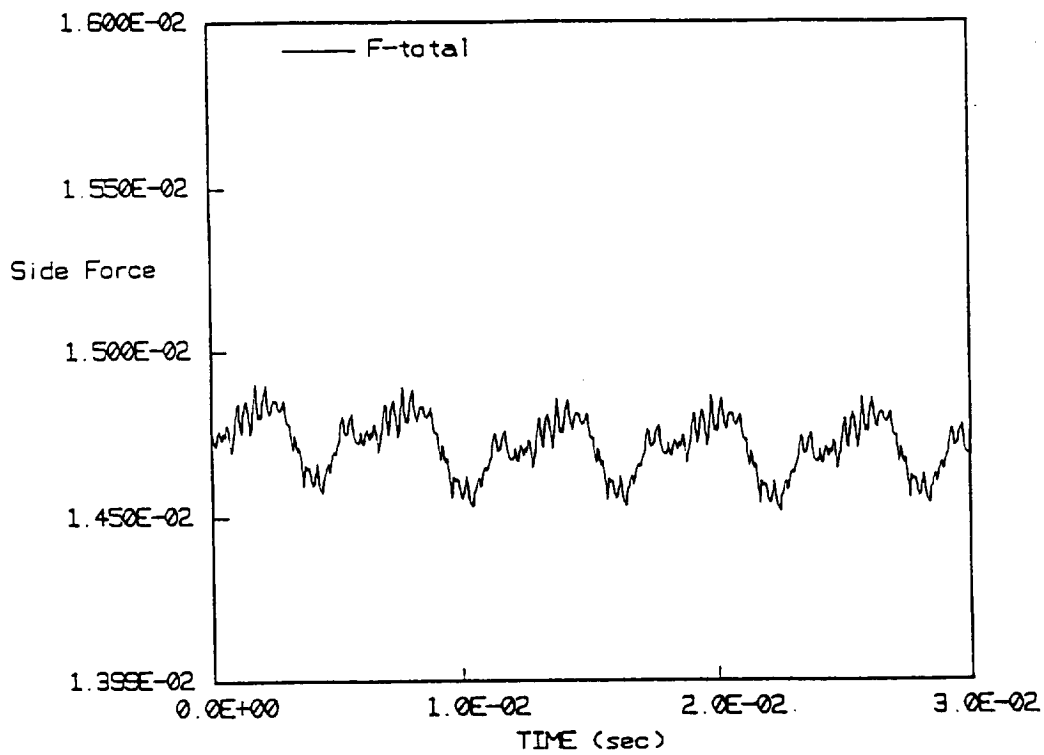
Fig. 34 Force Magnitude Iteration History, Expended Scale
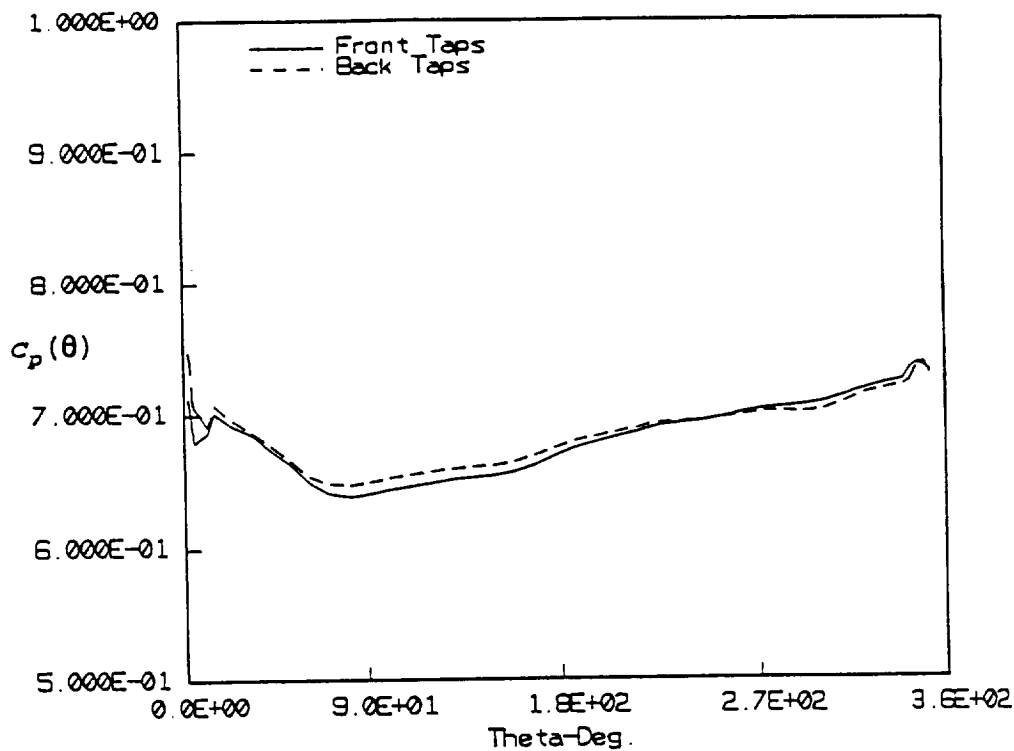
Fig. 35 Pressure Profile in the Volute, $\phi = .092$
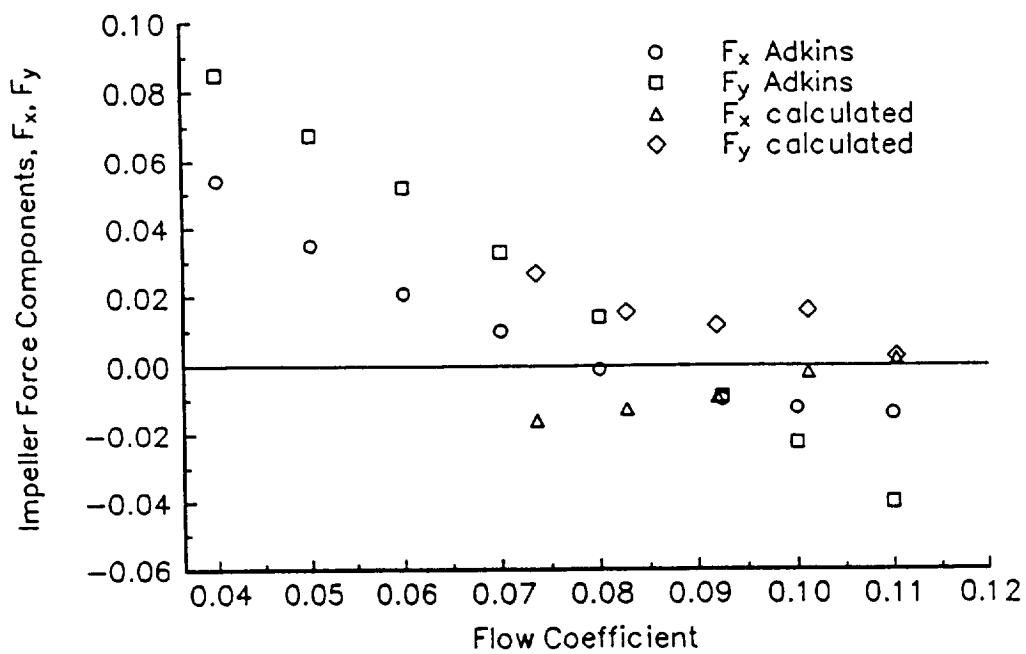
Fig. 36 Force Components as a Function of Flow Coefficient

36

3.3.2 CFD Simulation of Volute A using Adkins/Brennen's Model for Impeller X

To reduce computation time, the impeller grid was removed and Adkins/Brennen impeller model was used to establish the inlet boundary condition for the volute flowfield. The Adkins/Brennen impeller/volute pump model and the test data to which it has been compared is summarized in Appendix A. Briefly, the model assumes that the flow within the impeller follows a logarithmic spiral. Bernoulli's equation is integrated along this path. The Adkins/Brennen impeller/volute model will iterate to the spiral flow angle, given the head rise across the pump. The impeller model provides a relation between the pressure and relative velocity magnitude at the impeller/volute boundary in terms of a circumferential perturbation function, β. Equation A-6 in Appendix A is the differential equation which defines β. Using the experimental head rise across the pump from Adkins (1986), the impeller/volute model was used to calculate the spiral flow angle (γ) needed to use the impeller model as a boundary condition.

The results from calculations for three flow coefficients, $\phi/\phi_{design}=0.8$, 1.0, and 1.1 will be presented, where $\phi=.074$, .092, and .101, respectively. Figure 37 shows the exterior surface of the volute grid with the circumferential location labeled on which the pressure profile will be presented at a tap radius ratio of $r_{tap}/r_2 = 1.08$. The circumferential pressure profile, $\dfrac{p(\theta)-p(0)}{.5\ \rho u_2^2}$, on the shroud and hub sides (front and back, respectively) of the volute is shown in Fig. 38. Note that the offset is $p(\theta=0)$ in this figure. The kink near $\theta=350°$ is where the tap radius crosses the re-entrant flow boundary. The pressure, $\dfrac{p(\theta)-p_{t1}}{.5\ \rho u_2^2}$, measured by Adkins with the impeller placed on a circular whirl orbit of $r_{orbit}/r_2 = 0.016$ at the position nearest the volute tongue is in Fig. 39. No test data are available for a centered impeller. The calculated force components are shown in Fig. 40 with experimental values from Adkins (1986). The calculated pressure more closely matches the experiment than the fully coupled CFD solution presented in the previous section, consequently the force components are also closer to the
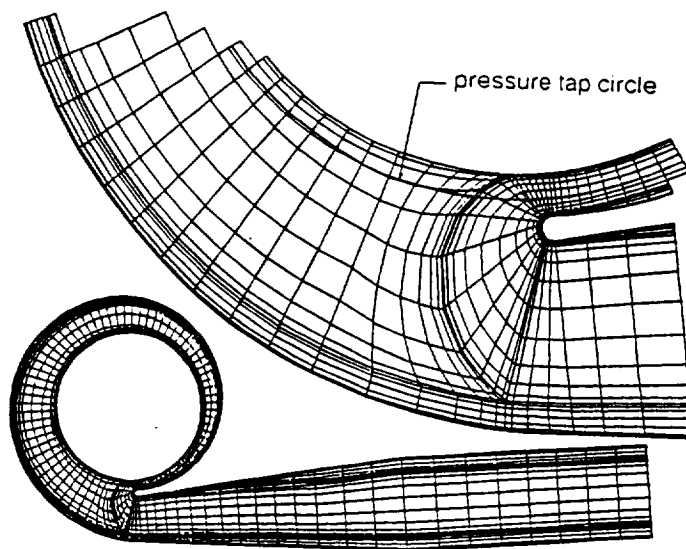
Fig. 37 Volute Grid, With Pressure Tap Circle Indicated
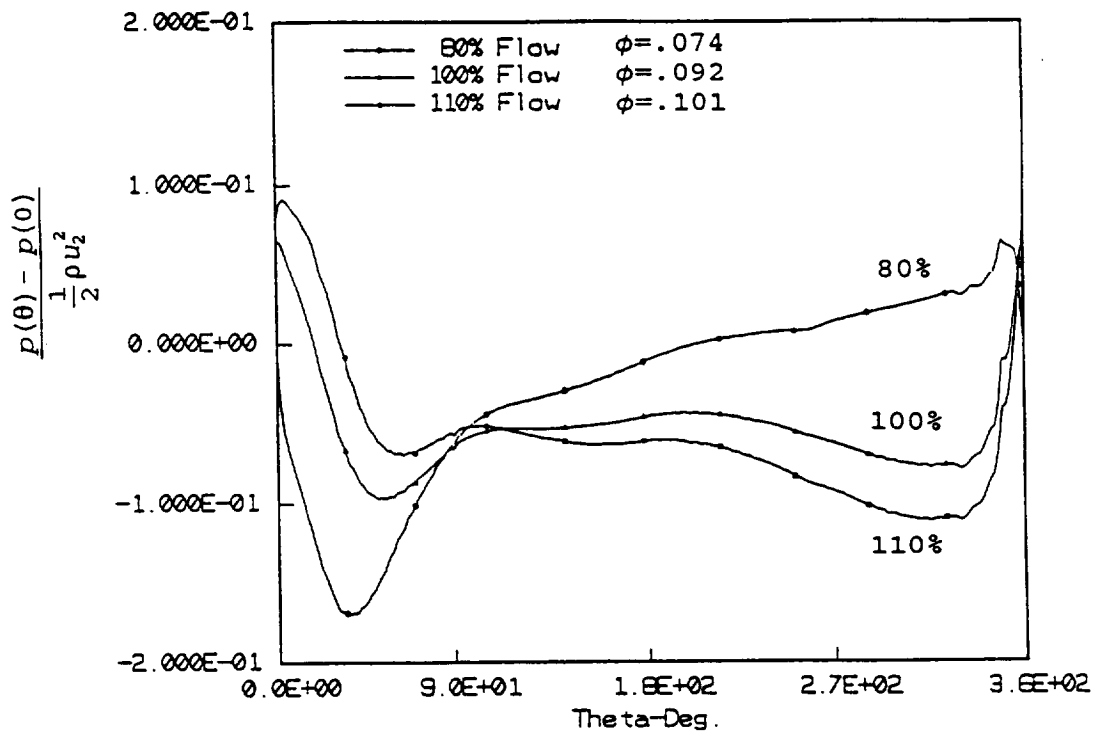
Fig. 38 Volute Pressure Profile, From Computation
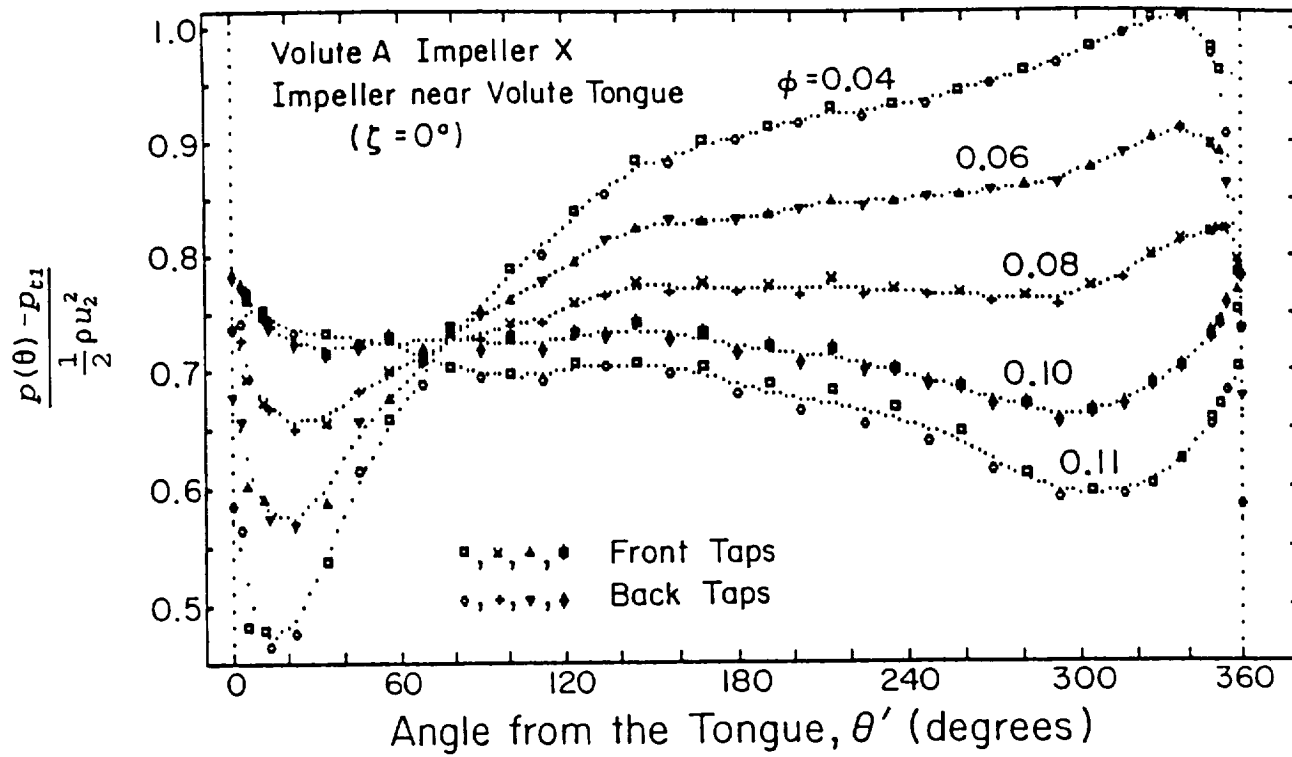
Fig. 39 Volute Pressure Profile, From Experiment (Adkins 1986)
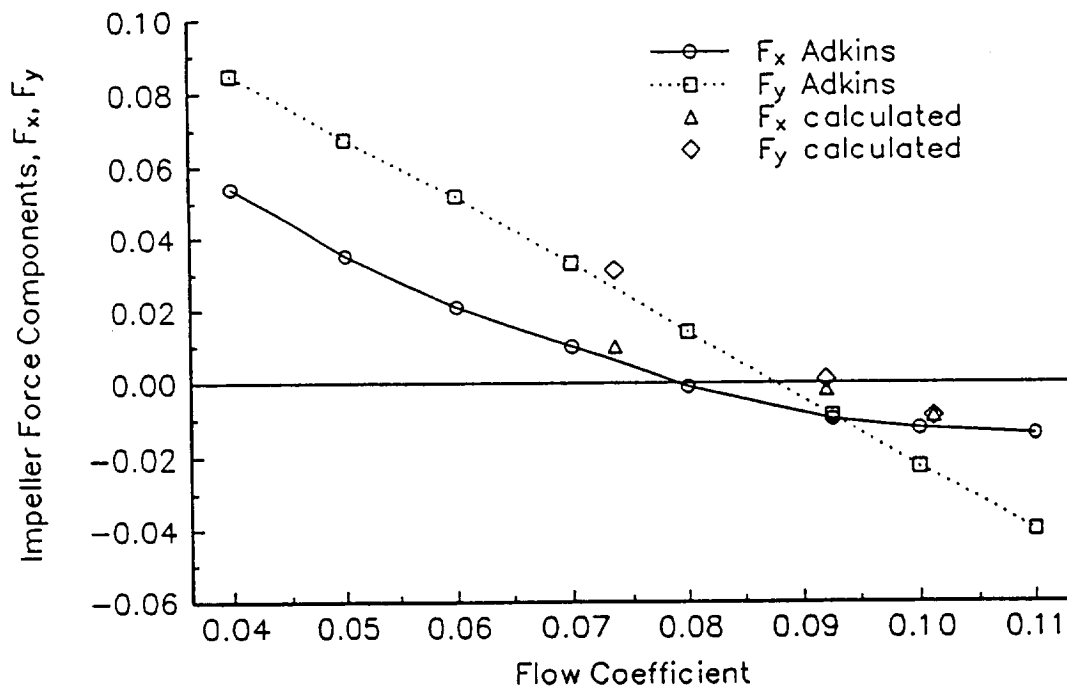
Fig. 40 Force Components as a Function of Flow Coefficient

measured values. For the design flow coefficient, $\phi = .092$, Figs. 41-42 show the pressure contours and velocity vectors. The relative velocity magnitude perturbation functions, $\beta(\theta,\gamma)$, from Adkins/Brennen impeller model used to specify the inlet velocity to the volute are given in Fig. 43. The functions obtained using both the Adkins/Brennen impeller and volute models are shown in Fig. 44.

These results were judged sufficiently accurate to warrant a parametric investigation of the effect of volute shape on radial forces. The spiral angle of the streamline relative to the impeller blade, γ, will, in general, not be known. For a postulated impeller and volute design, the fully coupled impeller/volute CFD solution should be used to provide γ for the design point of the pump. As mentioned previously, γ should be determined from the head curve for the pump, and it will be a function of the flow coefficient. However, it is a weak function of flow coefficient and may be assumed constant for modest volute variations and over a range of flow coefficients. For large variations in volute geometry, γ should be re-evaluated with the coupled CFD impeller/volute simulation at the design point (for each volute evaluated).

XMIN=-5.97E+00
XMAX= 7.02E+00
YMIN=-5.19E+00
YMAX= 5.89E+00

Color-Map:
a -7.0905E+00
b -6.4175E+00
c -5.7445E+00
d -5.0715E+00
e -4.3985E+00
f -3.7255E+00
g -3.0525E+00
h -2.3795E+00
i -1.7064E+00
j -1.0334E+00
k -3.6046E-01
l   3.1254E-01
m   9.8555E-01
n   1.6585E+00
o   2.3315E+00
p   3.0045E+00
q   3.6776E+00
r   4.3506E+00
s   5.0236E+00
t   5.6966E+00
u   6.3696E+00

Fig. 41 Pressure Contours ϕ = .092

XMIN=-5.97E+00
XMAX= 7.02E+00
YMIN=-5.19E+00
YMAX= 5.89E+00

Color-Map.
a   0.0000E+00
b   2.1478E-01
c   4.2957E-01
d   6.4436E-01
e   8.5915E-01
f   1.0739E+00
g   1.2887E+00
h   1.5035E+00
i   1.7183E+00
j   1.9331E+00
k   2.1478E+00
l   2.3626E+00
m   2.5774E+00
n   2.7922E+00
o   3.0070E+00
p   3.2218E+00
q   3.4366E+00
r   3.6514E+00
s   3.8662E+00
t   4.0809E+00
u   4.2957E+00

Fig. 42 Velocity Vectors ϕ = .092

41

Fig. 43   Relative Velocity Magnitude Perturbation Function, From Computation
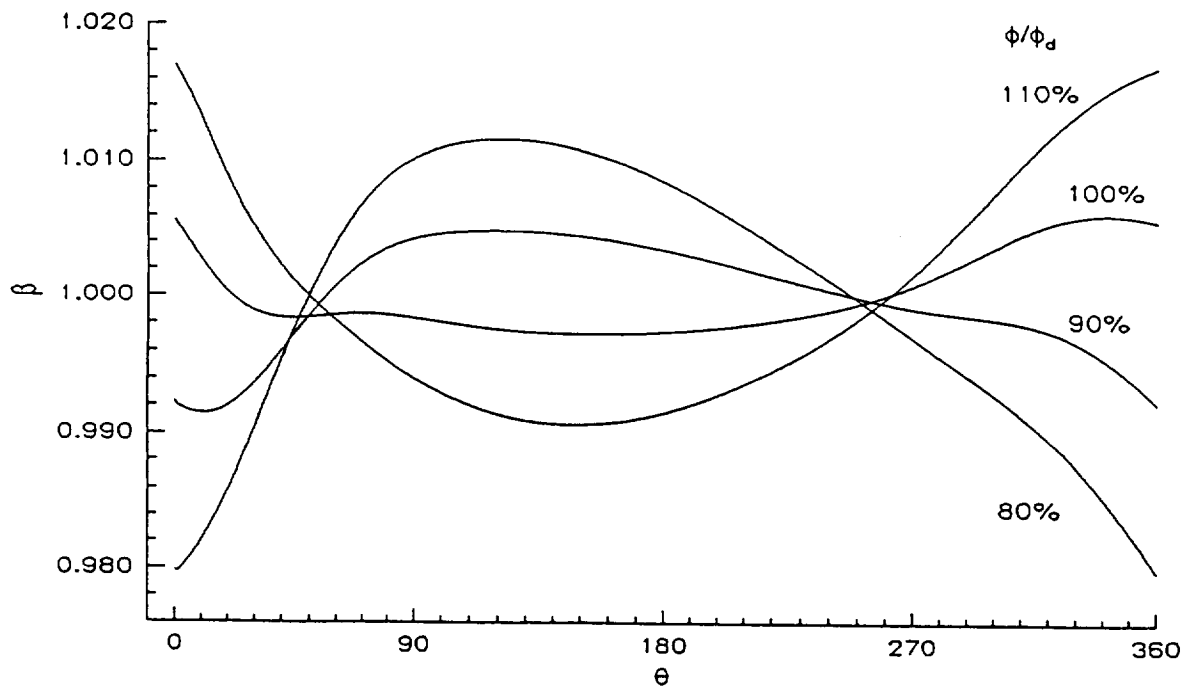
Fig. 44   Relative   Velocity   Magnitude   Perturbation   Function,   Using   Adkins'
Impeller/Volute Model

4.0 DESIGN OF A TEST VOLUTE

Even though a small number of parameters are required to specify the volute shape with the volute grid code (the spiral shape and the angle of the trapezoidal cross-section are the major parameters, with the filet radii and circular shape of the outside of the cross-section expected to be of minor importance), a large number of parametric cases would be required to obtain an optimum volute shape. Also, the primary focus of this study was to develop the design methodology, not to actually design volutes. Therefore, a limited set of parametric cases were analyzed, and an interesting, but not optimal, new volute was selected for testing to verify the methodology.

The predicted pressure distributions indicate that a major source of the radial forces are the pressure disturbances caused by the tongue. This suggests that the tongue geometry could be modified to reduce the separation in the discharge duct or that the spiral shape opposite the tongue could be distorted to balance the disturbance at the tongue. Of course, other strategies could be used. The promising shapes indicated by the experimental data shown in Fig. 3 could be investigated. Unfortunately, the specific volute geometries tested to produce Fig. 3 were not reported; therefore, the entire reconfiguring of the volute would have to be re-done. Due to the finite funding available for this study, the concept of reducing the tongue distortion and balancing this effect with volute geometry changes opposite the tongue were the only optimization factors considered.

4.1 Parametric Studies

Changes were made to the Volute A surface to investigate their effect upon the force on the impeller. The four volute geometries evaluated are summarized in Table 2. Since these geometries are quite similar to Volute A, the value of γ was held constant. The flowfields for four flow coefficients: $\phi = .074, .083, .092,$ and $.101$ were calculated.

Table 2. Volute geometries				
case	label	cross-section interpolation method	modified tongue	spiral contour
1	baseline	spline	no	spline
2	modified tongue	spline	yes	spline
3	arch spiral 186±10 flat .5	f(Θ)	yes	Archimedian spiral
4	arch spiral 186±5	f(Θ)	yes	Archimedian spiral

For the first two cases presented, the surface of the spiral region was interpolated between the defined cross-sections using cubic splines. The defined cross-sections were obtained from the drawing of a Volute A, which had been tested at Caltech. For the first case, flow separation was observed on the discharge side of the tongue for all of the flow coefficients calculated. Consequently, the tongue contour on the discharge side was modified for the second case. For the above design flow coefficient, the flow separation was drastically reduced, and, for the other flow coefficients, entirely eliminated The modified tongue was kept for the subsequent cases. Since the same differences exist between the simulated and the measured forces for Volute A, the simulated forces were used for these parametric comparisons.

For the last two cases the spiral surface was described using the volute cross-section geometry previously presented, Fig. 6. The cubic spline which had described the spiral midplane contour was replaced by two Archimedian spirals connected with a two-point spline to smooth the transition. For the geometry labeled "arch spiral 186±10 flat .5" the spiral contour was flattened opposite the tongue. The spiral contour is shown Fig. 45-46 using Cartesian and polar coordinates, respectively. The cross-sectional area in the spiral region and its derivative with respect to θ are shown in Figs. 47-48. In Fig. 47, θ starts at the tip of the tongue; however, the tongue is not included in Fig. 48.

For each flow coefficient calculated, Fig. 49-52 shows the change in the circumferential
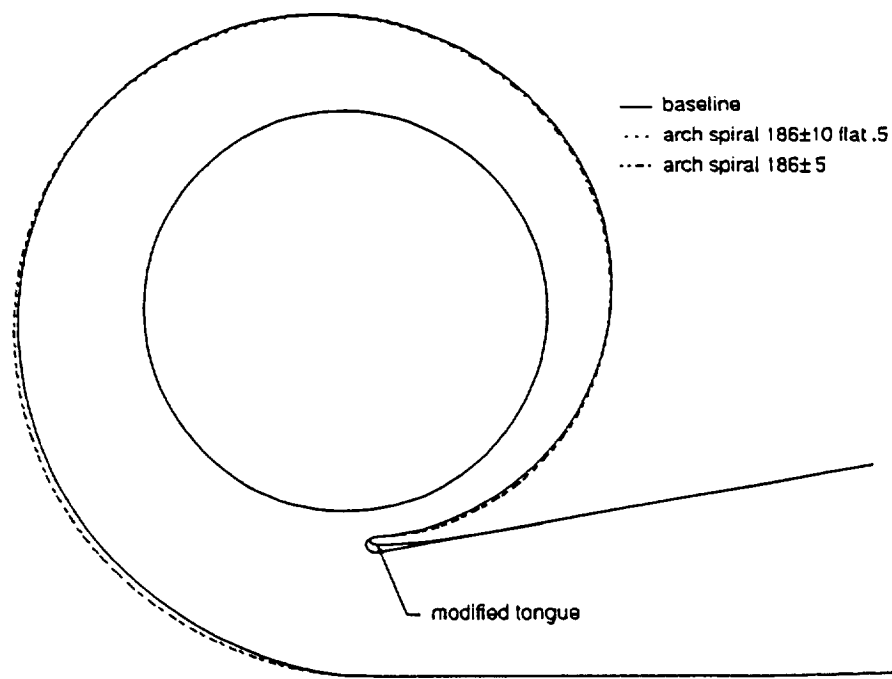
Fig. 45 Volute Midplane Contour
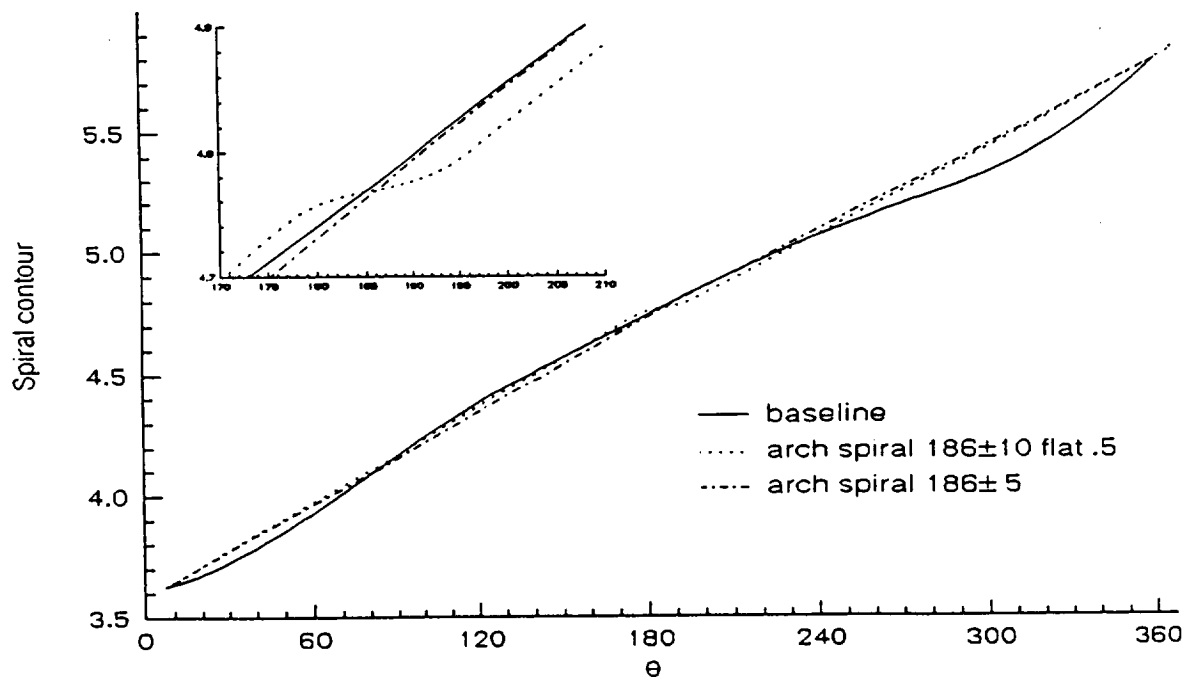
Fig. 46 Volute Spiral Contour
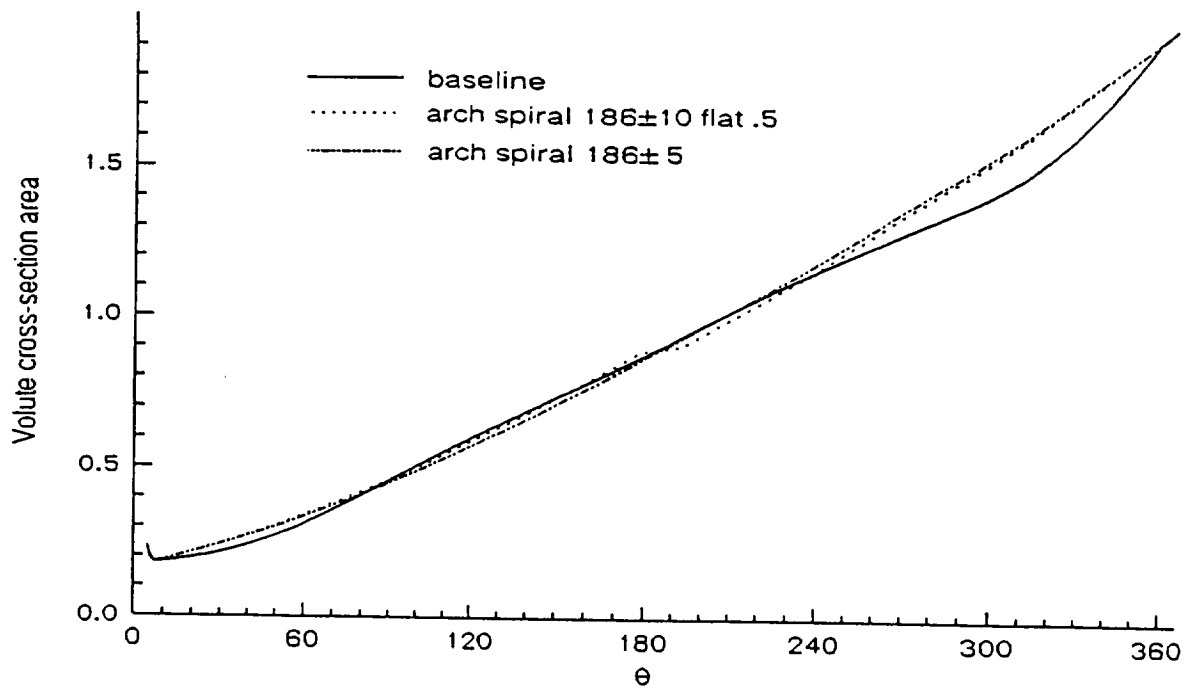
Fig. 47 Volute Cross-Section Area
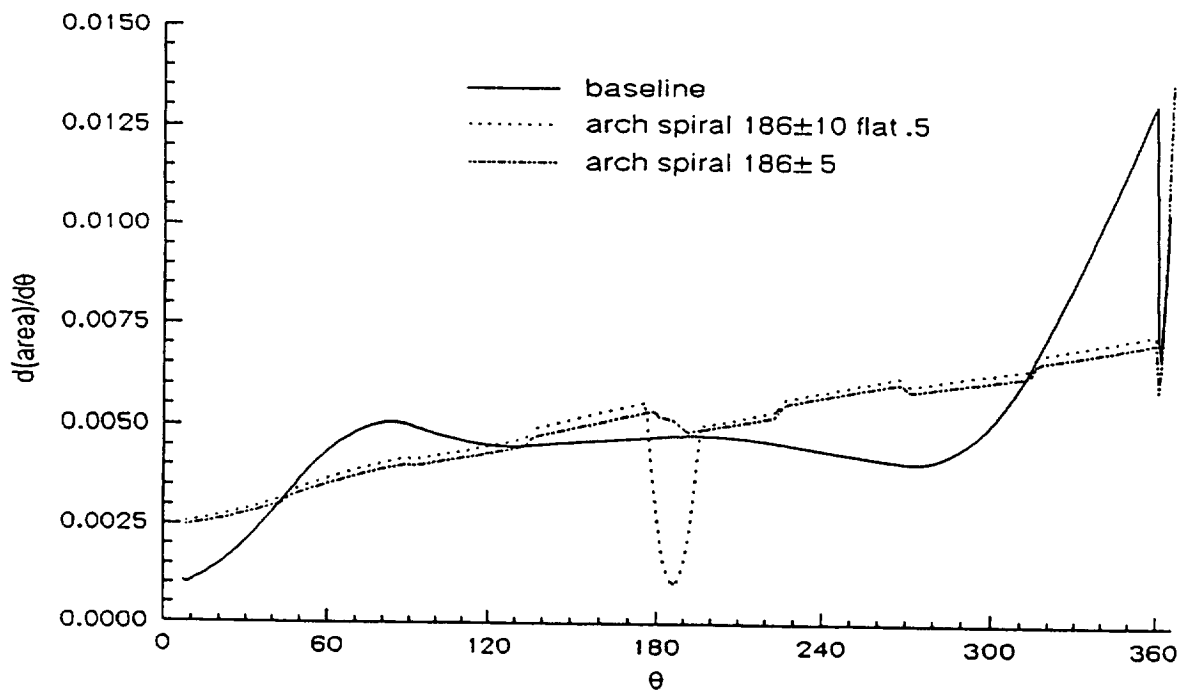
Fig. 48 Slope of the Volute Cross-Section Area With Respect to θ
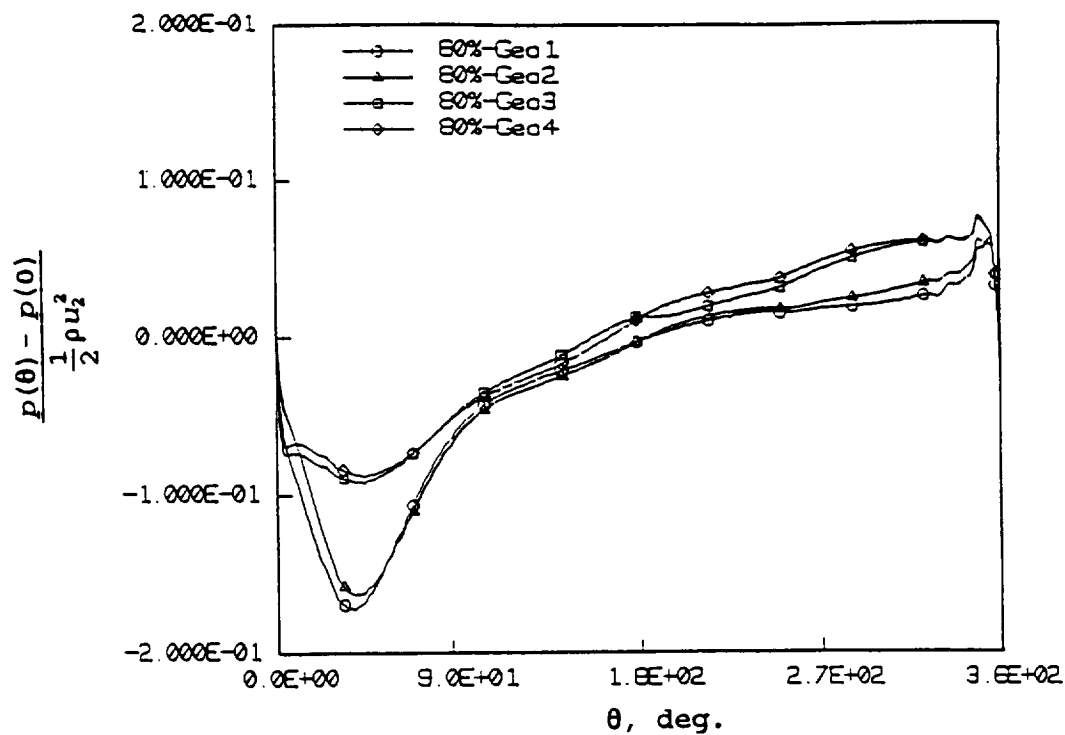
Fig. 49 Volute Pressure Profile $\phi/\phi_{design} = .8$
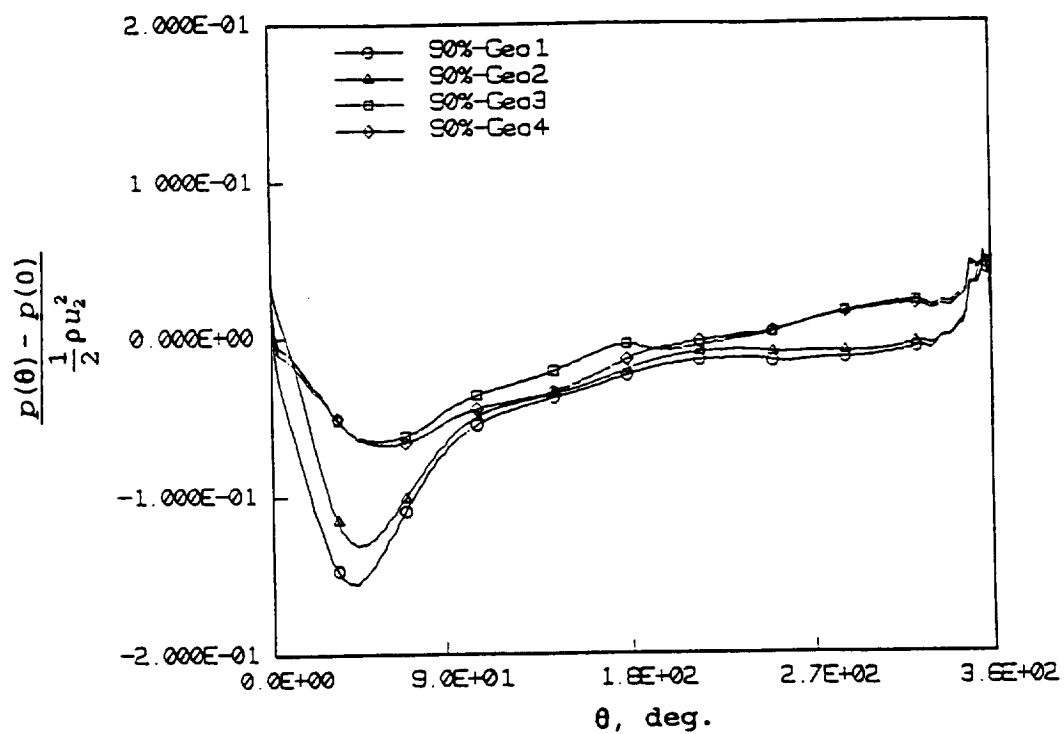
Fig. 50 Volute Pressure Profile, $\phi/\phi_{design} = .9$
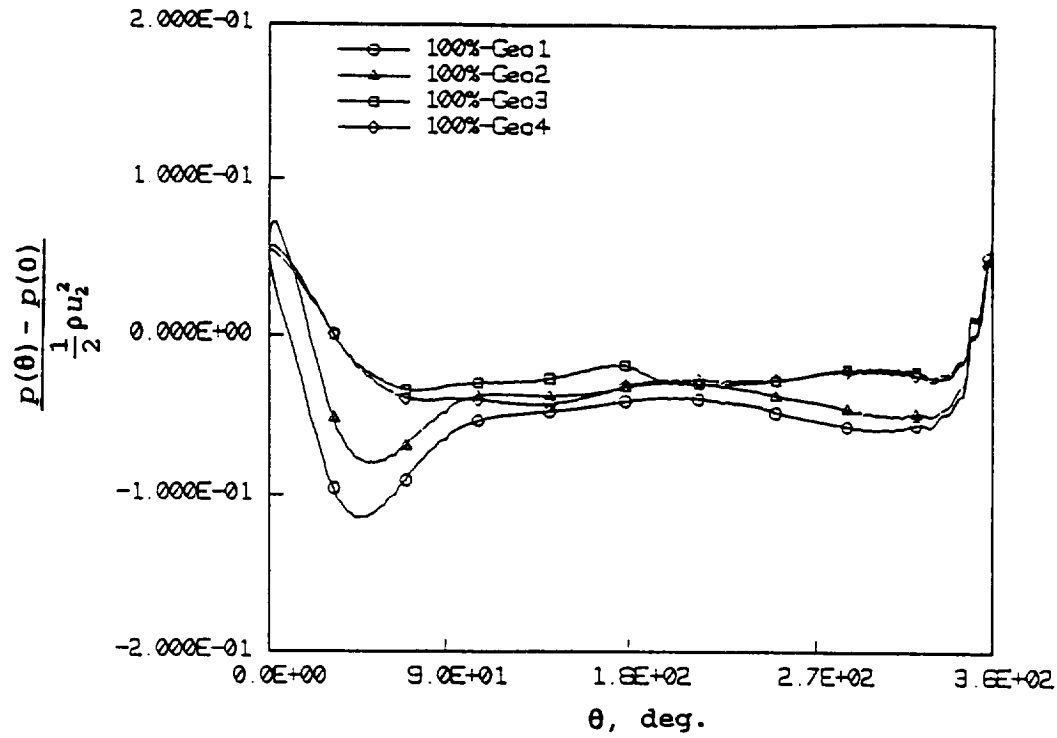
Fig. 51 Volute Pressure Profile $\phi/\phi_{design} = 1.0$
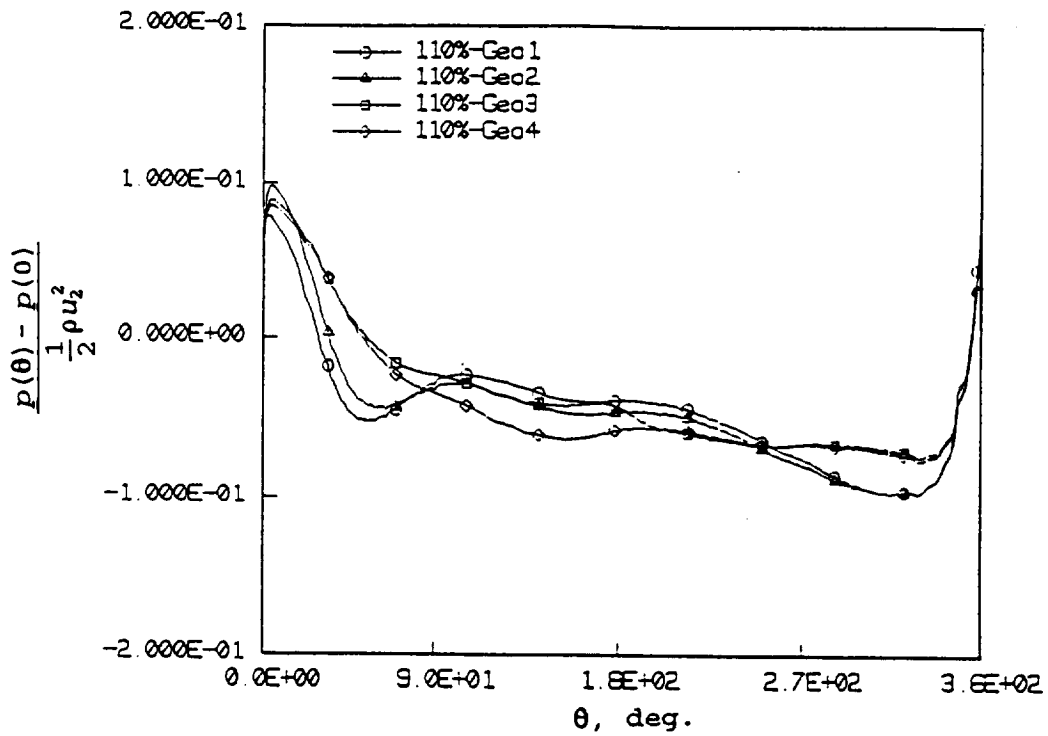
Fig. 52 Volute Pressure Profile, $\phi/\phi_{design} = 1.1$

pressure profile, $\dfrac{p(\theta) - p(0)}{.5\ \rho u_2^2}$, for the four geometric cases. For the last two cases with the

Archimedian spiral, the drop in pressure after the tongue was flattened. The calculated force components are shown in Fig. 53, with the force magnitude in Fig. 54. Except for $\phi/\phi_{design} = 1.1$, the geometry changes tried shifted the $F_x(\theta)$ and $F_y(\theta)$ curves but did not noticeably affect their slope. The tongue modification had the greatest effect on $\phi/\phi_{design} = 1.1$.

The calculations shown in Fig. 54 were used to select the test volute design described in the next section of this report. However, since the simulated radial forces indicated such a strong dependence on volute geometry, another case was analyzed. The grid used for the case labeled: "baseline: spline" for Volute A was observed to have an unrealistic convergence immediately after the tongue. A new Volute A grid was constructed from the $F\{\theta\}$ cross-sections using piece-wise continuous circular arcs matched at the locations of the metal guides in the form upon which the fiberglass shell was cast. The results of this case is shown as "baseline: 3 point arc" in Fig. 55. The computed forces resulting from this geometry change are obviously of the order as those caused by the other shape changes studied. The other geometries studied did not exhibit the unrealistic convergence noted in the baseline case. However, such sensitivity suggests that the carefully machined metal volutes would be more susceptible to accurate CFD simulation.

4.2 Selection of the Test Volute

Although more parametric cases would have been valuable, the "arch spiral 186 ± 10 flat 0.5" was chosen as the verification case. A somewhat wider broadened minimum region in the force versus flow coefficient was indicated in Fig. 54, although the minimum was slightly higher (when compared to Volute A). A design drawing of this volute is shown in Fig. 56. The volute was manufactured and supplied to Caltech for testing.

The original plan was to manufacture the volute with fiberglass using a similar procedure to that used to manufacture Volute A. However, subsequent investigation indicated that the test volute could be made more accurately and for less cost by machining it from aluminum.
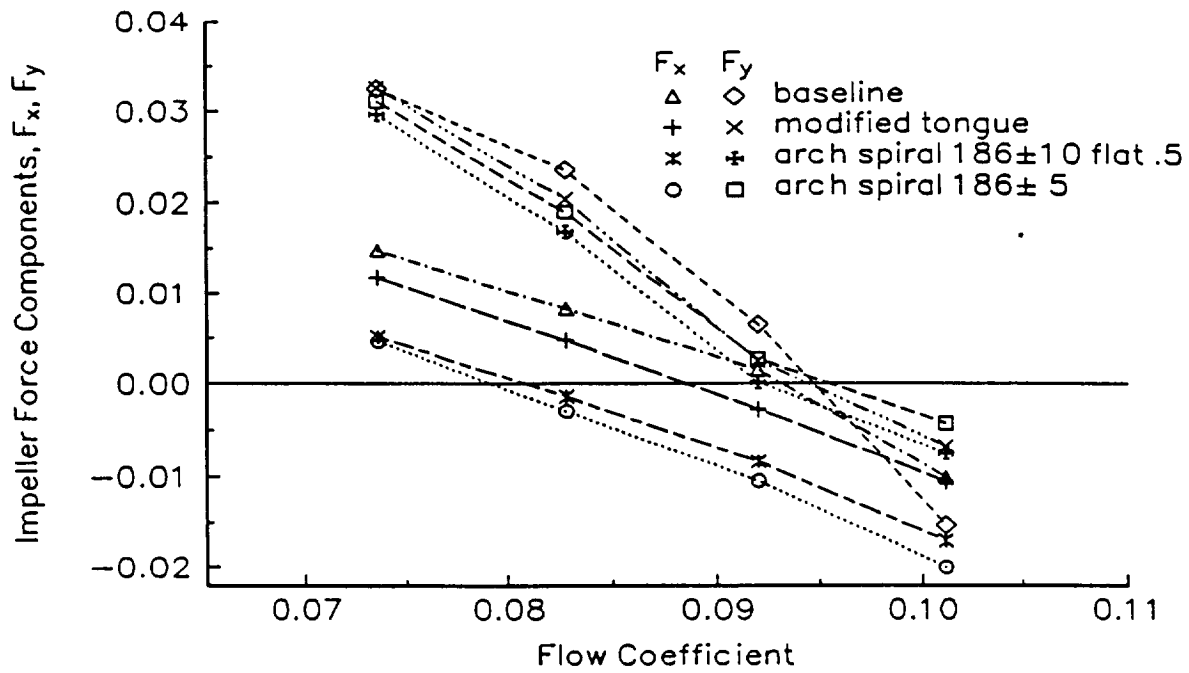
Fig. 53 Force Components as a Function of Flow Coefficient
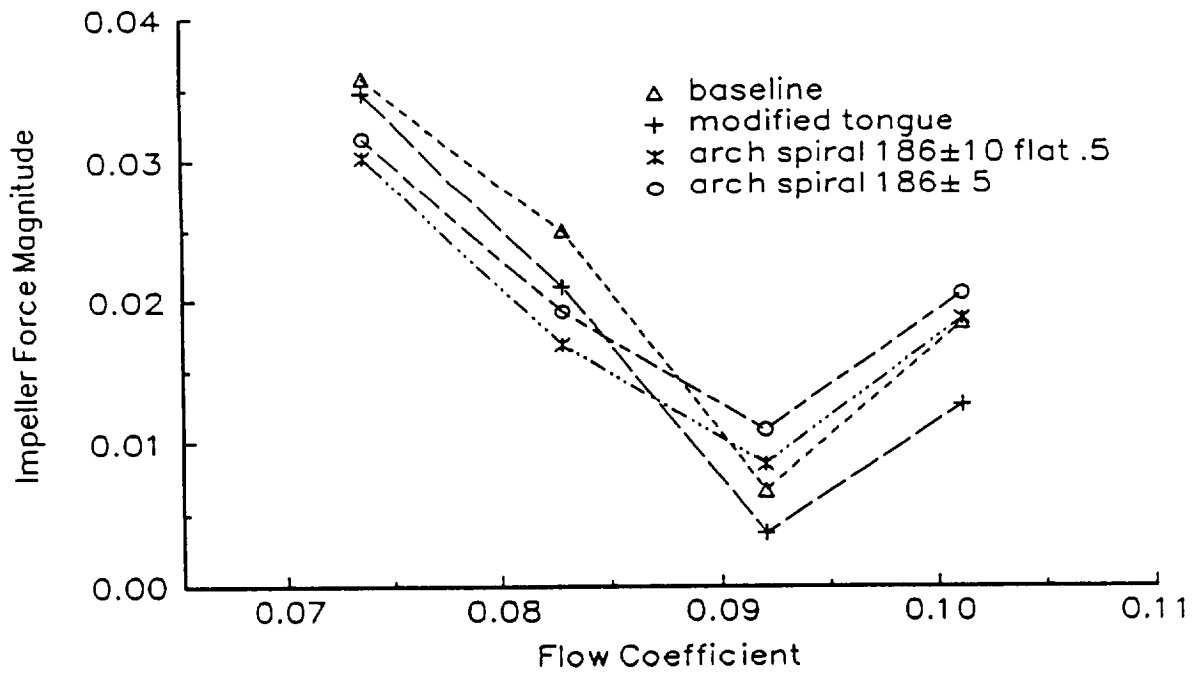
Fig. 54 Force Magnitude as a Function of Flow Coefficient
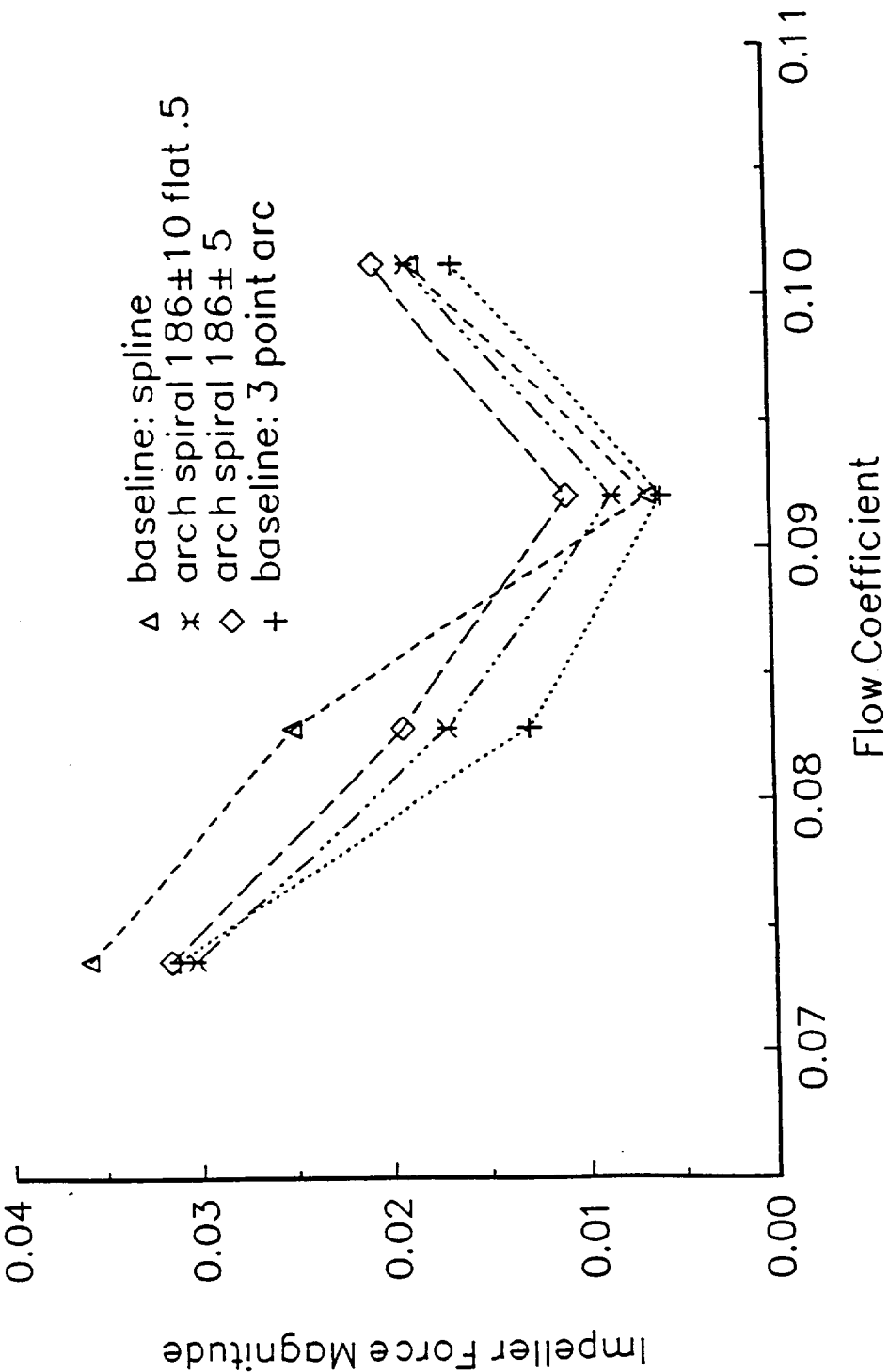
Fig. 55 Configuration Studies with Volute A

Fig. 56a Test Volute Configuration

Fig. 56b Test Volute Configuration
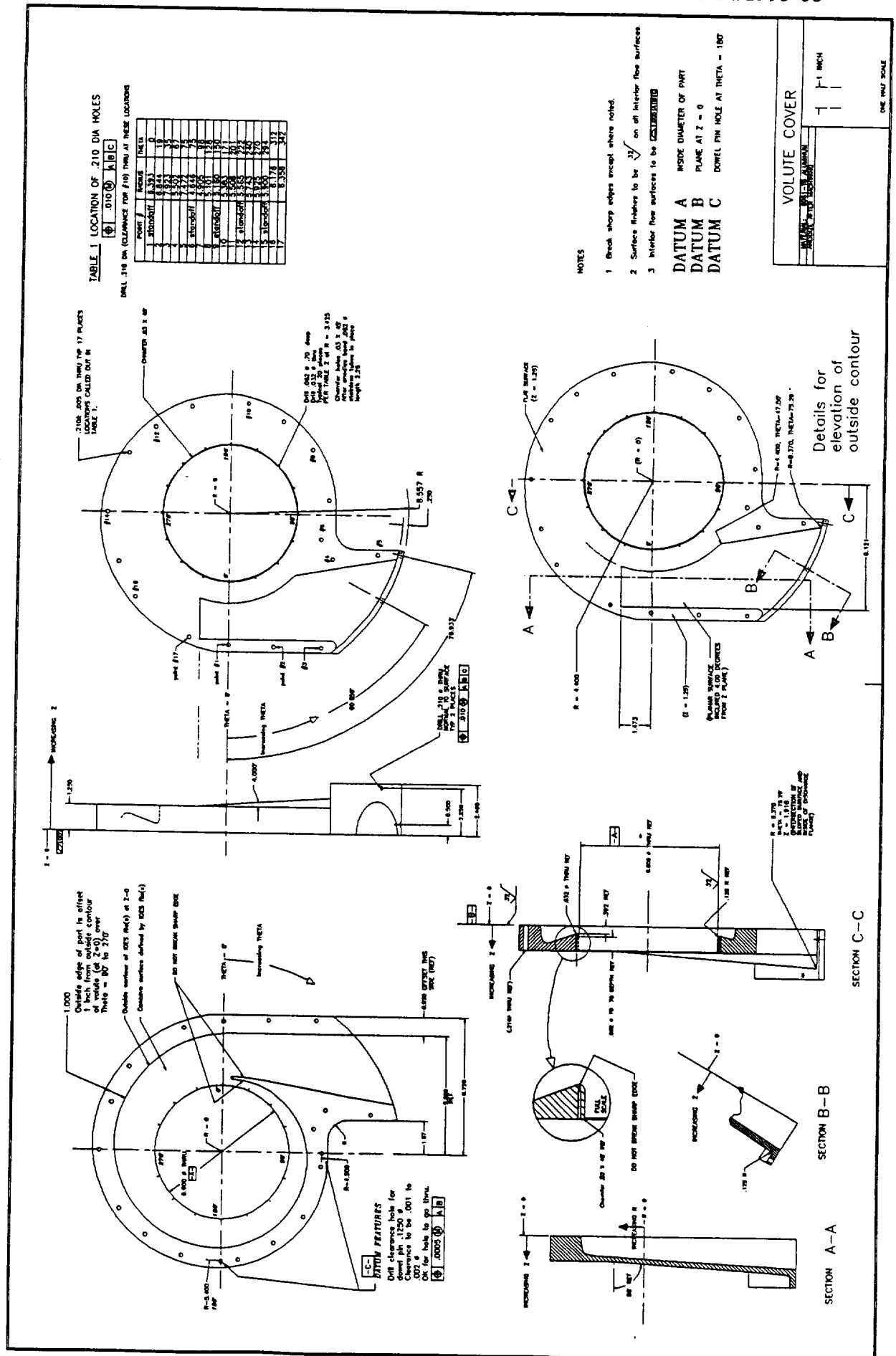
The use of a computer controlled milling machine was required to produce the volute. Such a machining operation was accomplished by specifying the geometry in an IGES formatted file.

Obtaining an IGES file involves the transformation of the volute surface from one form to another. The volute grid generator writes the grid out as a plot3d file, a set of discrete points. The procedure used is to read the plot3d file, extract the surfaces, convert the discrete point surface to a NURBS (Non-Uniform Rational B-Spline) surface, then write the NURBS surface in an IGES file format. The discrete points in the plot3d file controls what the surface in the IGES file actually describes. By obtaining an IGES file with a coarse grid, the created NURBS surfaces can be compared with the intended volute through a fine grid. The grid generator was brought to NASA/MSFC, where codes supplied by Mississippi State University were used to provide the NURBS surfaces and the IGES files. These files were supplied to a machinist and the test volute was fabricated.

5.0 EXPERIMENTAL EVALUATION OF TEST VOLUTE

The test volute was evaluated in the Rotor Force Test Facility (RFTF) at Caltech. The results of these tests are attached as Appendix B.

Figures 57 and 58 show a comparison of the measured and predicted radial forces on the test volute. The accuracy of the simulation is quite good near the design point. At extremely high and low flow coefficients, the trends are correct, but the accuracy is somewhat less. Leakages and other factors not included in the analysis are probably the cause of the differences observed. The CFD codes used for the design of the test volute are adequately verified by the experimental measurements. The small geometric differences between the test volute and Volute A indicate that the CFD analysis is sufficiently sensitive to evaluate design modifications. Furthermore the verification suggest that good dimensional control must be exercised on experimentally tested volutes to preclude obscuring important design features.

Figure 59 shows a comparison of the measured and predicted radial pressure distribution around the test volute. The pressure coefficient is defined as:

$$c_p = (p - p_{ref})/0.5\rho\, u_2^2$$

u_2 is the impeller exit velocity. p_{ref} in the FDNS simulation and in Appendix B are not the same. This difference changes the magnitude of the pressure coefficient; therefore, the measured pressure profiles were rescaled for comparison in Fig. 59. The obvious differences in pressure for the two sides of the volute are due to the use of an assumed constant impeller exit velocity from the hub to the shroud (which results from using the Adkins/Brennen impeller model) and to leakage effects. The pressure profile fits are reasonable and apparently do not effect the good force predictions shown in Figs. 57 and 58.
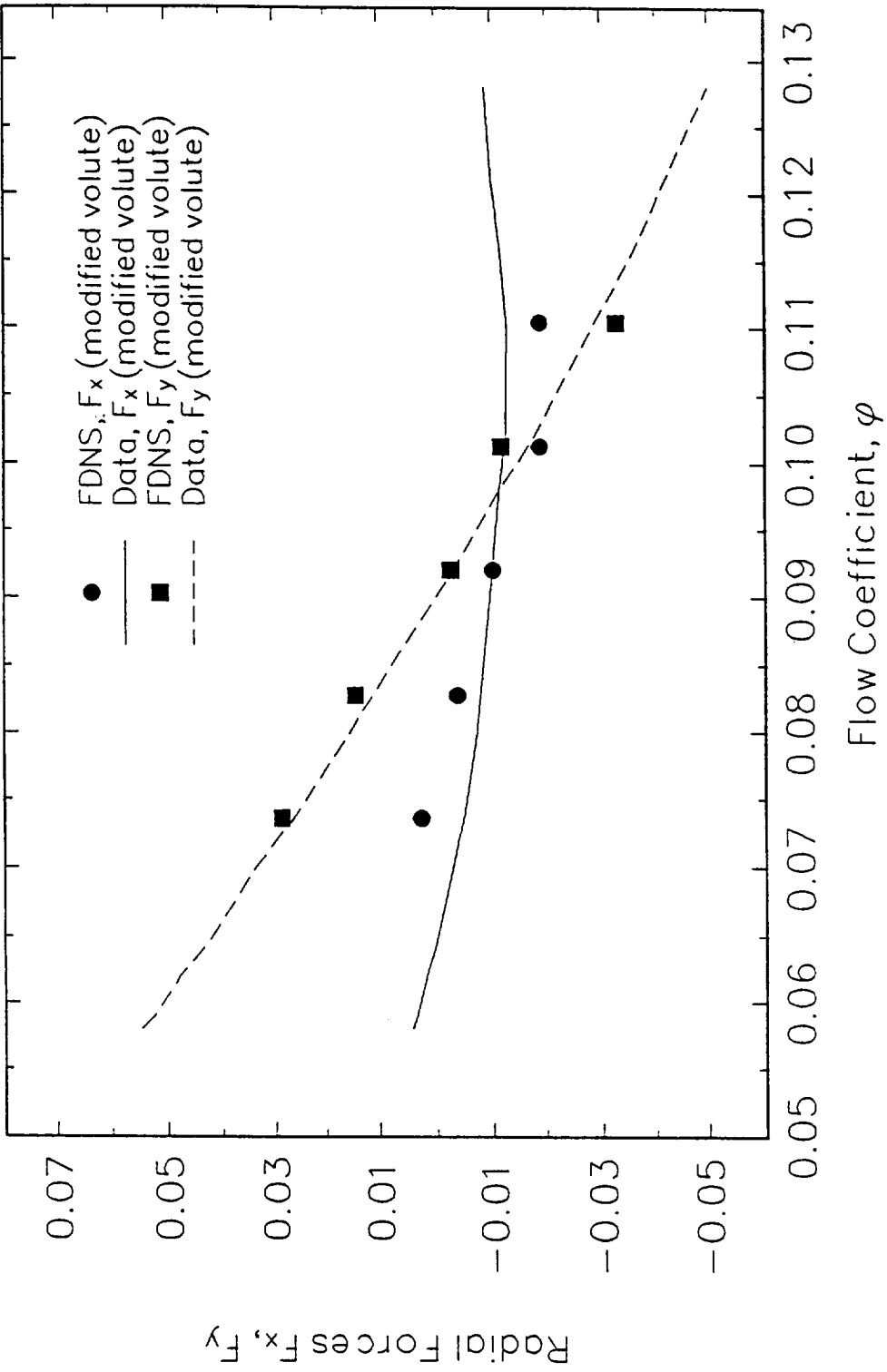
Fig. 57 Radial Force Components for the Test Volute
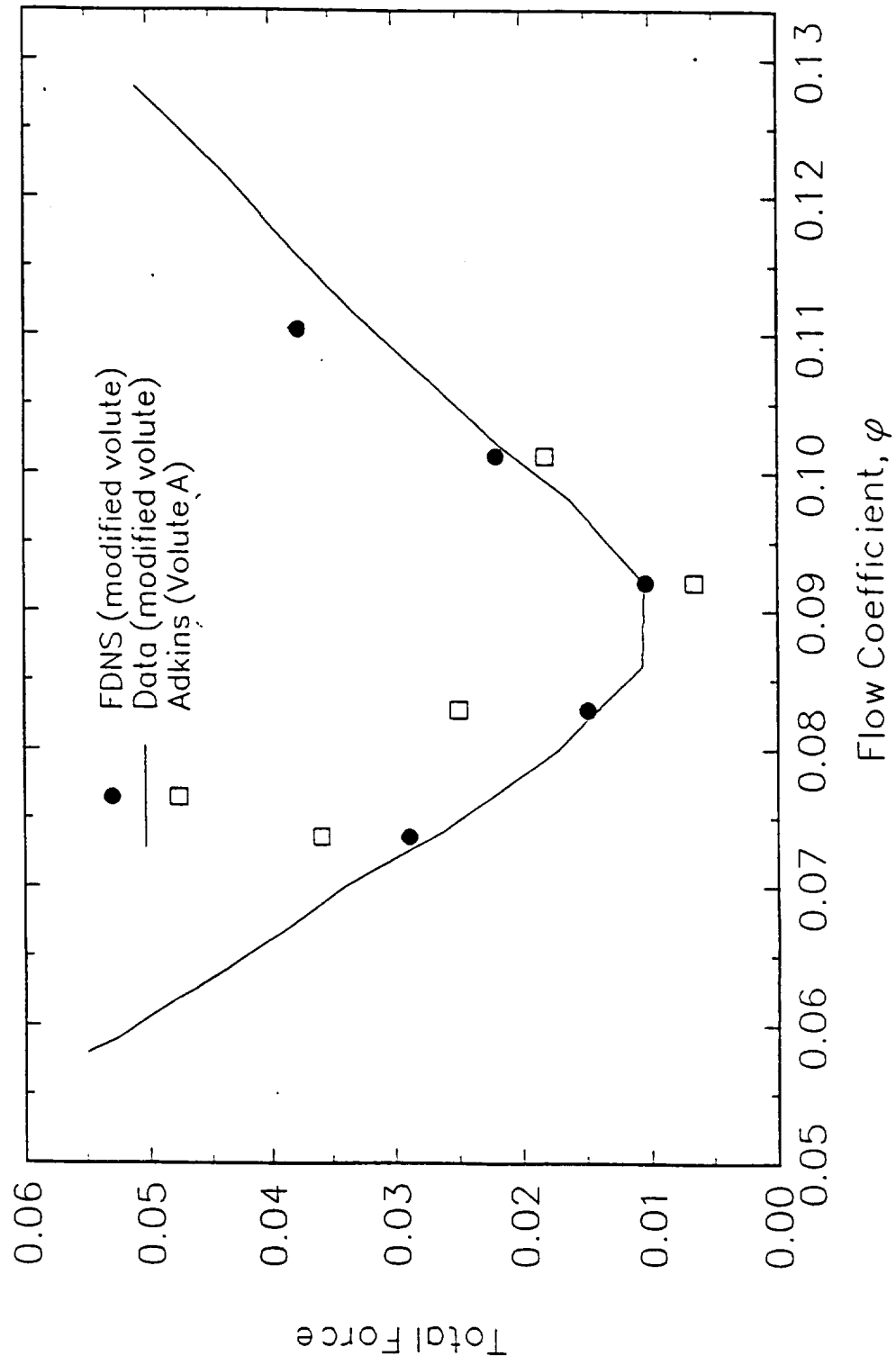
Fig. 58 Magnitude of the Radial Forces for the Test Volute
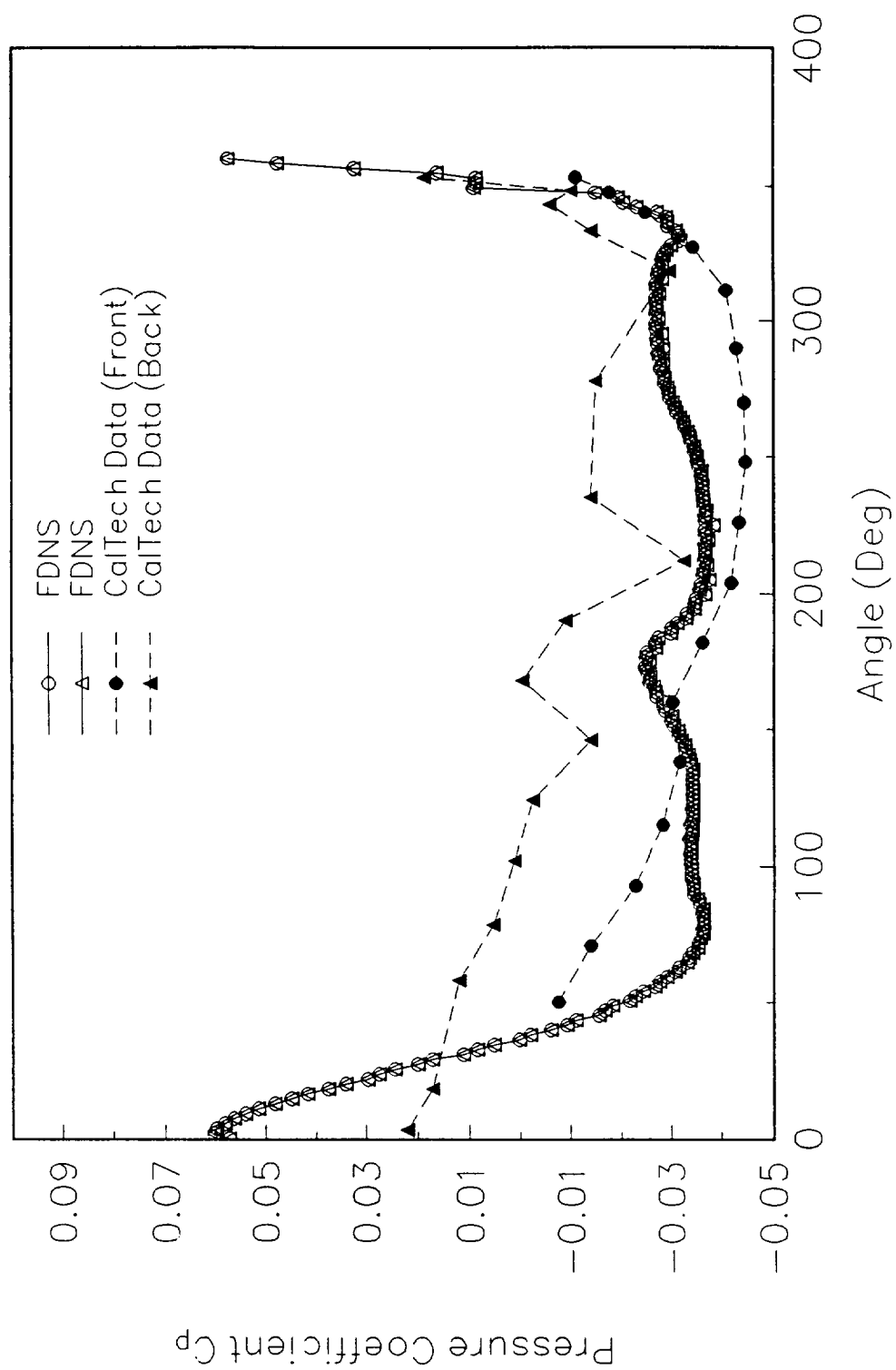
Fig. 59 Pressure Distribution in Test Volute at $\phi = 0.092$

6.0 CONCLUSIONS

The following conclusions are drawn from this investigation:

(1)   The volute grid generator is useful for investigating volute configurations.

(2)   Coupled impeller/volute CFD solutions are feasible, but they require excessive computation time to provide parametric volute configuration studies.

(3)   Using Adkins/Brennen's β-equation for impeller/volute coupling with a CFD volute simulation provides an accurate and practical model for optimizing volute configurations. The simulations are very sensitive to the volute geometry specified. The parameter γ in the Adkins/Brennen impeller model should be evaluated with at least one fully coupled impeller/volute CFD simulation for each major impeller/volute configuration change considered.

(4)   The impeller/volute model described in (3) was verified by experimental measurements for a single configuration. The agreement between the simulation and experiment is excellent near the design flow coefficient, and becomes somewhat less accurate away from the design point.

(5)   The design methodology can be used to minimize, or set to a prescribed, value, the radial forces on a pump by controlling volute geometry.

7.0 RECOMMENDATIONS

To obtain the maximum benefit from this pump model code, the following recommendations are offered:

(1)   The grid generator should be extended to provide an option for creating volute surfaces in an IGES format.

(2)   The pump model should be used in its present form to parametrically study impeller/volute interactions on radial forces over a wide range of volute configurations.

(3)   The pump model should be extended to treat vaned volutes, vaned diffusers, and cross-over ducts for multi-stage pumps. Parametric configuration studies should be made with this model. Note that the effects of axial velocity gradients at the trailing edge of the impeller vanes and of rotor/stator interaction are neglected in this pump model.

(4)   The pump model should be extended to treat impeller/volute rotor dynamic interactions by direct application of the Adkins/Brennen impeller whirl model to CFD volute simulations. This extension should include applications to fluid bearings.

REFERENCES

Adkins, D.R., (1986). "Analyses of Hydrodynamic Forces on Centrifugal Pump Impellers," Ph.D. thesis, Division of Engineering and Applied Science, California Institute of Technology, Pasadena, CA., 1986.

Adkins, D.R. and Brennen, C.E. (1988). "Analyses of Hydrodynamic Radial Forces on Centrifugal Pump Impellers". ASME J. Fluids Eng., 110. No. 1, 20-28.

Agostinelli, A., Nobles, D. and Mockridge, C.R. (1960). "An Experimental Investigation of Radial Thrust in Centrifugal Pumps". ASME J. Eng. for Power 82, 120-126.

Brennen, C.E., (1994). Hydrodynamics of Pumps, Concepts ETI, Inc., Norwich, Vt.

Chamieh, D.S. (1983). "Forces on a Whirling Centrifugal Pump - Impeller," Ph.D. Thesis, Division of Engineering and Applied Science, California Institute of California, Pasadena, CA.

Chen, Y.S., (1988). "3-D Stator-Rotor Interaction of the SSME," AIAA Paper 88-3095.

Chen, Y.S., (1989). "Compressible and Incompressible Flow Computations with a Pressure Based Method," AIAA Paper 89-0286.

Chen, Y.S., (1993). FDNS A General Purpose CFD Code User's Guide, Version 3.0.

Jery, B., (1987). "Experimental Study of Unsteady Hydrodynamic Force Matrices on Whirling Centrifugal Pump Impellers," Ph.D. thesis, Division of Engineering and Applied Science, California Institute of Technology, Pasadena, CA.

APPENDIX A

THE ADKINS/BRENNEN PUMP MODEL

A.1 The Adkins/Brennen Impeller/Volute Interaction Model

To analytically describe the interaction of impeller/volute flows and forces, Adkins and Brennen (1988) constructed a flow model for the impeller and for the volute which was matched by iteration at the impeller exit and the volute inlet. This model accounts for whirl, but in this investigation only impeller centered flows were considered. The impeller flow was modeled with an unsteady form of the Bernoulli equation. This flow was assumed to be 2-dimensional, and the whirl speed was assumed constant. The flow was also assumed to follow a spiral path through the impeller at a fixed angle relative to the impeller. This angle was a function of the flow rate and the head rise, as required to satisfy an experimentally determined pump curve. Initial conditions for the impeller flow were no swirl and circumferentially constant total head. The volute flow was described with a continuity equation, a moment of momentum equation, and a radial momentum equation. The velocity profile in the volute was assumed to be flat across a cross-section and vary circumferentially around the spiral. The resulting model consisted of nine ordinary differential equations which were solved by iteration until pressure and flow conditions at the interface between the impeller discharge and the volute inlet were matched. Application of this flow model to the Volute A/Impeller X pump is shown in Fig. A-1, from Adkins (1986). The model does not closely match the test data, but the proper trends are predicted.

The Adkins and Brennen pump model was encoded from the listing in Adkins (1986) dissertation for use as a stand-alone pump model and as a module to provide boundary conditions for a CFD calculation the volute flow. The Adkins/Brennen impeller submodel describes the flow between the inlet and discharge of the impeller with a simplified Bernoulli equation:

$$P_i/\rho + 0.5(v^2 - \Omega^2 r''^2) + \int_{s''} \frac{\partial v}{\partial t} ds'' - \omega^2 \epsilon \int_{s''} \cos\{\omega t - \Omega t - \theta''\} dr''$$
$$- \omega^2 \epsilon \int_{s''} \sin\{\omega t - \Omega t - \theta''\} r'' d\theta'' = F\{t\} \tag{A-1}$$
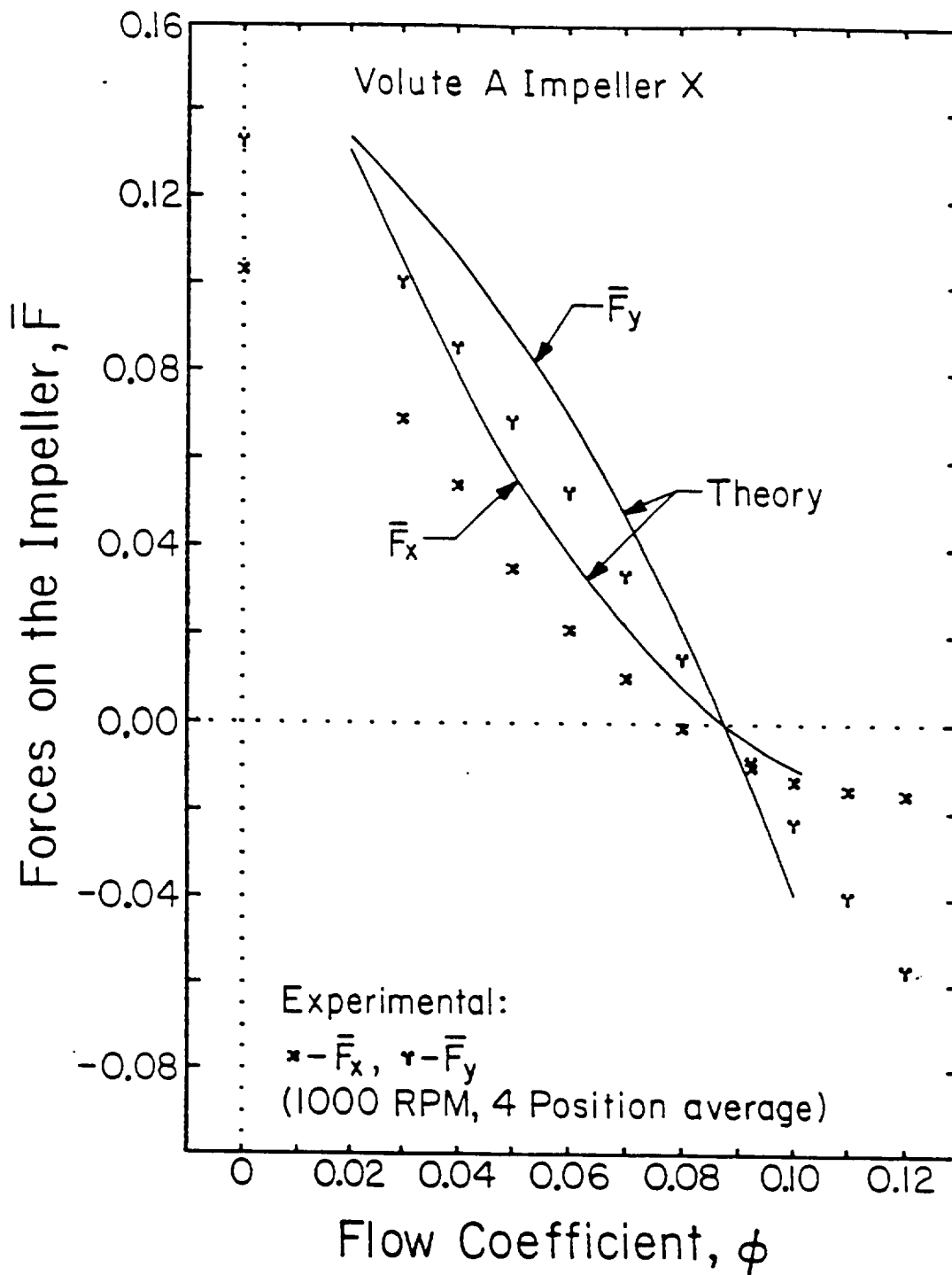
Fig. A-1   Radial forces on Impeller X in Volute A, theoretically calculated over a wide range of flow coefficients, and compared to experimental measurements, from Adkins (1986).

The geometric variables used are defined in Fig. A-2. The flow in the impeller is assumed to follow a spiral path with inclination angle γ which is fixed relative to the impeller. For a given flowrate and head rise, the spiral path is described by:

$$\theta_2{}'' = \theta'' + \tan \gamma \, \ln\{r''/R_2\} \tag{A-2}$$

The inclination angle is found by equating the theoretical and experimental head/flowrate characteristics (ψ_{exp}, in dimensionless form):

$$\psi_{exp} = 0.5[D_p\{2\pi\} + C_vV^2\{2\pi\}] \tag{}$$

where D_p is the volute pressure coefficient and V is the non-dimensionalized velocity in the volute. D_p and V are evaluated with a centered impeller, and C_v is defined in terms of the moments of the volute cross-sectional area.

To account for flow asymmetry, a circumferential perturbation, β, is imposed on the mean impeller flow, which is related to the relative velocity in the impeller, v, as follows.

$$v = [\phi\Omega R_2{}^2/r'']\beta\{\theta'', \, r'',\Omega t,\omega t,\epsilon\}\sec\{\gamma\} \tag{A-3}$$

For small eccentric whirl orbits, ϵ, β may be linearized

$$\beta\{\theta'',r'',\Omega t,\omega t,\epsilon\}=\beta_o\{\theta_2\}+\epsilon^*[\beta_c\{\theta_2\}\cos\omega t+\beta_s\{\theta_2\}\sin\omega t] \tag{A-4}$$
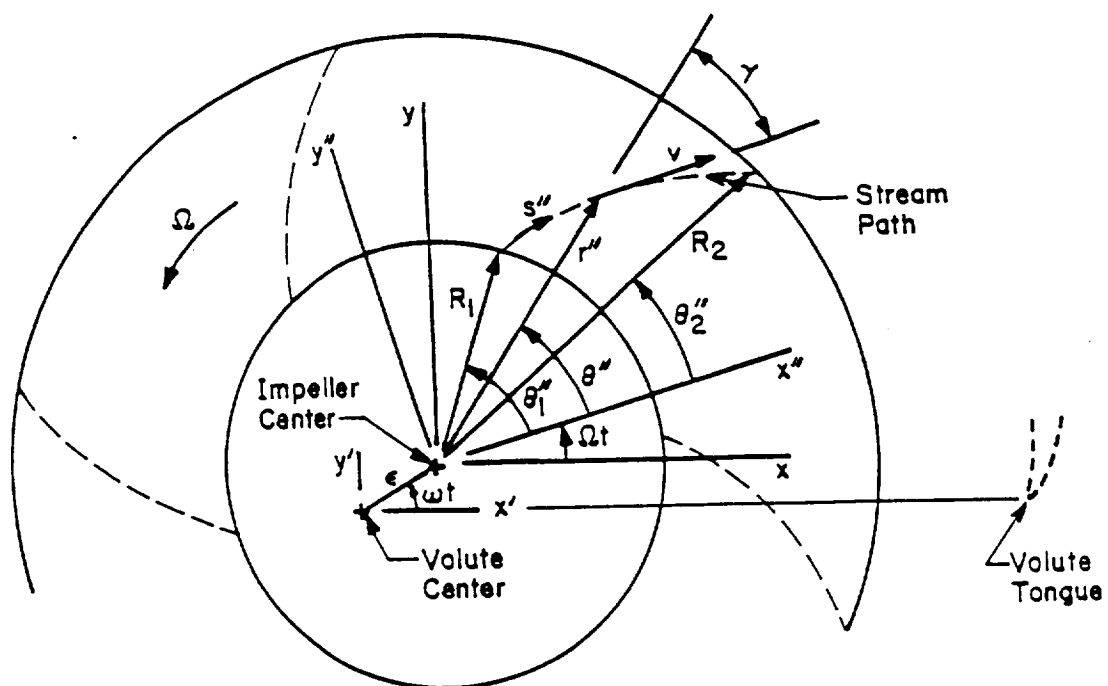
Fig. A-2. Geometry of a Centrifugal Pump Impeller, Adkins (1986).

65

By combining equations 1, 3, and 4, and by assuming no inlet swirl and no circumferential total

pressure variation, the dimensionless inlet pressure may be written

$$P_i^*\{R_1,\theta_1\} = h_1^* - \phi R\beta_o\{\theta_2\}[\phi R\beta_o\{\theta_2\} + 2\epsilon^*(\omega/\Omega)\sin\{\theta_1-\omega t\}]$$

$$- 2\epsilon^*\phi^2 R^2\beta_o\{\theta_2\}[\beta_c\{\theta_2\}\cos\omega t + \beta_s\{\theta_2\}\sin\omega t] \qquad (A-5)$$

By combining equations A-3, A-4, and A-5 and neglecting higher order terms,

Bernoulli's equation may be separated into harmonics with steady, $\epsilon \cos \omega t$, and $\epsilon \sin \omega t$

dependency. The steady term becomes

$$\phi \sec^2\gamma[2 \ln\{R\} (d\beta_o/d\theta_2) + \phi \beta_o^2] + D_p - 1 = 0 \qquad (A-6)$$

The sine and cosine harmonics will not be given here since they deal only with unsteady forces;

they are given in Adkins and Brennen (1988), hence $\beta_o = \beta$.

The Adkins/Brennen impeller/volute interaction analysis was coded as a stand-alone code,

and Eq. A6 was used to provide inlet boundary conditions for flow into the volute. The

Adkins/Brennen analysis models the volute flow and solves the coupled set of equations for β,

D_p, V, and γ by iteration for a measured value of the head rise across the pump.

A.2 Caltech Pump Test Data

Reports and records at Caltech were reviewed to obtain engineering drawings of the Rotor Force Test Facility and of the various impeller/volute configurations which have been studied. Most of the impeller-volute combinations were tested with Impeller X. Table A-1 describes these volutes. The circumferential increase of the cross-sectional area is shown in Fig. A-3. The magnitude of the side force on Impeller X for these volutes is shown in Fig. A-4, with the vaneless volutes in part (a) and the vaned diffusers in part (b). These measurements were reported by Jery (1987).

Two volutes were selected for modeling. The first one studied was a vaneless volute, for which the grid generation was simpler. Volute A was selected since it was designed to match Impeller X. Also, wall pressure measurements were taken at the volute inlet with the impeller displaced from the volute center in four directions (stiffness measurement). Volute D geometry was used as the basis of a 2-dimensional CFD simulation. No validation data exists for Volute D other than total force measurements.

A listing of Adkins' pump model, WHIRL2, was obtained from Adkins (1986), but the code was not available. The listed code was converted from Basic to Fortran and has been checked against Adkins' published solutions. Drawings of Impeller X and Volute A used in the comparison with Adkins' results were presented in Figs. 5 and 4, respectively. Software was written to generate the volute cross-section integrals required as input by WHIRL2. The integrals were calculated using the cross-sections in Fig. 4; however, the fillet radius at the

67

Table A-1 Volutes Tested with Impeller X at Caltech's Rotor Force Test Facility Data taken from Jery (1987)					
VOLUTE NAME	VOLUTE TYPE	CROSS SECTION SHAPE	SPIRAL ANGLE	NUMBER OF VANES	VANE ANGLE
A	VOLUTE	TRAPEZOIDAL	4	0	-
B	VOLUTE	CIRCULAR	-	0	-
C	VOLUTE	TRAPEZOIDAL	4	0	-
C (D-O)	VANELESS DIFFUSER	TRAPEZOIDAL	4	0	-
E	VANED DIFFUSER	ELLIPTIC	5	17	18
F (D-6L)	VANED DIFFUSER	TRAPEZOIDAL	4	6 LONG	10
G (D-6S)	VANED DIFFUSER	TRAPEZOIDAL	4	6 SHORT	15
H (D-12S)	VANED DIFFUSER	TRAPEZOIDAL	4	12 SHORT	15
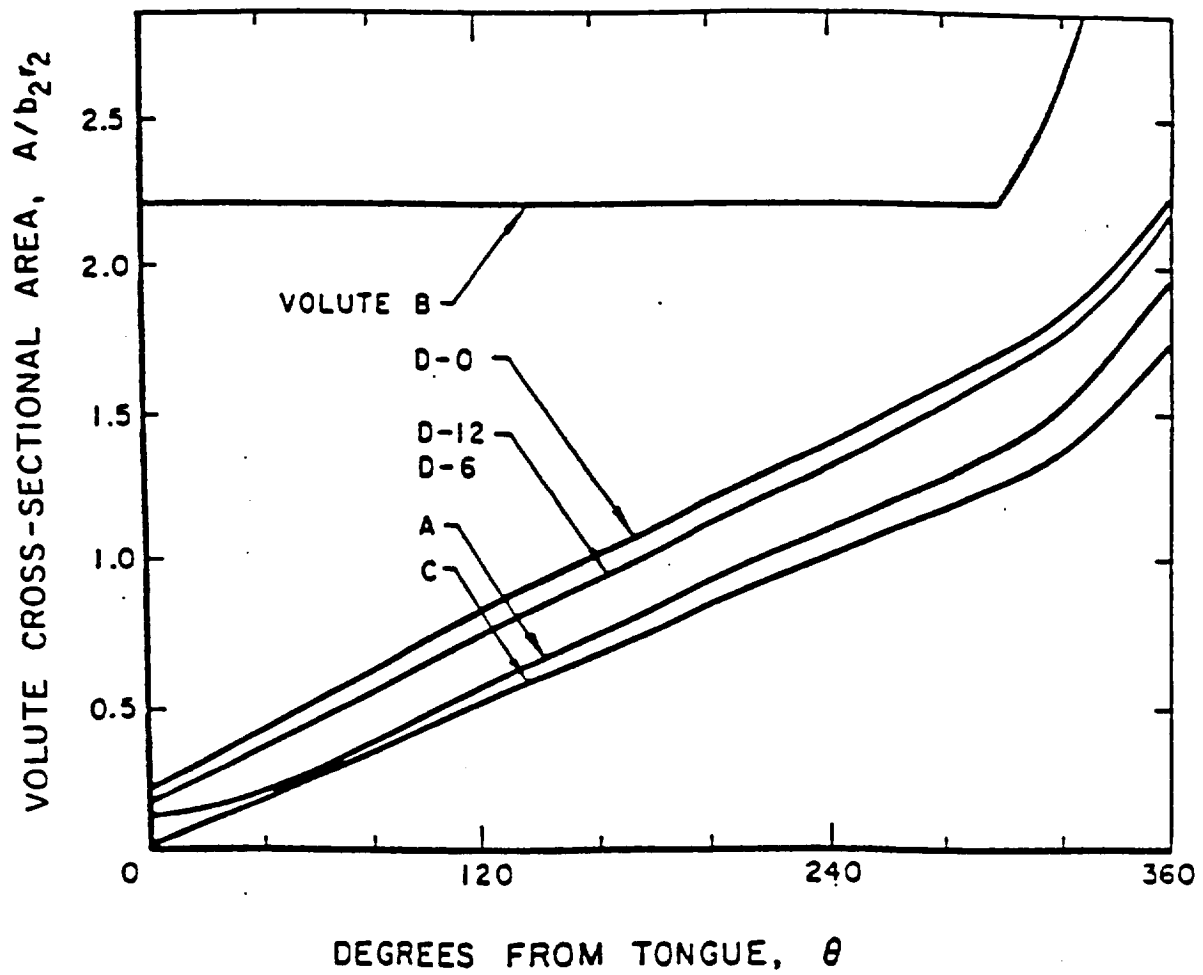
Fig. A-3 Volute Cross-Section Area for the Various Volutes Tested
from Jery (1987)
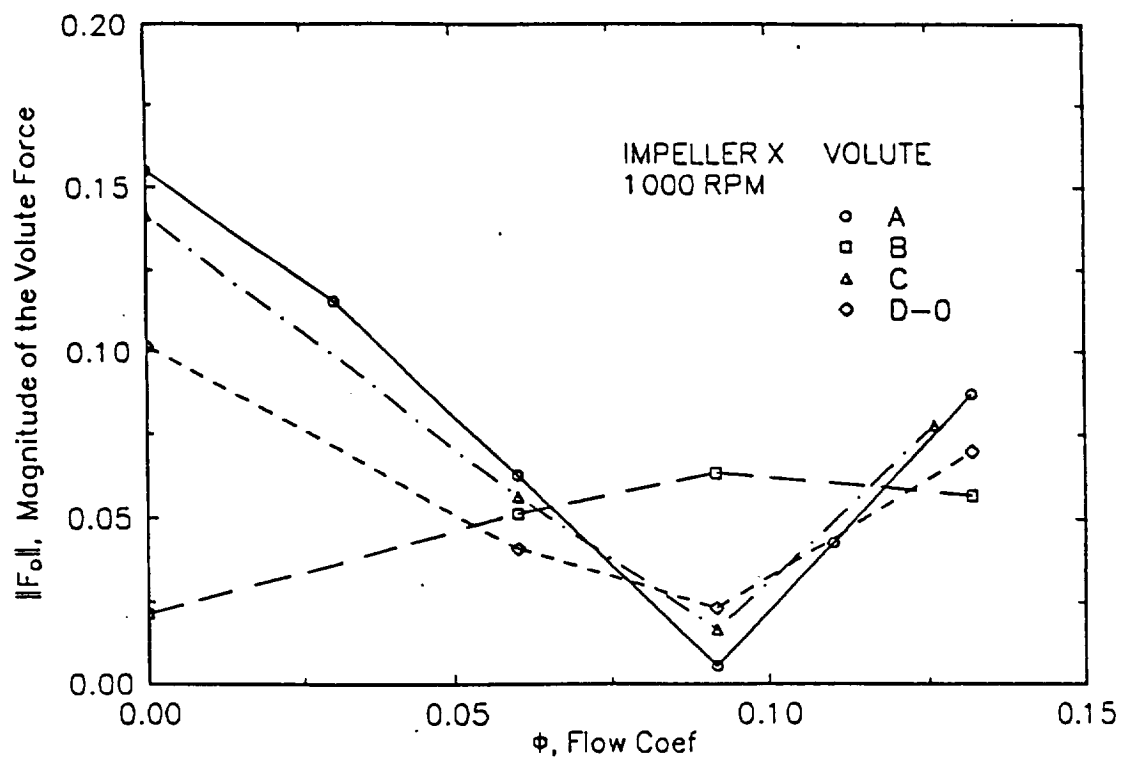
Fig. A-4a Magnitude of the Volute Force for Vaneless Volutes
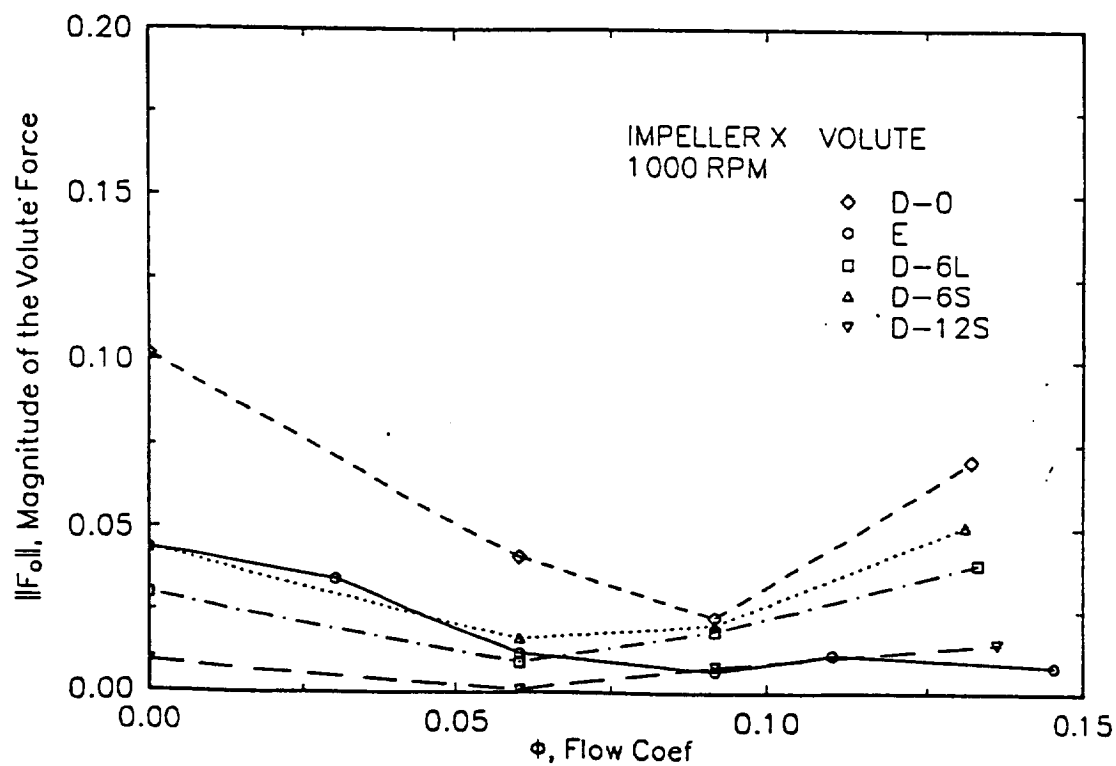
Fig. A-4b Magnitude of the Volute Force for Vaned Diffusers

70

volute inlet was ignored. Figs. A-5 through A-8 show plots providing a comparison between the current calculations and results taken from Adkins (1986). The input integrals are given in Figs. A-5 and A-6. These integrals were interpolated using quadratic and cubic splines for the Adkins and SECA calculations, respectively. The model results can be compared by examining the flow perturbation at the impeller discharge and the pressure distribution at the volute inlet for several flow coefficients as shown in Figs. A-7 and A-8 for Adkins and SECA, respectively. Notice that the Adkins/Brennen model predicts a static pressure discontinuity at the cutwater. The conversion and implementation of the Adkins/Brennen code was successful.

The Adkins/Brennen code to model the impeller-volute flow for an impeller whirling on a circular orbit within the volute was modified to eliminate interaction with the user during the calculation of the steady, impeller centered, solution. Instead of the user comparing the computed head rise with an experimental value, after having provided the impeller flow path angle as input, the program will now search for the appropriate flow angle for a specified head rise and tolerance.
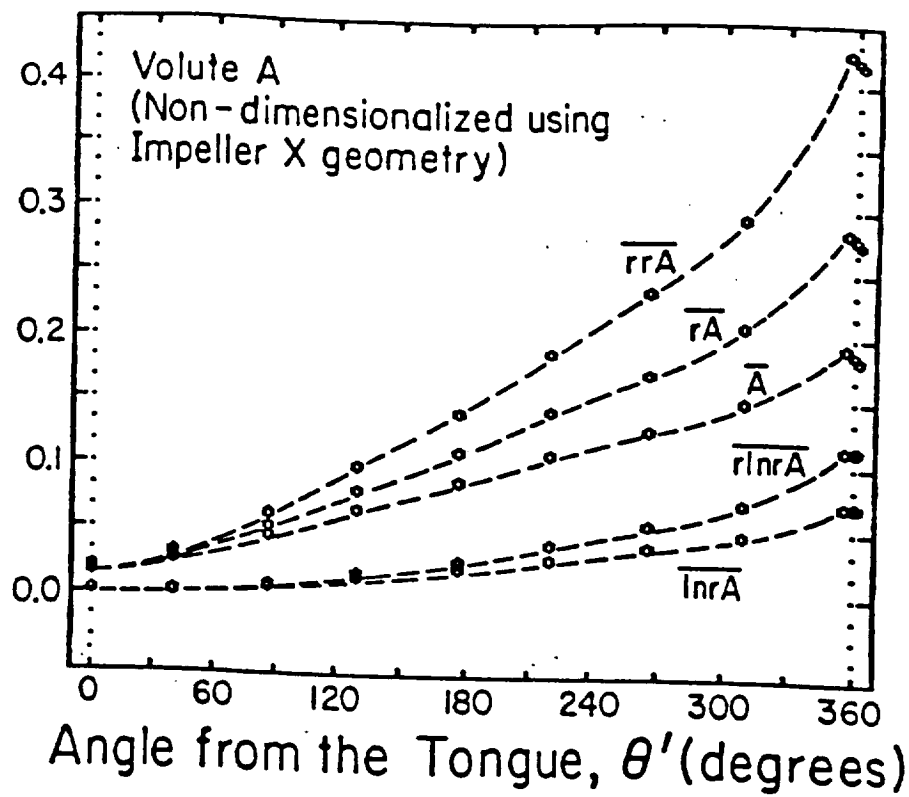
Fig. A-5 Moments of the Volute Cross Section, from Adkins (1986)
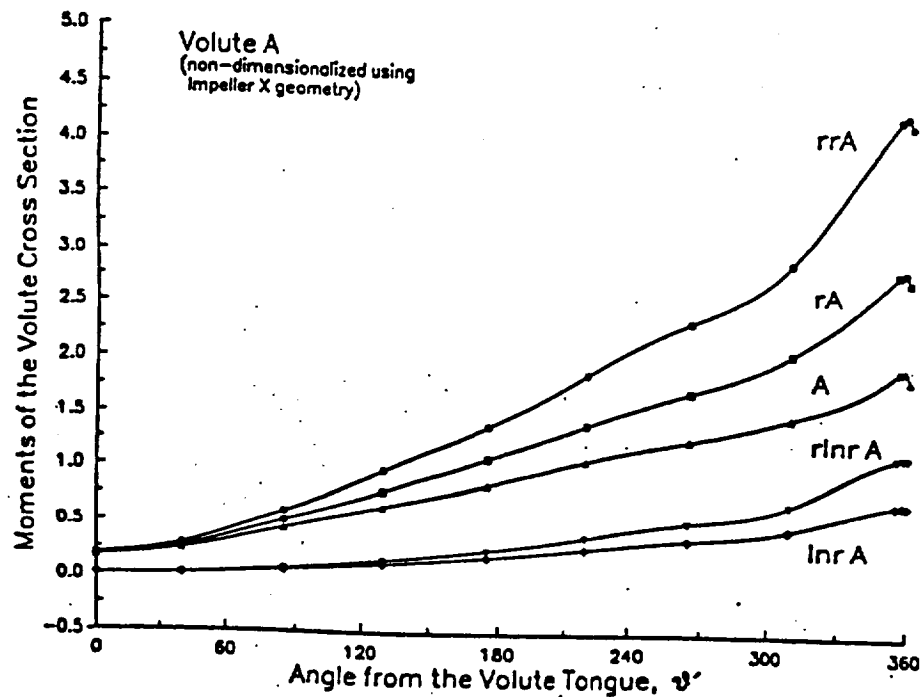
Fig. A-6 Calculated Moments of the Volute Cross Section

72
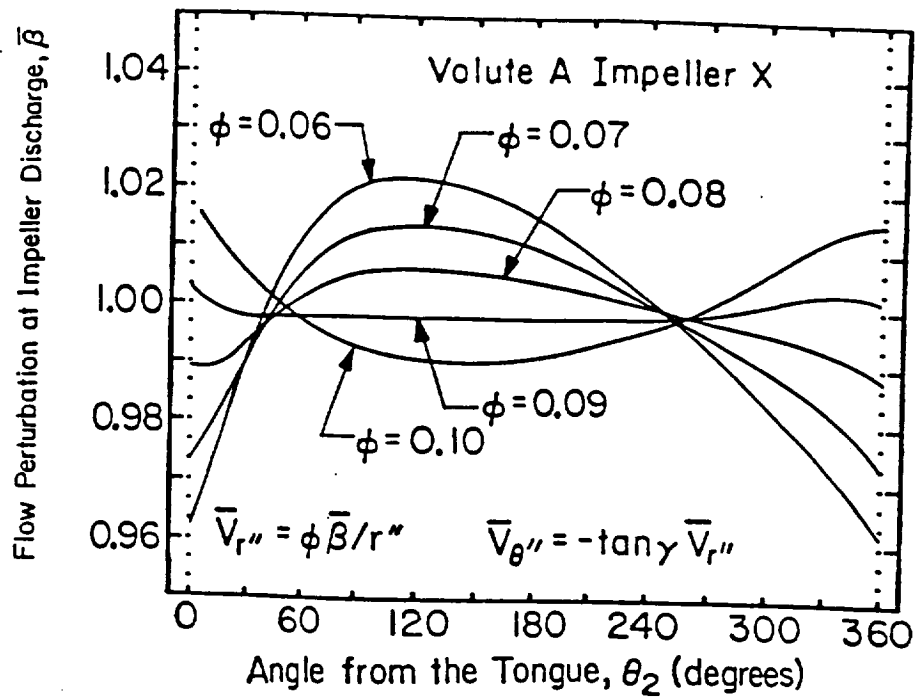
Fig. A-7a Flow Perturbation at Impeller Discharge, from Adkins (1986)
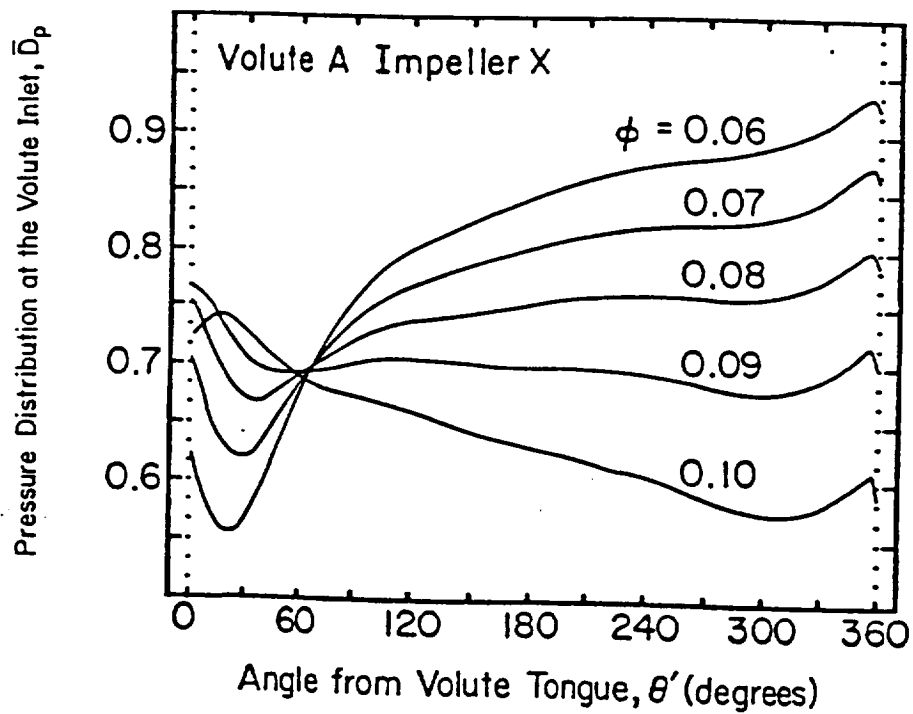
Fig. A-7b Pressure Distribution at the Volute Inlet, from Adkins (1986)

73
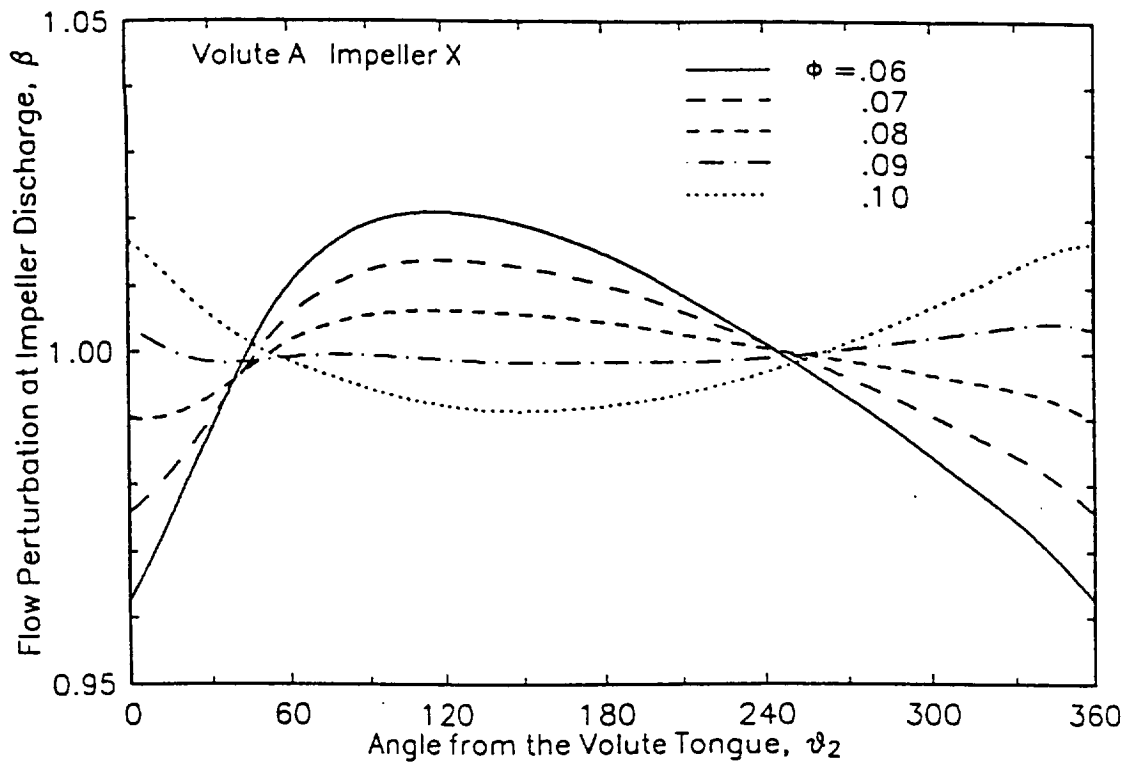
Fig. A-8a Calculated Flow Perturbation at Impeller Discharge
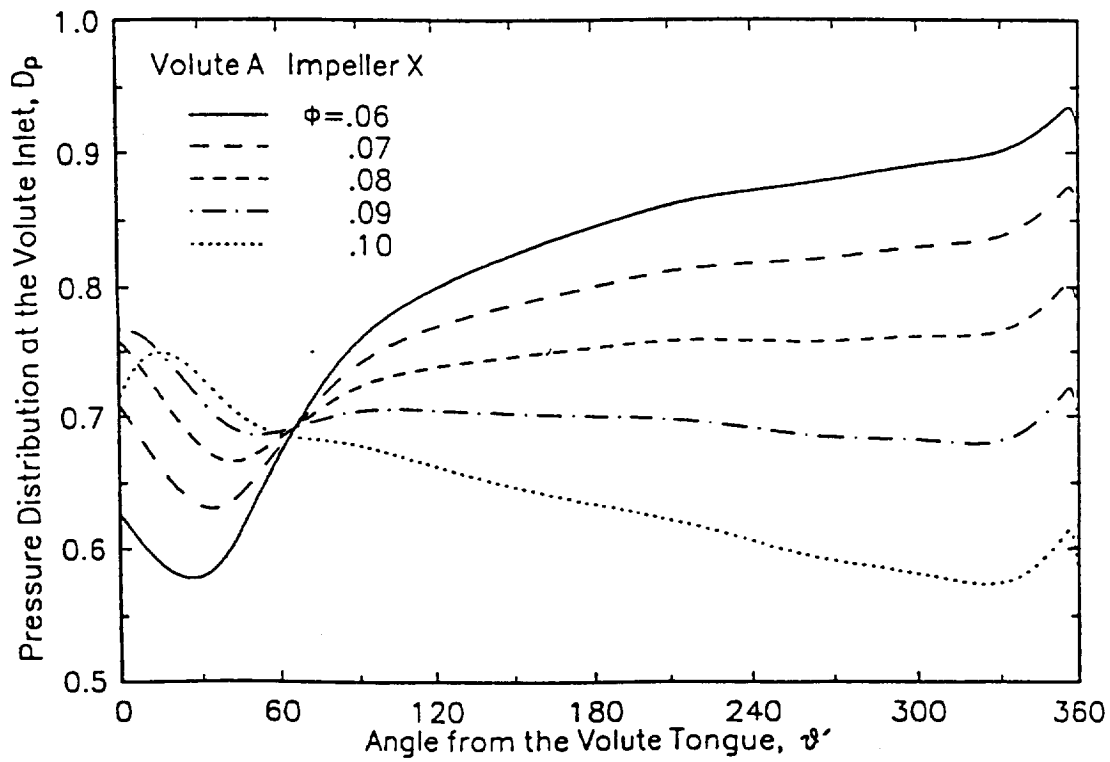
Fig. A-8b Calculated Pressure Distribution at the Volute Inlet

74

A.3 Instructions for Using The Adkins.for Code

A copy of the Adkins/Brennen code for the calculation of only the steady, impeller centered, flow was provided to NASA/MSFC. An Input Instructions Guide is given below. The I/O of the code was modified when it was implemented as a subroutine in the volute design program.

Impeller/Volute Model Geometry
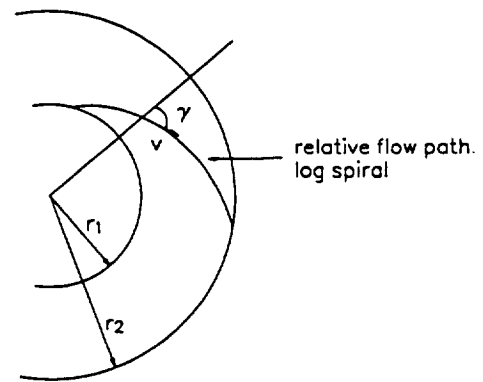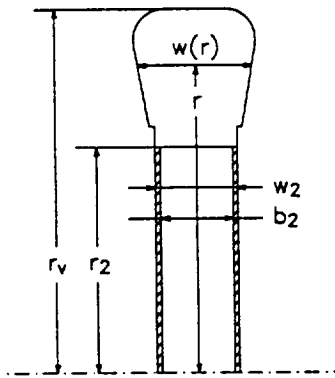
cross-section integrals

$$\bar{A}(\theta) = \frac{\int_{r_2}^{r_v} w(r)\,dr}{b_2 r_2}$$

$$\overline{rA}(\theta) = \frac{\int_{r_2}^{r_v} r w(r)\,dr}{b_2 r_2^2} \qquad \overline{lnrA}(\theta) = \frac{\int_{r_2}^{r_v} \ln\left(\frac{r}{r_2}\right) w(r)\,dr}{b_2 r_2}$$

$$\overline{r^2 A}(\theta) = \frac{\int_{r_2}^{r_v} r^2 w(r)\,dr}{b_2 r_2^3} \qquad \overline{rlnrA}(\theta) = \frac{\int_{r_2}^{r_v} r\ln\left(\frac{r}{r_2}\right) w(r)\,dr}{b_2 r_2^2}$$

Input files of the volute integrals:

name.ext discrete data

$$\theta_i \quad \bar{A}(\theta_i) \quad \overline{rA}(\theta_i) \quad \overline{r^2A}(\theta_i) \quad \overline{lnrA}(\theta_i) \quad \overline{rlnrA}(\theta_i)$$

i.e. $(\theta(i),(aregrl(i,k), k = 1,5), i = 1,n)$

n = number of specified cross-sections

name.SPL cubic spline fit coefficients

$$((C_1(i,k), \quad C_2(i,k), \quad C_3(i,k), \quad C_4(i,k), i=1,n-1), k=1,5)$$

where Spline(θ) =

$$C_1(i,k) + C_2(i,k)(\theta-\theta_i) + C_3(i,k)(\theta-\theta_i)^2 + C_4(i,k)(\theta-\theta_i)^3$$

θ in degrees, measured from the volute tongue in the direction of impeller rotation.

Program I/O

Impeller geometry: r_1, r_2, b_2, w_2 in code

Input:

      Number of integration divisions, nd $\Delta\theta = 2\pi/nd$

      Volute cross-section integral file (discrete data) 'name.ext'

      program will read 'name.SPL' for cubic spline fit coefficients

      Output file name

      Query: store p(θ'), $\beta(\theta_2)$ for θ_i i=1,nd?

      Flow coefficient, ϕ

Find γ (1)   Enter the experimental head rise, search tolerance, and an initial guess of γ

     or   (2)   Enter -1, flow path angle (γ)

              Query: is calculated head rise=experimental value?

                  If no, continue search, request another guess of γ

                  If yes, proceed

output: (files appended)

output.MAT ϕ γ ψ_0 F_{ox} F_{oy} nd

output.PBT ϕ γ ψ_0 F_{ox} F_{oy} nd

              θ'_i D_{pi} β_i for i=1,nd+1

Nomenclature

b_2 width of impeller discharge passage

$D_p(\theta')$ pressure coef. at volute inlet $= \dfrac{p_v(r_2,\theta')-p_{t1}}{.5\ \rho(\Omega r_2)^2}$

F_{ox},F_{oy} components of the steady force on the impeller in the volute frame, nondimensionalized by $\rho\pi b_2\Omega^2 r_2^3$

nd   number of integration divisions

p_{t1},p_{t2} upstream, downstream total pressure

p_v pressure at volute inlet

Q   volume flow rate

r_1,r_2 impeller inlet, discharge radius

$v_r,v\theta$ radial, azimuthal velocity relative to the impeller

w_2 external width of impeller discharge

$\beta(\theta_2)$ impeller relative radial velocity perturbation

$$v_r = \frac{\phi \Omega r_2^2 \beta(\theta_2)}{r}$$

$$\frac{v_\theta}{v_r} = -\tan \gamma \qquad r_1 \le r \le r_2$$

γ impeller relative flow path angle

θ' measured in stationary volute frame from tongue.

θ_2 measured in translating (not rotating) impeller frame.

     (for centered impeller, $\theta' = \theta_2$)

ρ fluid density

ϕ flow coefficient $= Q/(2\pi r_2^2 b_2 \Omega)$

ψ_0 total head coefficient $\dfrac{P_{t2} - P_{t1}}{\rho(\Omega r_2)^2}$

Ω radian freq. of the impeller (shaft) rotation.

ω radian freq. of the circular whirl orbit.

The Fortran source code and sample input file of Adkins/Brennen model are stored in the /u/te/garyc/volute/adkins directory, located at **tyrell.msfc.nasa.gov**.

APPENDIX B

Radial Force Measurements
for the SECA Volute

Robert V. Uy
Christopher E. Brennen
Division of Engineering and Applied Science

Report No. E249.16, 1995

Radial Force Measurements for the SECA volute

Robert V. Uy
Christopher E. Brennen

California Institute of Technology
Pasadena, Calif. 91125

1 INTRODUCTION

This report contains the results of measurements of the steady radial forces on a centrifugal pump impeller produced by a particular volute (the SECA Volute) designed by SECA, Inc. of Huntsville, Alabama, under contract to the NASA George Marshall Space Flight Center. This SECA Volute was designed using CFD methodology which SECA has developed to handle such flows. The purpose of the present tests was to determine experimentally the steady radial forces by making measurements in the Rotor Force Test Facility (RFTF) at the California Institute of Technology. This facility is described in detail elsewhere (Chamieh *et al.* 1985, Jery *et al.* 1985, Brennen *et al.* 1986, Adkins and Brennen 1988, Arndt and Franz 1986) and will not be repeated here. For the purposes of the present tests, the fundamental components of the RFTF are as follows. A centrifugal impeller, Impeller X, is driven by an electric motor at speeds up to 2000rpm. The impeller is mounted directly onto a rotating internal balance or dynamometer which measures the forces imparted to it by the impeller. The forces are measured using strain gauges whose output signals emerge through slip rings and are processed by a bank of instrumentation amplifiers. Since the forces sensed by the balance are in a rotating frame, it is necessary to resolve them into forces in the laboratory frame. The time averaged components of the radial forces are as defined in figure 1 where F_x^* is in the direction of the volute cutwater and F_y^* is perpendicular to this. In section 3, we will briefly describe the impeller and various volutes used in the present tests.

The radial forces will be presented here in nondimensional form by dividing the forces by $\rho\pi\Omega^2 R^3 L$, where ρ is the fluid density, Ω is the rotational speed (in radians/sec), R is the discharge radius and L is the width of the impeller discharge. The non-dimensional forces will be denoted by F_x and F_y. The magnitude of the dimensionless radial force will be denoted by $F_0 = (F_x^2 + F_y^2)^{\frac{1}{2}}$, and its direction, θ, will be measured from the tongue or cutwater of the volute in the direction of rotation.

2 RADIAL FORCES

The existence of radial forces, and attempts to evaluate them, date back to the 1930s (see Stepanoff's comment in Biheller 1965) or earlier. The nonaxisymmetries which produce the radial forces depend upon the geometry of the impeller and the volute as well as the flow coefficient, ϕ. The latter is defined as $Q/A\Omega R$ where Q is the volume flow rate through the pump and A is the area of impeller discharge. Measurements of radial forces have been made with a number of different impeller/volute combinations by Agostonelli *et al.* (1960), Iverson *et al.* (1960), Biheller (1965), Grabow (1964), Domm and Hergt (1970), Chamieh *et al.* (1985), and Franz and Arndt (1986) among others.

Some typical nondimensional radial forces obtained experimentally by Chamieh *et al.* (1985) for the Impeller X/Volute A combination (see below) are shown in figure 2 for a range of speeds and flow coefficients. Note that the "design" objective that Volute A be well matched to Impeller X appears to be satisfied at a flow coefficient, ϕ, of 0.092 where the magnitude of the radial force appears to vanish.

The dependence of the radial forces on volute geometry is illustrated in figure 4 from Chamieh *et al.* (1985) which presents a comparison of the magnitude of the force on Impeller X due to Volute A with the
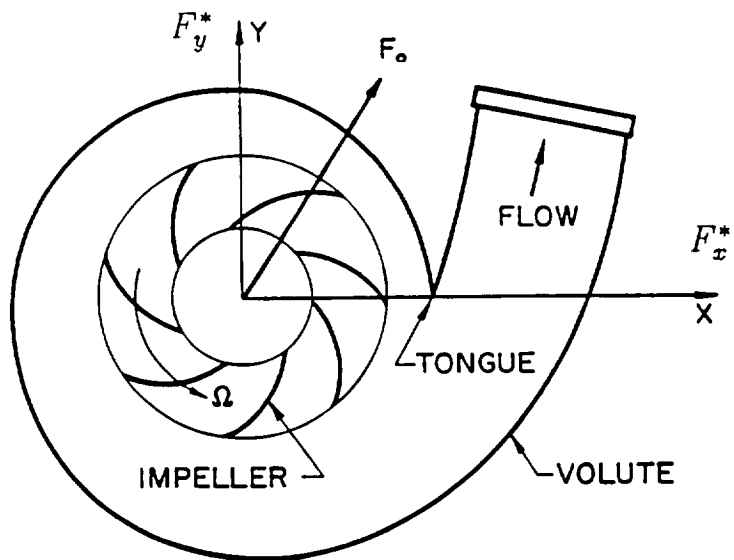
Figure 1: Schematic showing the definition of the radial forces. F_x^* and F_y^*, within the volute geometry as seen from the inlet to the pump.
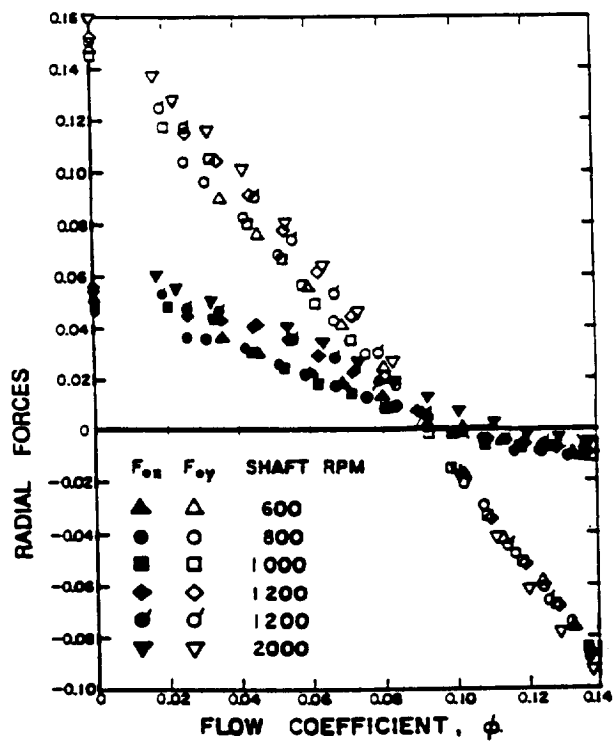
Figure 2: Radial forces for the centrifugal Impeller X/Volute A combination as a function of shaft speed and flow coefficient (Chamieh et al. 1985).

3
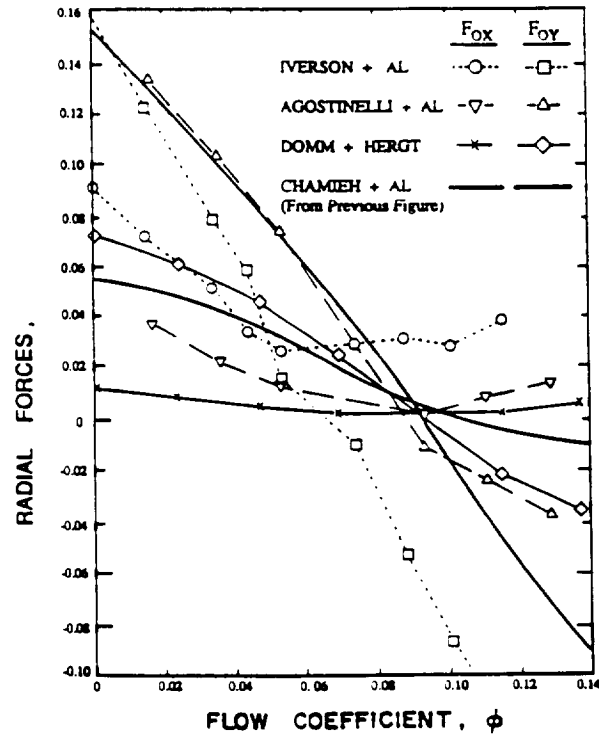
Figure 3: Comparison of the radial forces measured by Iverson, Rolling and Carlson (1960) on a pump with a specific speed, N_D, of 0.36, by Agostinelli, Nobles and Mockeridge (1960), on a pump with $N_D = 0.61$, by Domm and Hergt (1970), and by Chamieh et al. (1985) on a pump with $N_D = 0.57$.
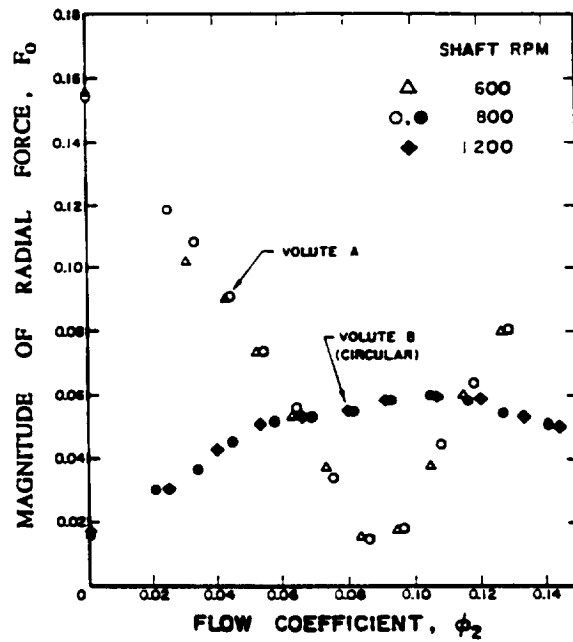
Figure 4: Comparison of the magnitude of the radial force (F_0) on Impeller X caused by Volute A and by the circular Volute B with a circumferentially uniform area (Chamieh et al. 1985).

4
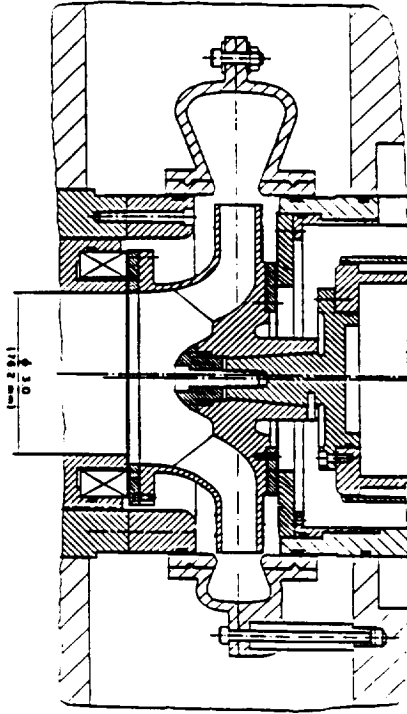
Figure 5: Schematic of the impeller/volute arrangement in the RFTF used in the experiments of Chamieh *et al.* (1985).

magnitude of the force due to a circular volute with a circumferentially uniform cross-sectional area. In theory, Volute B could only be well-matched at zero flow rate; note that the results do exhibit a minimum at shut-off. Figure 4 also illustrates one of the compromises that a designer may have to make. If the objective were to minimize the radial force at a single flow rate, then a well-designed spiral volute would be appropriate. On the other hand, if the objective were to minimize the force over a wide range of flow rates, then a quite different design, perhaps even a constant area volute, might be more effective. Of course, a comparison of the hydraulic performance would also have to be made in evaluating such design decisions.

In the past a number of different configurations of the "seal" at the impeller discharge/volute inlet were employed during measurements of the Impeller X/Volute A radial forces. Specifically, figures 5. 6 and 7 show the different configurations employed by Chamieh *et al.* (1985), Adkins and Brennen (1988) and Franz *et al.* (1990), respectively (figure 8 shows the configuration employed in the current tests for both the Volute A and the SECA Volute tests). Because the leakage flows in this region have an important effect on the pressure distributions acting on the impeller discharge and on the shroud, the radial forces differ somewhat for each of these configurations. Further comment on these effects will be included later.

Visualizing the centrifugal pump impeller as a control volume, one can recognize three possible contributions to the radial force. First, circumferential variation in the impeller discharge pressure (or volute pressure) will clearly result in a radial force acting on the impeller discharge area. A second contribution could be caused by the leakage flow from the impeller discharge to the inlet between the impeller shroud and the pump casing. Circumferential nonuniformity in the discharge pressure could cause circumferential nonuniformity in the pressure within this shroud-casing gap, and therefore a radial force acting on the exterior of the pump shroud. For convenience, we shall term this second contribution the leakage flow contribution. Third, a circumferential nonuniformity in the flow rate out of the impeller would imply a force due to the nonuniformity in the momentum flux out of the impeller. This potential third contribution has not been significant in any of the studies to date. Both the first two contributions appear to be important.

In order to investigate the origins of the radial forces. Adkins and Brennen (1988) (see also Brennen *et al.* 1986) made measurements of the pressure distributions in the Volute A, and integrated these pressures to evaluate the contribution of the discharge pressure to the radial force. Typical pressure distributions for
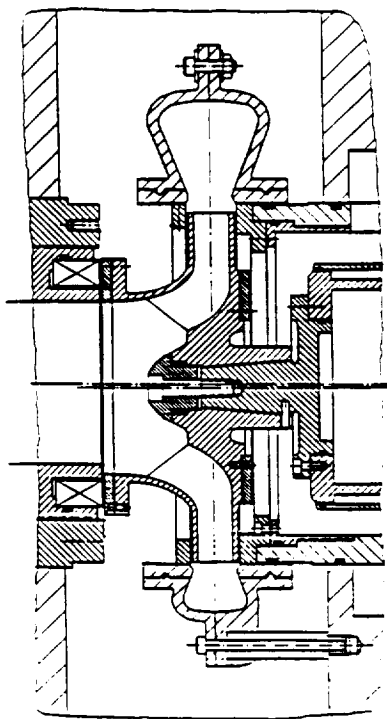
Figure 6: Schematic of the impeller/volute arrangement in the RFTF used in the experiments of Adkins and Brennen (1988).
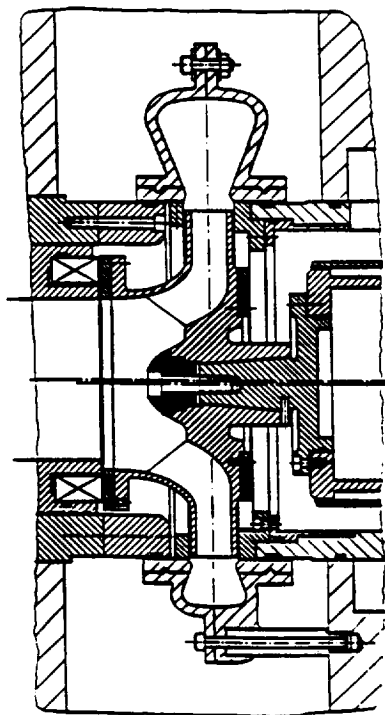
Figure 7: Schematic of the impeller/volute arrangement in the RFTF used in the experiments of Franz *et al.* (1990).
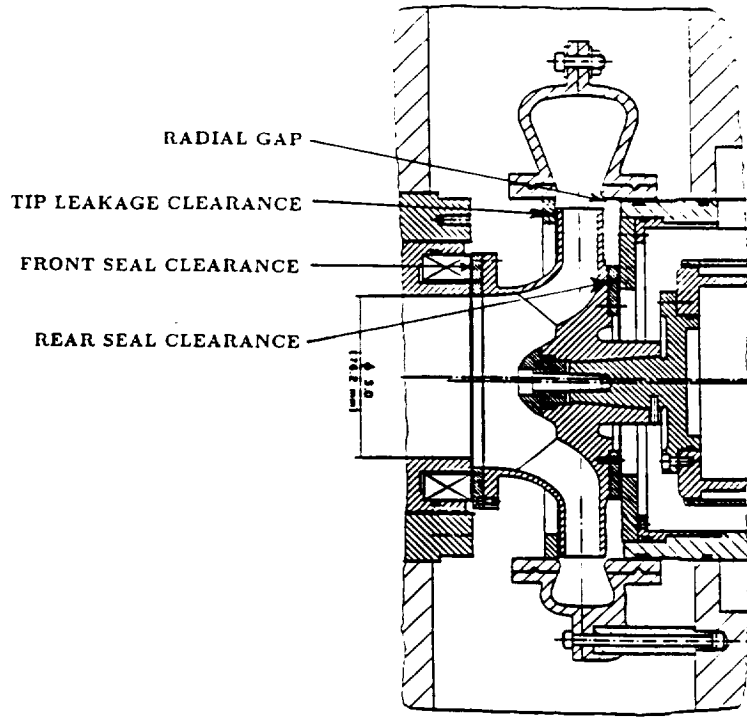
Figure 8: Schematic of the impeller/volute arrangement in the RFTF used in the current tests.
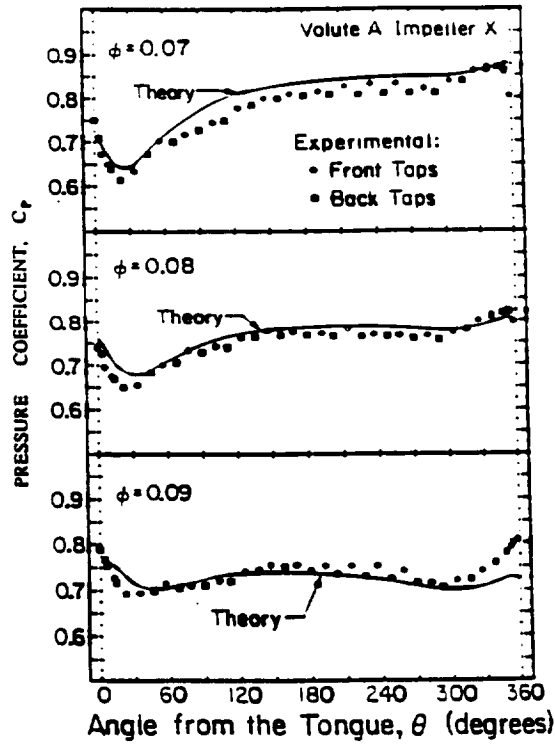
Figure 9: Circumferential pressure distributions in the impeller discharge for the Impeller X/Volute A combination at three different flow rates. Also shown are the theoretical pressure distributions of Adkins and Brennen (1988).
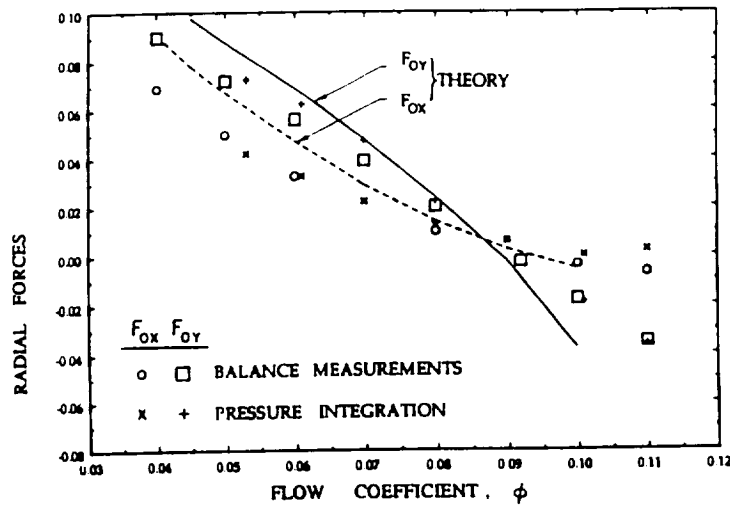
Figure 10: Comparison of radial forces from direct balance measurements. from integration of measured pressures. and from theory for the Impeller X/Volute A combination (from Adkins and Brennen 1988).

the Impeller X/Volute A combination (with the flow separation rings of figure 6 installed) are presented in figure 9 for three different flow coefficients. Minor differences occur in the pressures measured in the front sidewall of the volute at the impeller discharge (front taps) and those in the opposite wall (back taps). The experimental measurements in figure 10 are compared with theoretical predictions based on an analysis that matches a guided impeller flow model with a one-dimensional treatment of the flow in the volute (Adkins and Brennen 1988), a theory which is similar in spirit to that proposed by Lorett and Gopalakrishnan (1983).

Integration of the experimental pressure distributions yielded radial forces in good agreement with both the overall radial forces measured using the force balance and the theoretical predictions of the theory. These results demonstrate that it is primarily the circumferential nonuniformity in the pressure at the impeller discharge that generates the radial force. The theory clearly demonstrates that the momentum flux contribution is negligible.

The leakage flow from the impeller discharge, between the impeller shroud and the pump casing, and back to the pump inlet does make a significant contribution to the radial force (Adkins and Brennen 1988, Guinzburg et al. 1990). Adkins and Brennen obtained data with and without the "flow separation rings" of figure 6. The data of figures 9 and 10 were taken with these rings installed. The measurements showed that, in the absence of the rings, the nonuniformity in the impeller discharge pressure caused significant nonuniformity in the pressure in the leakage annulus, and, therefore, a significant contribution from the leakage flow to the radial force. This was not the case once the rings were installed, for the rings partially isolated the leakage annulus from the impeller discharge nonuniformity. However, a compensating mechanism exists which causes the total radial force in the two cases to be more or less the same. The increased leakage flow without the rings tends to relieve some of the pressure nonuniformity in the impeller discharge, thus reducing the contribution from the impeller discharge pressure distribution.

3 PUMP, IMPELLER AND VOLUTES

It is appropriate at this point to include a brief description of the pump components used in the present tests.

Impeller X, which is shown in figure 11, is a five-bladed centrifugal pump impeller made by Byron Jackson Pump Division of Borg Warner International Products. It has a discharge radius, $R = 8.1$ cm, a discharge blade angle of $23°$, and a design specific speed, N_D, of 0.57.

In past studies frequent use was made of a volute designated Volute A (figure 12) which is a single exit, spiral volute with a base circle of 18.3 cm and a spiral angle of $4°$. It is designed to match Impeller X at a flow coefficient of $\phi = 0.092$. This implies that the principles of fluid continuity and momentum have been

ALL DIMENSIONS
IN CENTIMETERS
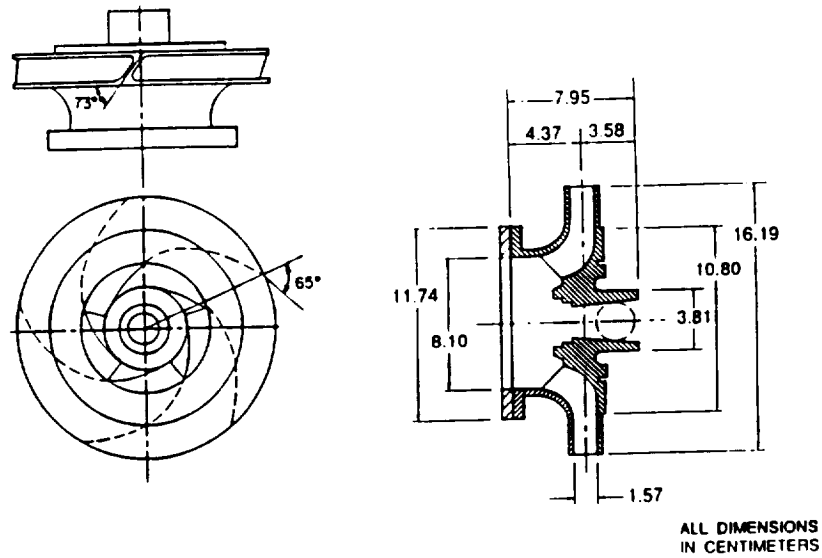
Figure 11: A centrifugal pump impeller designated Impeller X.
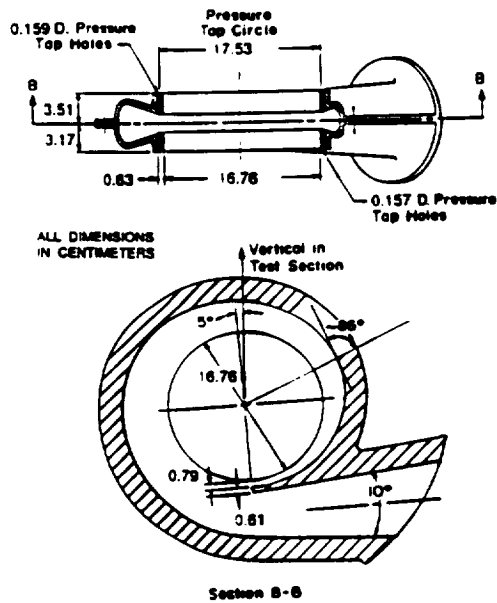
Figure 12: A vaneless spiral volute (designated Volute A) designed to be matched to Impeller X.

utilized in the design. so that the volute collects a circumferentially uniform discharge from the impeller and channels it to the discharge line in such a way that the pressure in the volute is circumferentially uniform, and in a way that minimizes the viscous losses in the decelerating flow. For given volute and impeller geometries. these objectives can only by met at one "design" flow coefficient. In the present tests measurements of the forces on Volute A were included in order to provide a point of reference to the previous data base.

Also in the past. measurements were made (Chamieh *et al.* 1985) with a volute with a circumferentially uniform area called Volute B.

However. the purpose of the present tests was to obtain comparable data using SECA Volute. This volute was fabricated elsewhere and shipped to Caltech. Some minor machining to the exterior was necessary in order to fit the SECA Volute into the RFTF but this had no effect upon the interior flow. The SECA Volute was also provided with a circular array of pressure taps on the interior circumference. both on the front (or flow inlet) surface and on the back (or drive shaft) surface. These were connected to banks of manometers in order to measure the circumferential pressure distribution within the flow discharging from the impeller and entering the volute. Similar measurements were carried out in the past on Volute A by Adkins and Brennen (1988). In this report we present not only measurements of the radial forces obtained using the internal balance but also pressure distributions obtained using these pressure taps. The pressure distributions will also be integrated to obtain values for the contributions to the overall radial forces due to nonuniformities in the circumferential pressure distribution acting on the impeller discharge.

4 MEASUREMENT PROCEDURES

As in all past experiments. "dry" runs (experiments without water in the RFTF) were first conducted in order to determine the tare forces registered by the internal balance. These tare forces were subtracted from the "wet" runs to obtain the fluid forces imparted to the impeller by the flow. In addition the buoyancy force acting on the submerged impeller was subtracted from the wet runs; this buoyancy force was obtained by manually positioning the impeller in several different rotational orientations.

5 FORCE BALANCE DATA FOR VOLUTE A

The first set of measurements carried out during the current investigation consisted of further measurements on the Impeller X/Volute A combination in order to provide a point of comparison for the later measurements with the SECA Volute. Figure 13 presents the nondimensional forces in the x and y directions obtained at a rotational speed of $2000rpm$ over a range of flow coefficients. This data is similar to, but not identical to, previous measurements on the same combination obtained by Chamieh *et al.* (1985), Adkins and Brennen (1988) and Franz *et al.* (1990). This previous data is compared with the current measurements in figures 14 and 15. The differences can be ascribed to the differences in the impeller discharge/volute inlet configuations shown in figure 5 through 7. Specifically, the configuration used by Chamieh *et al.* (1985) (figure 5) is substantially different from that used by Adkins and Brennen (1988) (figure 6) or Franz *et al.* (1990) (figure 7) since the absence of the flow separation rings reduces the pressure nonuniformity in the impeller discharge but increases the pressure nonuniformity acting on the exterior of the shroud. The data of figures 14 and 15 reflect this configurational difference since the data from Adkins and Brennen (1988) and Franz *et al.* (1990) is quite similar.

Some additional documentation on the current configuration should be recorded. Referring to figure 8 we note that

- The radial gap is a uniform $0.094in$.

- The rear seal axial clearance is a uniform $0.004in$.

- The tip leakage axial clearance is a uniform $0.007in$.

- The front seal axial clearance was made as uniform as possible but still varied from $0.004in$ at top dead center to $0.006in$ at bottom dead center.

10
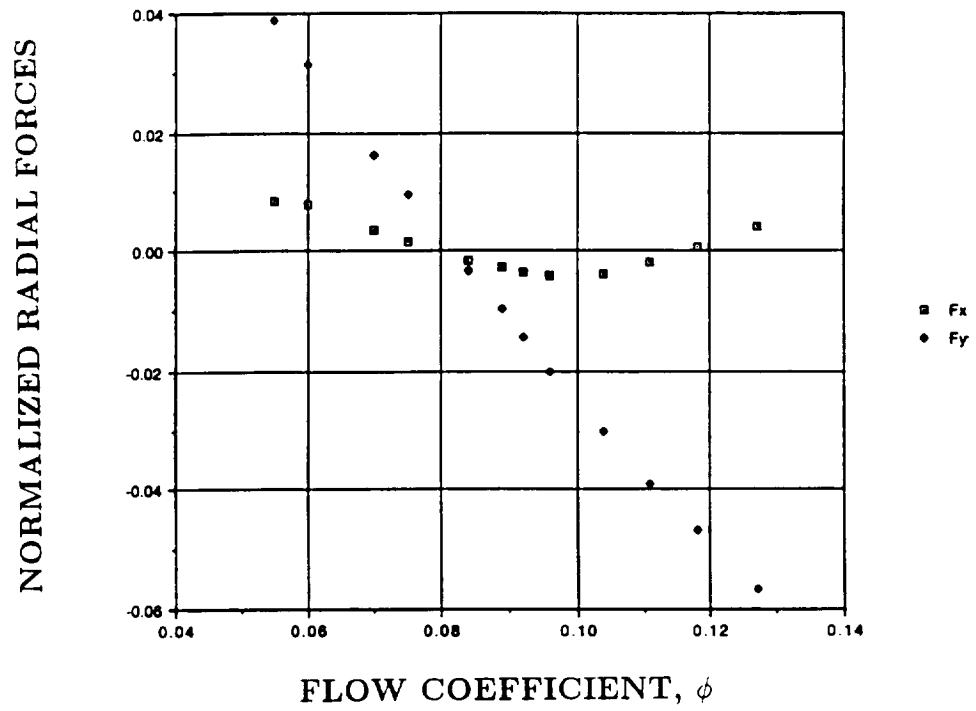
Figure 13: Current measurements of the radial forces for the Impeller X/Volute A combination obtained at 2000rpm.
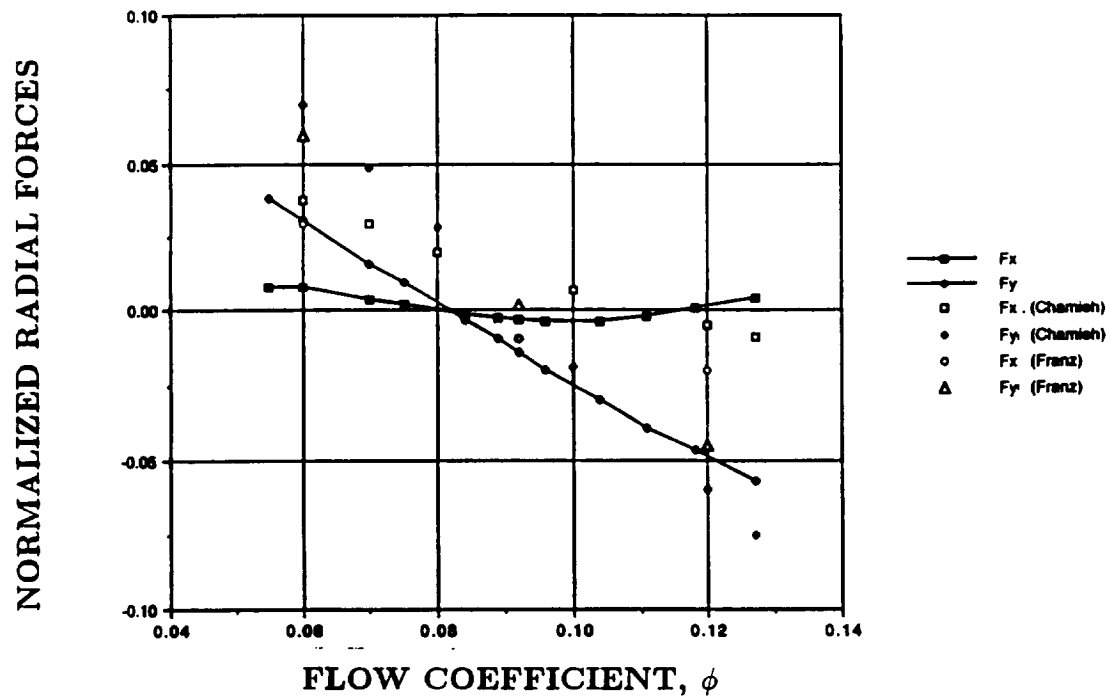
Figure 14: Comparison of the current measurements of the radial forces for the Impeller X/Volute A combination with those obtained by Chamieh et al. (1985) and Franz et al. (1990).

11
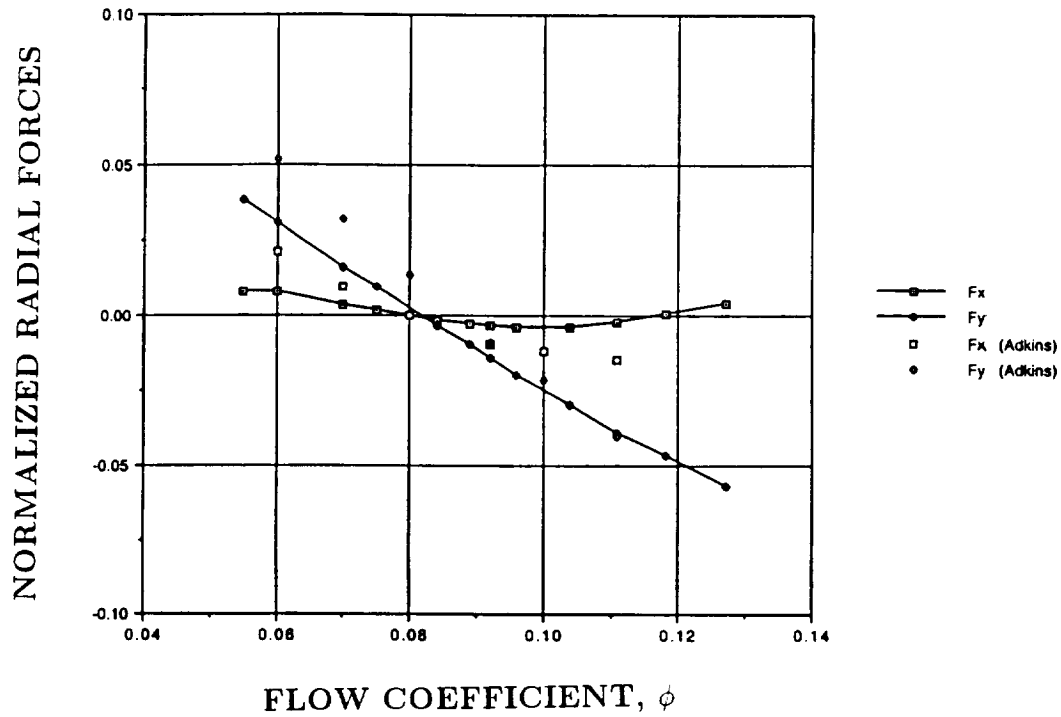
Figure 15: Comparison of the current measurements of the radial forces for the Impeller X/Volute A combination with those obtained by Adkins *et al.* (1988).

Note also from figure 8 that the current configuration differs somewhat from all three earlier configurations. It has greater similarity to Adkins and Brennen (1988) and Franz *et al.* (1990) than it does to Chamieh *et al.* (1985) and the data of figures 14 and 15 show that the current forces display a similar relationship.

6   FORCE BALANCE DATA FOR THE SECA VOLUTE

The radial forces, F_x and F_y, produced by the SECA Volute are presented in figure 16. Data was obtained at both 2000rpm and at 1800rpm and it can be clearly seen from figure 15 that the non-dimensional data for the two speeds is consistent. This has also been our past experience and indicates that Reynolds number effects upon these results are minimal. Note that the magnitude of the force exhibits a minimum at a flow coefficient of about 0.09 which seems to be the effective design flow coefficient for this impeller/volute combination.

Also note by comparing figures 16 and 13 that the SECA Volute yields a small reduction in the magnitude of the radial force when compared with Volute A. However they both yield very similar results.

7   PRESSURE DISTRIBUTIONS

The circular arrays of pressure taps located on the interior surface of the SECA Volute just inside the volute inlet were connected to manometer banks and data on the pressure distributions were obtained at two speeds (1800rpm and 2000rpm) and several flow coefficients. The pressures were converted to pressure coefficients by normalizing with respect to the dynamic pressure corresponding to the impeller tip speed (the reference pressure is inconsequential). These pressure coefficients were then plotted against position as represented by the angle from the cutwater measured in the direction of impeller rotation. Similar plots were constructed by Adkins and Brennen (1988); a sample was presented earlier in figure 9.

Five different pressure distributions for the SECA Volute are presented in figures 17 through 21, a series with ascending flow coefficient. Several features of these pressure distributions are particularly noteworthy.
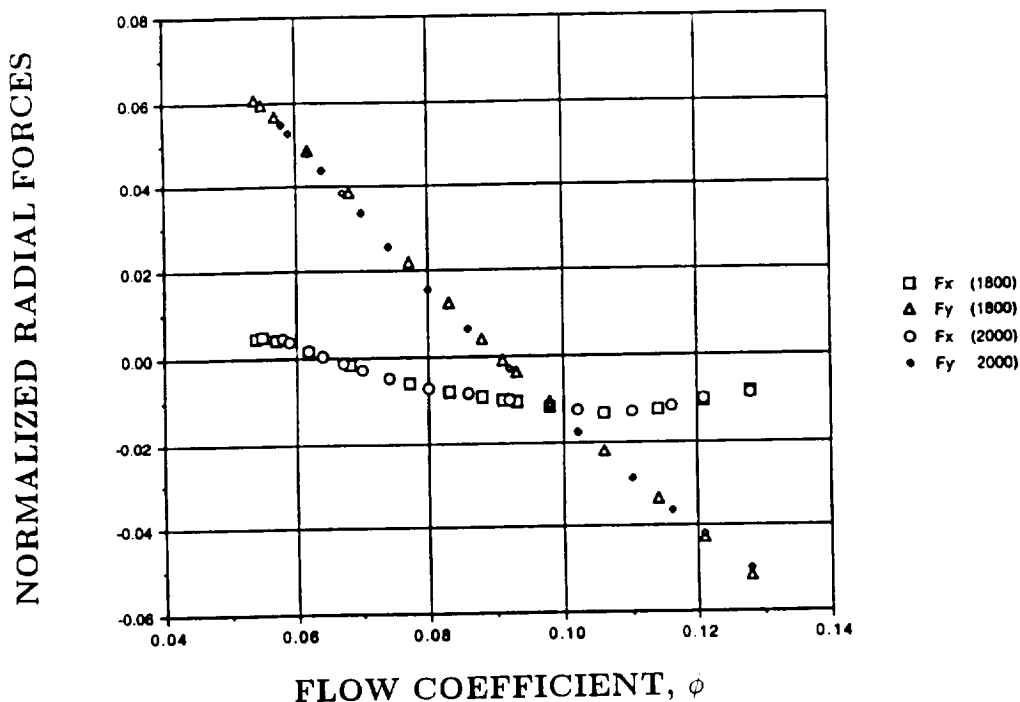
Figure 16: Measurements of the normalized radial force components. F_x and F_y, for the SECA Volute plotted against flow coefficient. Data is shown for both 2000rpm and 1800rpm.

First though they evolve in a way which is somewhat similar to Volute A (figure 9) they have a distinctively different shape in which the major pressure rise at low flow coefficients occurs upstream of the cutwater, while, at higher flow coefficients the pressure decreases fairly uniformly around the circumference.

The data for the front taps seems more consistent than that for the back taps, perhaps because of local flow separation. However it seems clear that the back tap pressures are significantly higher at lower flow coefficients, suggesting that, under these conditions, the impeller discharge flow is not precisely radial but has a component in the axial direction of the inlet flow. This trend seems to fade at higher flow coefficients and the front and back tap data then yield similar results.

8 COMPARISON OF BALANCE AND PRESSURE FORCES

The pressure distributions of the last section were integrated over the area of the impeller discharge (using the front tap distributions) in order to obtain the contribution of the nonuniformity in the pressure around the discharge to the radial forces. The magnitudes of the forces obtained in this way are compared in figure 22 with those measured using the internal balance. Data for both 2000rpm and at 1800rpm is included. Note that the integrated pressure forces constitute about 60% to 80% of the total forces measured by the balance.

A second comparison between the balance measurements and the integrated pressure forces is included in figure 23 where the individual components of the forces are presented. Note that the force contributed by the discharge pressure seems to have a somewhat different direction from the additional forces (probably acting on the shroud). This results in a different variation of F_x with flow coefficient.

9 CONCLUSIONS

The radial force data obtained for the SECA Volute using both the internal balance and integration of the pressure distributions suggests that the SECA Volute is yields marginally smaller forces than the logarithmic

13

C-2
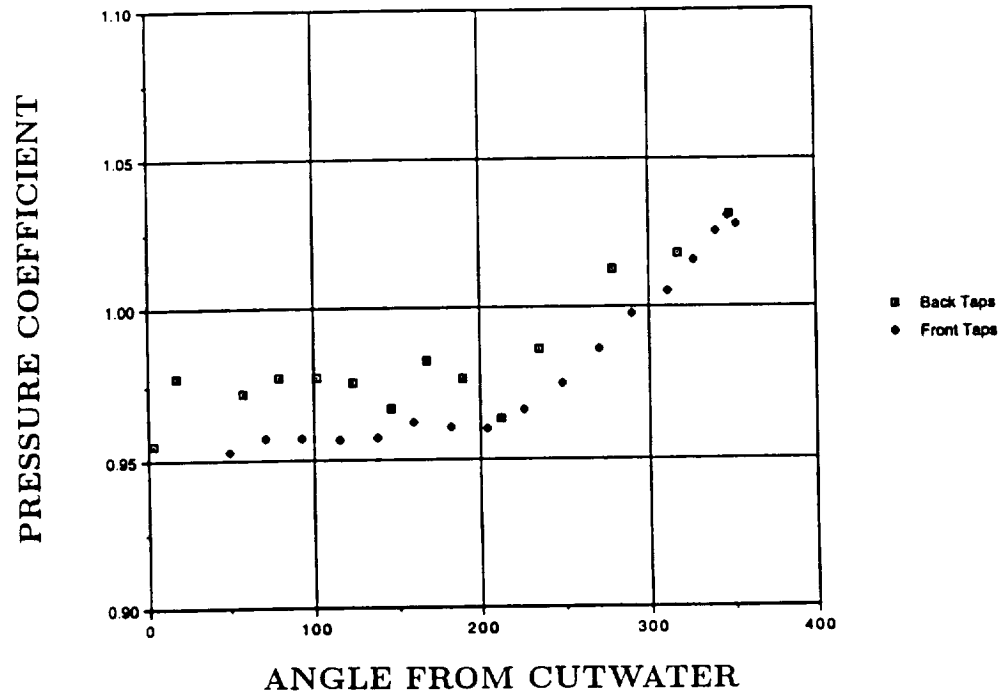
Figure 17: Pressure distributions for the SECA Volute operating at $1800rpm$ and a flow coefficient of 0.074.
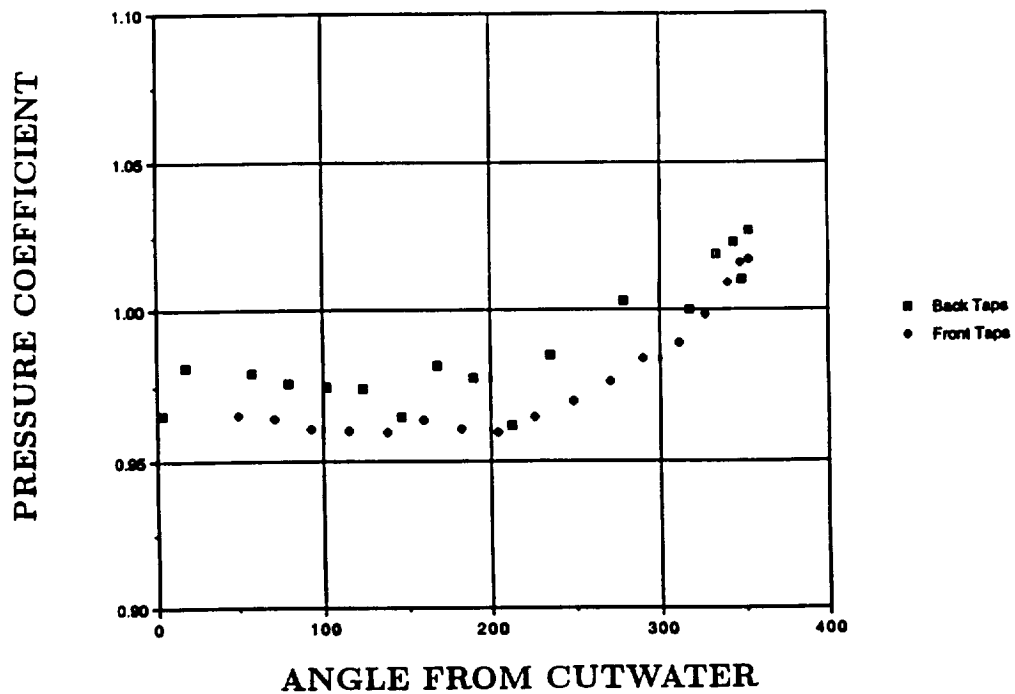
Figure 18: Pressure distributions for the SECA Volute operating at $2000rpm$ and a flow coefficient of 0.079.
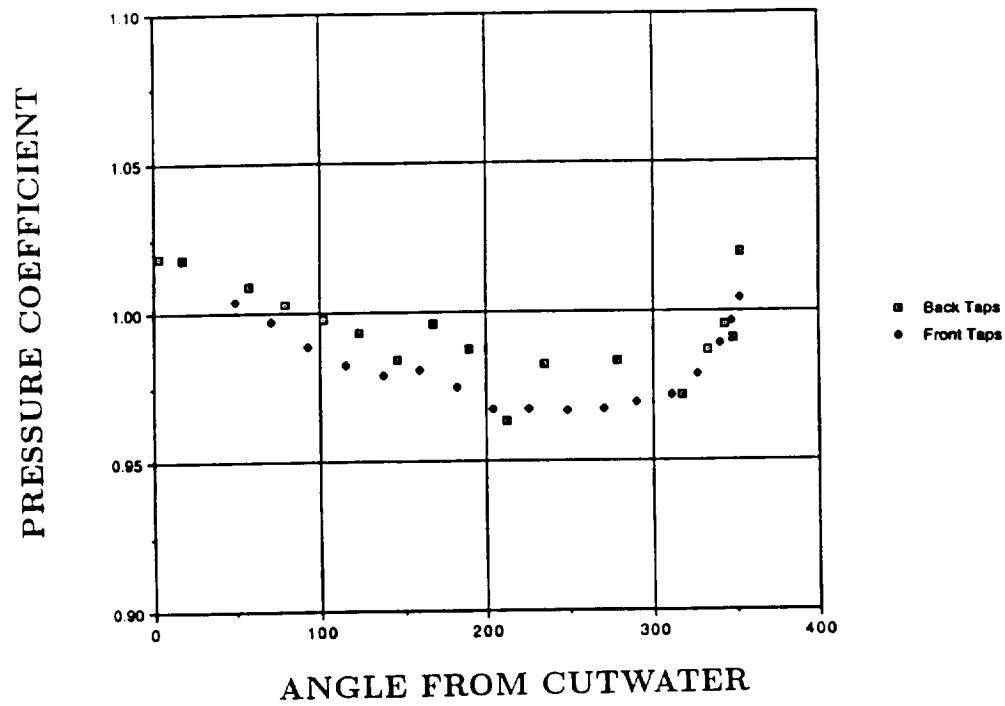
Figure 19: Pressure distributions for the SECA Volute operating at $1800rpm$ and a flow coefficient of 0.092.
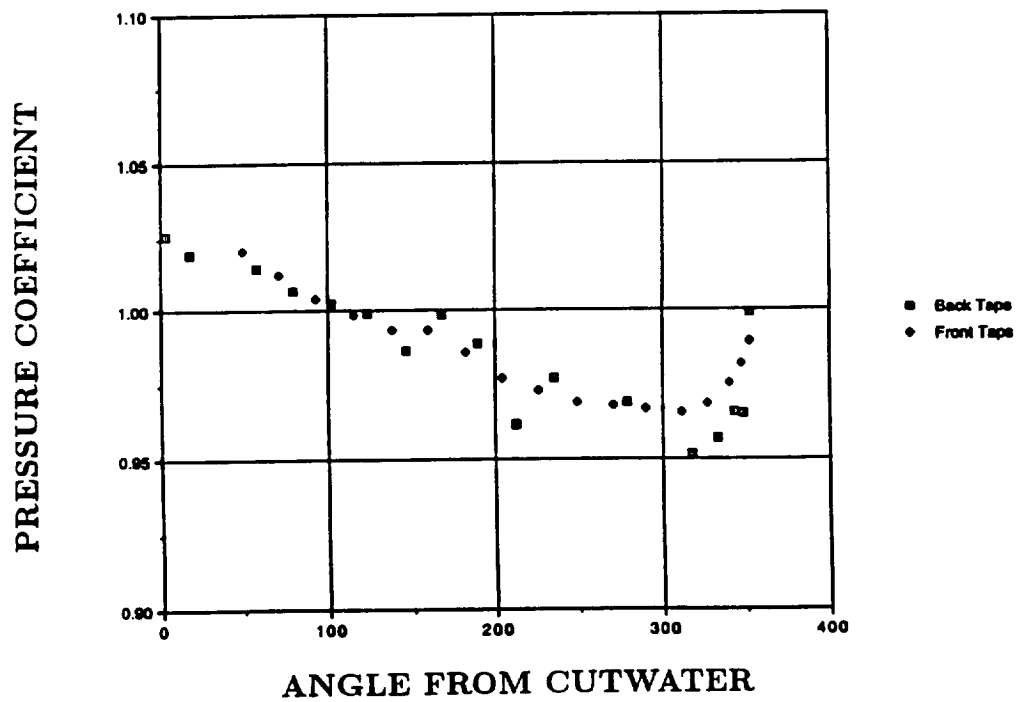
Figure 20: Pressure distributions for the SECA Volute operating at $2000rpm$ and a flow coefficient of 0.098.

15
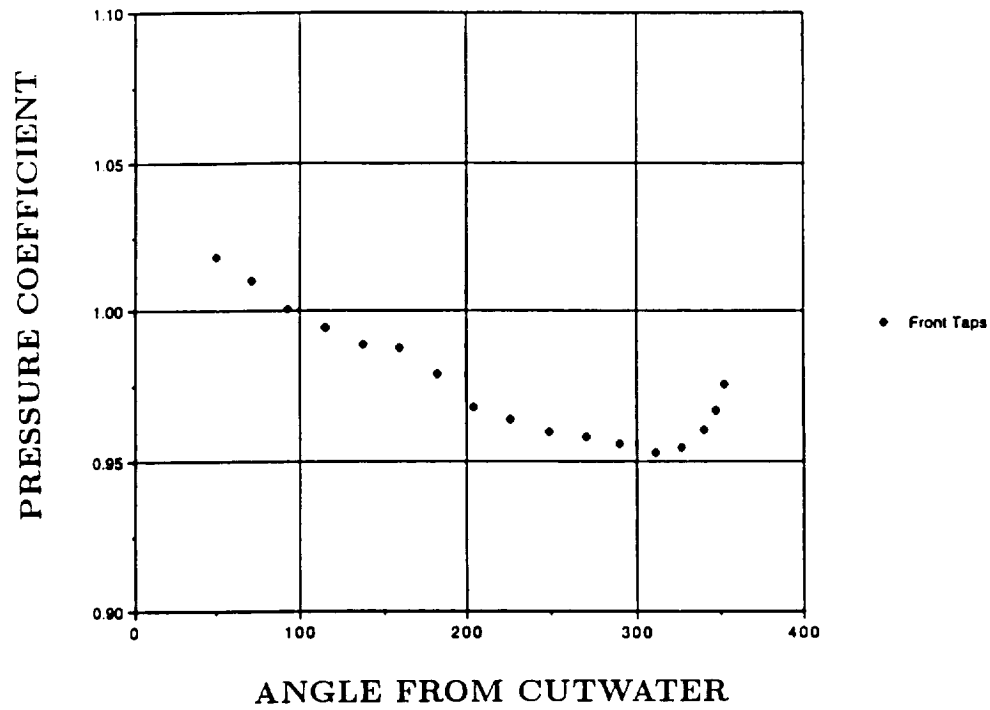
Figure 21: Pressure distributions for the SECA Volute operating at 1800rpm and a flow coefficient of 0.100.
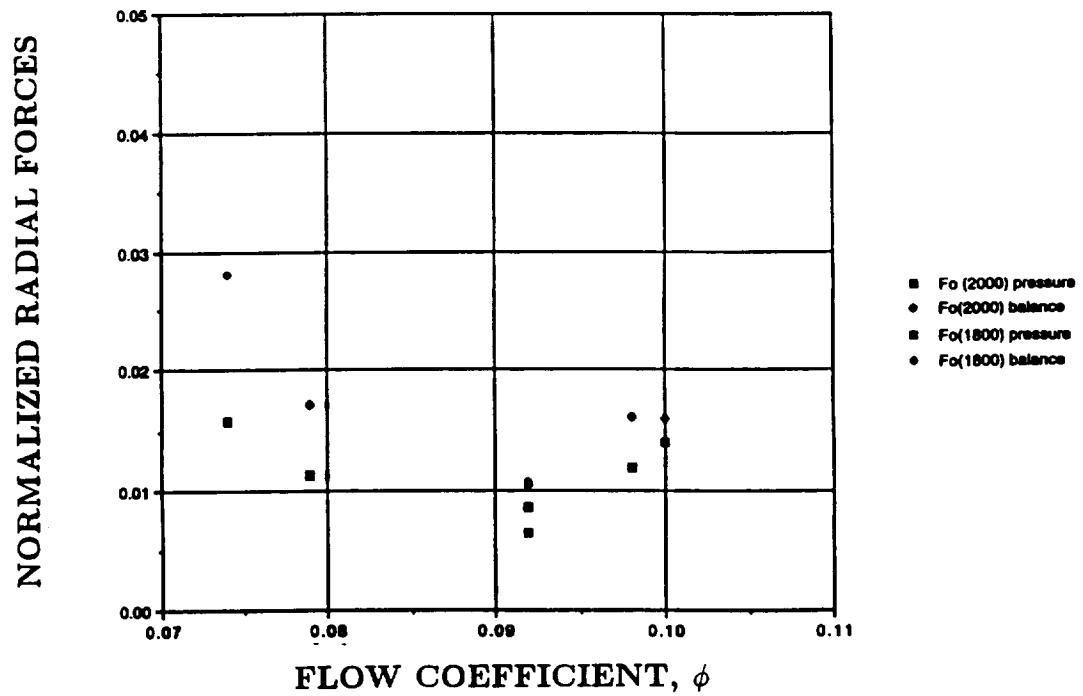
Figure 22: Measurements of the magnitude, F_0, of the radial force for the SECA Volute obtained at 2000rpm and at 1800rpm. Both balance measurements and pressure integration measurements are shown.
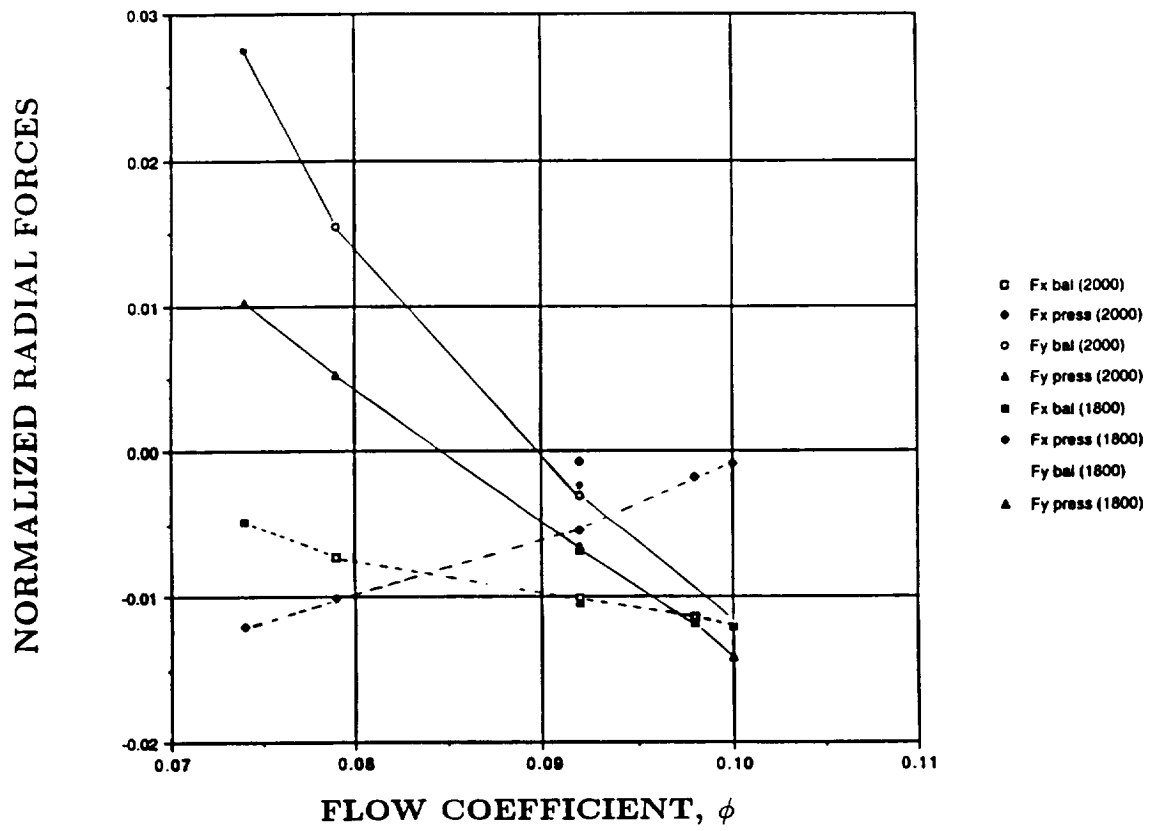
Figure 23: The components, F_x and F_y, of the radial force for the SECA Volute obtained at $2000rpm$ and at $1800rpm$. Both balance measurements and pressure integration measurements are shown.

spiral Volute A but the differences are not large.

10   ACKNOWLEDGEMENTS

11   REFERENCES

Adkins. D.R. and Brennen. C.E. (1988). Analyses of hydrodynamic radial forces on centrifugal pump impellers. *ASME J. Fluids Eng.*, **110**. No. 1. 20-28.

Agostinelli. A., Nobles, D. and Mockridge. C.R. (1960). An experimental investigation of radial thrust in centrifugal pumps. *ASME J. Eng. for Power.* **82**, 120-126.

Arndt. N. and Franz. R. (1986). Observations of hydrodynamic forces on several inducers including the SSME LPOTP. *Calif. Inst. of Tech.. Div. Eng. and Appl. Sci.. Report No. E249.3.*

Biheller. H.J. (1965). Radial force on the impeller of centrifugal pumps with volute. semi-volute and fully concentric casings. *ASME J. Eng. for Power. July 1965.* 319-323.

Brennen. C.E.. Acosta. A.J., and Caughey, T.K. (1986). Impeller fluid forces. *Proc. NASA Advanced Earth-to-Orbit Propulsion Technology Conference. Huntsville. AL, NASA Conf. Publ. 2436,* 270-295.

Chamieh. D.S., Acosta, A.J., Brennen, C.E., and Caughey, T.K. (1985). Experimental measurements of hydrodynamic radial forces and stiffness matrices for a centrifugal pump-impeller. *ASME J. Fluids Eng.*, **107**, No. 3, 307-315.

Domm, H. and Hergt, P. (1970). Radial forces on impeller of volute casing pumps. In *Flow Research on Blading* (ed: L.S. Dzung), Elsevier Publ. Co., 305-321.

Franz, R. and Arndt, N. (1986). Measurements of hydrodynamic forces on the impeller of the HPOTP of the SSME. *Calif. Inst. of Tech., Div. Eng. and Appl. Sci., Report No. E249.*

Franz, R., Acosta, A.J., Brennen, C.E., and Caughey, T.K. (1990). The rotordynamic forces on a centrifugal pump impeller in the presence of cavitation. *ASME J. Fluids Eng.*, **112**, 264-271.

Grabow, G. (1964). Radialdruck bei Kreiselpumpen. *Pumpen und Verdichter*, No. 2, 11-19.

Guinzburg, A., Brennen, C.E., Acosta, A.J., and Caughey, T.K. (1990). Measurements of the rotordynamic shroud forces for centrifugal pumps. *Proc. ASME Turbomachinery Forum*, **FED-96.** 23-26.

Hergt, P. and Krieger, P. (1969-70). Radial forces in centrifugal pumps with guide vanes. *Proc. Inst. Mech. Eng.*, **184**, Part 3N, 101-107.

Iversen, H.W., Rolling, R.E., and Carlson, J.J. (1960). Volute pressure distribution, radial force on the impeller and volute mixing losses of a radial flow centrifugal pump. *ASME J. Eng. for Power*, **82**, 136-144.

Jery, B., Acosta, A.J., Brennen, C.E., and Caughey, T.K. (1985). Forces on centrifugal pump impellers. *Proc. Second Int. Pump Symp., Houston, Texas*, 21-32.

Lorett. J.A. and Gopalakrishnan, S. (1983). Interaction between impeller and volute of pumps at off-design conditions. *Proc. ASME Symp. on Performance Characteristics of Hydraulic Turbines and Pumps*, **FED-6**, 135-140.

APPENDIX C

Operational Instructions for the
Volute Geometry Generation Code

Discussion

The volute grid generation code that was developed as part of this contract is contained on the UNIX tar tape VOLO1.TAP that is a part of the final documentation and deliverables. The executable is named gdv and can be generated using the makefile - mkgdv. The input data files required to execute the code are: Coordinate mapping file, geometry file, and a grid stretching file. The input files contained on the tar tape that are used in this section to demonstrate the operation of the code are: volnrn.dat, vol_bud.dat, volstr.dat, respectively. Tables 1-3 list these three files for the sample case described in this Appendix.

The grid code is an interactive code that responds to user responses to queries by the code. The operation of the code requires two cycles through the mapping portion of the code which generates two files that describe the volute surface using a physical-surface coordinate mapping natural to the spiral, discharge and tongue regions. The first mapping cycle generates the mapping file that describes the surface of the volute except for the tongue region. The output file for the first mapping is named by the user (in the sample case - vcp_bud.gi). This file is subsequently used in the first grid generation cycle. The second mapping cycle defines the tongue area surface. This cycle outputs a second user specified mapping file (sample case - vcm_bud.gi), that is subsequently used in the second cycle through the grid generation module.

After the two mapping cycles are completed and control has returned to the top manu, the user should exit the code since there is presently a "bug" in the code that does not allow cycling through the grid portion until all the files are closed. The user can then re-execute the code and proceed to perform the actual grid generation and preparation of the FDNS grid file.

The first cycle through the actual grid generation part of the code requires the user to enter the first mapping file name (jcp_bud.gi). The code will also ask to enter a file name to store the grid data. The user should enter a file name for this first cycle (vcp_bud.b) as this output file can be used by the second cycle as an input file to avoid having to regenerate this data during the second cycle. After the first cycle has been computed, the grid file generated (vcp_bud.b) and control returned to the top menu, the user should select option b to specify the name of the binary grid file (jcp_bud.b) in order to retrieve the previously generated grid data.

Once this has been accomplished, the user then runs the grid generator a second time by inputting the second mapped file name (vcm_bud.gi). Both cycles through the grid generation have prompts for saving intermediate files for debug purposes. The user may or may not save these files except for the second cycle where the user is asked: 'Store internal grid for nreg=6?.' In this case, the user must respond with 'y' in order to generate the FDNS grid file. The FDNS file is output to file vcm_bud.v6 for the sample case shown. The FDNS file will always have as a first part of the file named the same as the first part of the second mapped file name. The FDNS grid file is in the binary format type for FDNS.

Table A-4 lists all the prompts and responses that are required to generate an FDNS grid for the sample case.

In order to simulate a volute flowfield, users need to run the grid generator, /u/te/garyc/volute/gridgen.ex located at tyrell.msfc.nasa.gov, to construct numerical grids. The volute grid generator will create a file which contains the numerical grid coordinates. The initial flowfield must be estimated directly by the user. Once the grid generation is completed, rename (or link) the file which contains grid coordinates to fort.12, and rename (or link) the file of initial flowfield to fort.13, which are the default Fortran units where the FDNS code reads in the data of grid coordinates and flowfield. After the above steps are completed, users can execute the FDNS flow solver, /u/te/garyc/volute/xfdns located at tyrell.msfc.nasa.gov. The details of running the FDNS code are described in the FDNS user's guide (1993).

Table A-1 Listing of Sample Problem Coordinate Mapping Input File - volnrn.dat

```
#  nrng_region  for grid and mapping generators
#  first character:  #-comment
#                    s,t,d,  nr_spiral,tongue,discharge
#                    m,c    nr_mapping: theta,c
#                    n-quit
# s  nr_spiral
#      1,5,8,11,15,9,9,9,9,9
#      1,5,8,10,12,14,16,18,10,10
#      1,4,7,10,13,16,19,22,25,27
#j     1,3,0,4,7,8,9,11,10,10
#j     1,3,5,6,7,8,9,11,10,10  before inlet fillet
#s  nr_spiral  test inlet fillet, fillet conv
#      1,3,6,9,11,9,9,9,9,9
#      1,7,0,8,11,12,13,15,10,10
#      1,4,7,10,13,16,19,22,25,27
# spiral j should have j4-j2 > j8-j7
s  nr_spiral
       1,3,6,9,11,9,9,9,9,9
       1,3,0,7,8,0,9,10, 10,10
       1,4,7,10,13,16,19,22,25,27
#mar  1,7, 0, 0,17,19, 0, 0,30,32
#j    1,3,0,7,8,0,9,11,10,10
#k    1,6, 0, 0,16,18, 0, 0,29,31
t  nr_tongue
       1,3,6,9,11,9,9,9,9,9
       1,3,3,7,9,10,10,10,10,10
       1,3,6,9,11,10,10,10,10,10
d  nr_discharge
       1,3,6,9,11,9,9,9,9,9
       1,3,6,9,11,10,10,10,10,10
       1,2,2,5,7, 7, 9, 9, 9,17
#d  nr_discharge  ted: plot3d
#      1,3,6,9,11,9,9,9,9,9
#      1,3,6,9,11,10,10,10,10,10
#      1,5,5,10,21,21,24,24,24,27
# cheat in second mapping, replace d(10,3)=17 with a smaller number
# to shorten straight pipe
b  nr_blank
       1,3,6,9,0, 11,9,9,9,9
       1,2,2,2,0, 5,10,10,10,10
       1,2,2,2,0, 7,10,10,10,10
#z  nm_thetz  theta_rv=nang
#      1,1,1,1,12, 10,10,10,10,10,10,10
#      1,9, 0,28,28,28,39,42,45,45,79,83
```

Table A-1 Listing of Sample Problem Coordinate Mapping Input File - volnrn.dat
Continued

```
#      1,2,1,10,11, 10,10,10,10,10,10,10
z nm_thetz  theta_rv=nang   ys 3-23-94
       1,1,1,1,12, 10,10,10,10,10,10,10
       1,6, 0,24,28,28,39,44,54,54,116,122
       1,2,1,10,11, 10,10,10,10,10,10,10
#j recirc      1,17, 0,47,51,51,62,66,74,74,116,122
#j use      1,9, 0,24,28,28,39,44,54,54,116,122
#j      1,6, 0,24,28,28,39,44,54,54,116,122
#z nm_thetz  theta_rv=nang   ys 3-23-94, vol_caf shorten pipe
#      1,1,1,1,12, 10,10,10,10,10,10,10
#      0,1, 0,19,23,23,34,39,49,49,111,117
#      1,2,1,10,11, 10,10,10,10,10,10,10
n
z2  va_yxsu before 4-22-94
       1,9, 0,24,28,28,39,44,54,54,116,122
z nm_thetz  theta_rv=nang
       1,1,1,1,12, 10,10,10,10,10,10,10
       1,9, 0,28,28,28,39,42,54,54,116,122
       1,2,1,10,11, 10,10,10,10,10,10,10


c nm_c around tongue
       1,1,1,1,10, 10,10,10,10,10
       1,15,20,22,25,28,60,60,67,81
       1,1,1,1,10, 10,10,10,10,10
m nm_thetb
       1,5,7,7,13, 9,9,9,9,9
       1,4,4,7,37,43,49,63, 10,10
       1,1,1,1,10, 10,10,10,10,10
n

  cheat
d nr_discharge
       1,3,6,9,11,9,9,9,9,9
       1,3,6,9,11,10,10,10,10,10
       1,2,2,5,7, 7, 9, 9, 9,12

       0,0,1,15,15,15,26,29,32,32,66,70
z nm_thetz
       1,1,1,1,12, 10,10,10,10,10
       1,15,19,19,30,33,35,35,64,68
       1,15,15,15,26,29,31,31,64,68
       1,1,1,1,11, 10,10,10,10,10
```

Table A-1 Listing of Sample Problem Coordinate Mapping Input File - volnrn.dat
Continued

n

m nm_thetb
     1,5,8,8,15, 9,9,9,9,9
     1,4,4,7,37,44,51,65, 10,10
     1,1,1,1,7, 10,10,10,10,10
m nm_thetb
     1,8,11,21,21, 9,9,9,9,9
     1,3,4,7,17,27,37,45, 10,10
     1,1,1,1,10, 10,10,10,10,10
#m nm_theta
1,4,5,5,9, 9,9,9,9,9
1,3,4,7,17,25,27,34, 10,10
1,1,1,1,7, 10,10,10,10,10
1,3,5,7,17,25,27,34, 10,10
c nm_c around tongue
     1,1,5,5,9, 9,9,9,9,9
     1,8,11,12,14,14,25,25,29,36
     1,1,1,1,7, 10,10,10,10,10
n

Table A-2 Listing of Sample Problem Geometry Input File - vol_bud.dat

```
#
#    restart aw0
#   baseline: spiral contour 3 pt arc    NOT 1/8 inlet fillet
#     rfc conv fixed with ishap91
#   csectv(i,1)=hv  use correct wr   replaced .31 w/ .32
#   hv from drawing hv values   wr fillet
#   volute dwg rw=8.62 xv=5.8                    rv(360)=5.79
#   tongue from 3 point arc from drawing
#   straight pipe extension l & m at housing chamber dwg coor, flange exit
#v  R2        B2    R3        WR        R4     DELRNG
#   3.1875  .62   3.3     .784    3.425  0.
#v  R2        B2    R3        WR        R4     IVLINRL RVLINRL
#   3.1875  .62   3.3     .784    3.425   0      .125
v  R1/R2 R2       B2    R3        WR        R4     IVLINRL RVLINRL
   .5 3.1875  .62    3.3       .784    3.425    0       .125
#  spiral cross-section control edges  not use eccentricity yet,
#  use non-zero value, else kdschrg=1 spline t0=0
r
12
 1    7.  1 1 1 1 1  -1 -1 -1 -1 -1  40. 0.328     0.     0.  .0625
 0   40.  0 0 0 0 3   0  0  0 0 91  40. 0.328     0.     0.  .1875
 2   45.  4 0 4 4 0   0 -1 -1 0  0  40. 0.52    .09004  0.  .1875
 0   50.  0 0 0 0 4   0  0  0 0 92  40. 0.52    .09004  0.  .1875
                0 41 0.  0.
 3   90.  7 7 7 7 7   0  3 -1 0 51  40. 0.87    .11114  0.  .1875
-.441070D+00 0.140827D+00 0.000000D+00
 4  135. 10 0 10 10 10  0 -1 -1 0  6  40. 1.18    .12984  0.  .25
                44  1 0 0.  0.   0.
 5  180. 13 13 13 13 13 51  3 -1 0 51  40. 1.44    .14551  0.  .25
-.360073D+00 -.199665D+00 0.000000D+00
 6  225. 16 0 16 16 16  0 -1 -1 0  6  40. 1.69    .16059  0.  .3125
                44  1 0 0.  0.   0.
 7  270. 19 19 19 19 19  0  3 -1 0 51  40. 1.89    .17265  0.  .3125
0.150534D+00 -.293009D+00 0.000000D+00
 8  315. 22 0 22 22 22  0 -1 -1 0  6  40. 2.11    .18592  0.  .375
                44  1 0 0.  0.   0.
 9  360. 25 25 25 25 25  0  3 -1 0 -1  40. 2.49    .20883  0.  .375
0.130232D+00 0.489394D+00 0.000000D+00
10  367. 27 27 27 27 27 51  6  6 1 51  40. 2.5436 .21207  .1  .375
                44  3 4     0.  0.   5.
                22  1 0     0.  0.   0.
#  spiral surface  splines along theta
#    if use control, fix grvc  nrnge(6,ned).le.kl   spline spans entire region
s
```

SECA-FR-95-08

Table A-2 Listing of Sample Problem Geometry Input File - vol_bud.dat
(Continued)

```
       2
    1   9   6   22   104   0   0.
    9  10   6   42   103   4   5.
#  t//c2//c3//c4
#    c2  bc for rv(theta) spline at theta(1)  n=nat bc  s=specify spiral angle
#    c3  tongue center, radius  r=specify radius  c=specify center
#        fit arc between tongue and discharge edges  f=fix radius  e=fix endpt
#    c4  tongue/discharge interface  follow curve until tangent to discharge edge
#        c=follow tongue circle  s=circle and spiral spline    = don't
#  before 3.72  .446  0.                  .12      0.0          .1875
    tsrc  tongue circle center (x,y,z), radius, spiral angle,  rfi_d
       3.7254  .451  0.                  .1246      87.27       .1875
    d1   discharge exit: tongue wall
    e       volute dwg rw=8.62
       1    5       0.244493D+01 0.826600D+01 0.000000D+00
    d2   discharge exit: casing wall
    e       volute dwg rw=8.62
       1    4       0.580000D+01 0.637686D+01 0.000000D+00
    e       housing dwg rw=8.625
       1    5       0.575764D+01 0.860657D+01 0.000000D+00
    f1   flange exit: tongue wall
    e       housing dwg
       1    7       0.177287D+01 0.123214D+02 0.000000D+00
    e  q=22
       1   10       0.911767D+00 0.221638D+02 0.000000D+00
    f2   flange exit: casing wall
    e       housing dwg
       1    7       0.575764D+01 0.126700D+02 0.000000D+00
    e  q=22
       1   10       0.489655D+01 0.225124D+02 0.000000D+00
    n
```

Table A-3 Listing of Sample Problem Grid Stretching Input File - volstr.dat

```
#  volute
#  use '#' for to indicate comments
a  use 'a' to indicate start of node distribution stretching parameters
    1   12   24   0.400000D+01   0.000000D+00
    0    0    0   0.000000D+00   0.000000D+00
    6   24   22   0.000000D+00   0.070000D+00
   24   28   14   0.000000D+00   0.100000D+00
   28   39   24   0.400000D+01   0.000000D+00
   44   54   21   0.300000D+00   0.000000D+00
  116  122   22   0.000000D+00   0.200000D+00
    0    0    0   0.000000D+00   0.000000D+00
    1   11   24   0.400000D+01   0.000000D+00
    0    0    0   0.000000D+00   0.000000D+00
```

Table C-4 Sample Execution of Volute Grid Generation Code

```
av310 [/usr2/ron/grid/opt] gdv
---- new gdv ------
  c:  create mapping
  g:  create grid
  b:  read existing grid data
  n:  execute options selected
  r:  reset program
  q:  quit program
select option c
Select mapping:
  p:  physical--surface coordinate
  c:  cross-section
  a:  Adkins' area integral  defined spiral c-sections
  b:  Adkins' area integral  along spiral region
  d:  discharge area integral
  e:  volute contour edge   iges file
  3:  3 point arc spiral contour
  k:  curvature of spiral c-sections
  i:  second volute mapping  iges surfaces
  t:  psc_surface tongue region
  m:  Adkins' impeller/volute model
  r:  Adkins' model and restart flowfield file
  z:  mapping  c zone: tongue')
p
enter file for nrn data volnrn.dat
enter file for volute geo data vol_bud.dat
enter idim (2-surface  3-volume) 2
enter file for mapping (don't write= ) vcp_bud.gi
select option n
  c:  create mapping
  g:  create grid
  b:  read existing grid data
  n:  execute options selected
  r:  reset program
  q:  quit program
select option c
Select mapping:
  p:  physical--surface coordinate
  c:  cross-section
  a:  Adkins' area integral  defined spiral c-sections
  b:  Adkins' area integral  along spiral region
  d:  discharge area integral
  e:  volute contour edge   iges file
  3:  3 point arc spiral contour
  k:  curvature of spiral c-sections
  i:  second volute mapping  iges surfaces
  t:  psc_surface tongue region
  m:  Adkins' impeller/volute model
  r:  Adkins' model and restart flowfield file
  z:  mapping  c zone: tongue')
z
```

Table C-4 Sample Execution of Volute Grid Generation Code (Continued)

```
enter node stretching file (none= ) volstr.dat
enter idim (2-surface  3-volume) 3
enter file for mapping (don't write= ) vcm_bud.gi
enter edge shape for interface 1-line, 3-arc, 8-log (center at tongue)
   and (2) theta at r2,rv (deg) for interface between tongue and spiral regions
8,360.,360.
add edges to pack grid near tongue
and to smooth re-entrant interface (if not line)
node distribution along spiral on r2
     nr:    44 tongue       54 pack tongue   116 smooth    122 re-entrant
angle:          7.00          52.26          332.85         360.00   uniform dist
enter pack tongue and smooth angles (none=0,0) 30.,340.
add edges along r to adjust non-uniform arclength of spiral surface
in psc_surface interpolation, assume uniform spacing
enter number of edges between thet_a     30.00 and _b    340.00
  >0 will input theta, <0 calculate equidistant   4
enter    4 intermediate (approx) angles (deg)
60,90,180,270
   c:   create mapping
   g:   create grid
   b:   read existing grid data
   n:   execute options selected
   r:   reset program
   q:   quit program
select option q
av310 [/usr2/ron/grid/opt] gdv

---- new gdv -----
   c:   create mapping
   g:   create grid
   b:   read existing grid data
   n:   execute options selected
   r:   reset program
   q:   quit program
select option
select option g
enter mapping file vcp_bud.gi
enter file to store grid data (don't= ) vcp_bud.b
select option n
Store edge coordinates for nreg= 2 ? (def=n) n
Store internal grid for nreg= 2 ? (def=y) n
Store edge coordinates for nreg= 3 ? (def=n) n
Store internal grid for nreg= 3 ? (def=y) n
store (r,theta,z)? (def=n) n
   c:   create mapping
   g:   create grid
   b:   read existing grid data
   n:   execute options selected
   r:   reset program
   q:   quit program
```

Table C-4 Sample Execution of Volute Grid Generation Code (Continued)

```
select option b
enter grid data file vcp_bud.b
select option n
   c:  create mapping
   g:  create grid
   b:  read existing grid data
   n:  execute options selected
   r:  reset program
   q:  quit program
select option g
enter mapping file vcm_bud.gi
select option n
Store edge coordinates for nreg= 4 ? (def=n)
Store internal grid for nreg= 4 ? (def=y)
Store edge coordinates for nreg= 5 ? (def=n)
Store internal grid for nreg= 6 ? (def=y)
store (r,theta,z)? (def=n)
   c:  create mapping
   g:  create grid
   b:  read existing grid data
   n:  execute options selected
   r:  reset program
   q:  quit program
select option q
```